Characterising Mesoscale Fast Flow Channels in the Polar Cap Ionosphere

Katie Herlingshaw

Thesis for the degree of Philosophiae Doctor (PhD)
University of Bergen, Norway
2021

UNIVERSITY OF BERGEN

Characterising Mesoscale Fast Flow Channels in the Polar Cap Ionosphere

Katie Herlingshaw

Thesis for the degree of Philosophiae Doctor (PhD)
at the University of Bergen

Date of defense: 22.01.2021

Year: 2021

Title: Characterising Mesoscale Fast Flow Channels in the Polar Cap Ionosphere

Name: Katie Herlingshaw

Print: Skipnes Kommunikasjon / University of Bergen

Abstract

The large-scale ionospheric convection that circulates in the high-latitude polar caps was initially assumed to be a smooth, laminar flow. However, it has now come to light that this is an oversimplified understanding of what is now known to be a dynamic region, filled with mesoscale velocity features. Ionospheric flow channels, an example of one such feature, have been linked to transient reconnection and a variety of auroral forms. This thesis investigates the statistical distribution and characteristics of these flow channels in the polar cap ionosphere.

To further our understanding of dynamic mesoscale flow channels, a flow channel detection algorithm was developed by using Super Dual Auroral Radar Network (SuperDARN) line-of-sight velocity data. The temporal and two-dimensional spatial evolution of the flow channels can be observed using this method, which was not achievable within previous studies that used satellite data or single SuperDARN radar beams. The detection algorithm was applied in three scientific papers that make up the main body of the thesis. This algorithm identifies fast flow channels (>900 m/s) embedded within a slower moving background flow.

In Paper I, the algorithm was defined and applied to 2017 SuperDARN Longyearbyen radar data. Two events were selected for detailed analysis, one on the edge of a polar cap arc and the other located in the dayside convection throat. These flow channels accounted for large values of the cross polar cap potential (40-60% at the peak).

In Paper II, the flow channel detection algorithm was applied to 2 years of SuperDARN Longyearbyen data. The algorithm detected $\sim$1000 flow channel events, most of which were in the dayside polar cap. The statistical characteristics of the flow channels were determined, including width, velocity, duration, and seasonal occurrence. The zonal motion of the flow channels was investigated and linked to magnetic tension due to a dominant IMF By component.

In Paper III, the flow channel detection algorithm was applied to 10 years (2008-2018) of SuperDARN data of 8 different radars, located across the northern and southern polar cap regions. The statistical distribution of the flow channels was examined and the solar wind driving conditions of the flow channels were investigated.

The main conclusions of the thesis are as follows:

- Fast flow channels in the polar cap are typically 200-300 km in width, travelling at velocities of 1.1-1.3 km/s, and are typically observed for a duration of 2-3 min.

- Fast polar cap flow channels can account for significant fractions of the polar cap potential (40-60%) and are therefore important for the redistribution of flux across the polar cap.

- Fast flow channels in the polar cap are most frequently observed under unstable, By-dominant IMF conditions.
- Fast flow channels were observed at all stages in their evolution over the polar cap. This is the first time that flow channels on old open field lines have been statistically studied, and also the first presentation of statistical occurrence distributions of flow channels at all magnetic local times in both the northern and southern polar caps.

Acknowledgements

These past four years have been phenomenal. There are so many people who have supported/entertained/consoled/put up with me. Thank you to those mentioned here (and all those that I don't have space to thank by name) for being such incredible people!

First and foremost, I would like to thank my main supervisor Dr Lisa Baddeley. I could not have asked for a better guide on the series of winding paths, dead ends, and summit celebrations that is academia. It was a pleasure to to be your PhD student. Thank you for your encouragement and belief in me, for your mentorship, and for your friendship. It is incredible what Boro lasses can achieve together!

I would also like to thank my co-supervisors: Professor Kjellmar Oksavik and Professor Dag Lorentzen. Kjellmar, thanks for all our mini-workshops on your visits to Svalbard. Even if you had a full day of teaching or working at KHO, you would come and find me to help me with my paper/thesis. Thank you for prioritising me and also for teaching me the process of scientific writing (it's all about those bullet points!). Dag, thank you for always having your door open for me, and for your help and patience throughout the PhD. Also thank you for sharing your data analysis skills and methods with me, and always being there to double check whatever scheme Lisa and I had put together. The three of you were a dream team, thanks for all the feedback and for reading all those drafts with lightning speed!

I am grateful to the University Centre in Svalbard (UNIS), the Birkeland Centre for Space Science (BCSS), and the Norwegian Research Council for providing me with the opportunity (and funding!) to achieve my PhD. Thanks to every person who has shared the Geophysics sofa with me over the years. The Arctic Geophysics department has been a wacky, caring, multicultural family that both laughs at and looks out for one another, as families do. A special thanks goes to my work wife Emma. Thank you for sharing both your SuperDARN knowledge and many bottles of Gustav over the years, as well as keeping me well fed during my write-up phase. Thanks to Kjersti, the other half of the Geophysics night crew, for keeping me company at the office at unconventional hours and always being up for second lunch. Thanks to Fasil for years of office banter, morning briefings, and dead office plants.

I have been lucky enough to travel to several meetings, workshops, and courses during my PhD. I would like to thank the SuperDARN community for being such a welcoming gang. Thanks in particular to Angeline Burrell, my good friend and remote Python guru, for teaching me the DaViT-py ropes. Thanks to the Polar Magnetospheric Substorms class of 2017 and to Stein Haaland for organising the course. I learned a lot about space physics, Codenames, and fishing. I would also like to thank the organisers and participants of the CaNoRock STEP PhD School 2019. Our time at Barrier Lake was unforgettable and very productive, and I can now add express paper writing to my

list of skills! Although the paper [*Fæhn Follestad et al.*, 2020] is outside of the scope of this thesis and therefore not included here, the process was still a valuable learning experience for me during my PhD. Thank you to all the co-authors!

The research in this thesis would of course not have been possible without the help of the data providers. I would like to acknowledge the use of SuperDARN data and thank the radar PIs for the radar data in this thesis. Thank you to Dag Lorentzen (University Centre in Svalbard) PI of the LYR radar, Katheryn McWilliams (University of Saskatchewan) PI of the CLY, SAS, and RKN radars, Bill Bristow (University of Alaska Fairbanks) PI of the MCM and SPS radars, Federica Marcucci (Institute for Space Astrophysics and Planetology) PI of the DCE radar, and Hongqiao Hu (Polar Research Institute of China) PI of the ZHO radar. A special thanks also goes to Marina Schmidt and Kevin Krieger for their help accessing the SuperDARN data. I would like to thank Larry Paxton (PI of SSUSI instrument) for the use of DMSP SSUSI data and the Goddard Space Flight Center Space Physics Data Facility for providing IMF and solar wind data. Lastly, thank you to the AMPERE team for providing the Iridium-derived data products and the infamous Steve Milan for providing the R1/R2 boundary circle fits from the AMPERE data.

I would especially like to thank my friends and family for their support and love. I never dreamed that I would be lucky enough to spend my PhD days snowmobiling/hiking/dog sledding/skiing/boating around under northern lights and midnight sun in the High Arctic. Thank you to everyone from the UNIS Spring 2016 semester, I could not leave this town after those months we spent here and now Longyearbyen will always have a special place in my heart. Thanks to Marcos, the nicest guy on the island, for all of the amazing trips and unwavering support. Thank you Joshi, for all the online writing sessions and those precious 5 minute catch up breaks. Thanks to Richard and Kaisa for instructing Lindy Hop with me, who knew Monday could be the best day of the week? Thanks to all the other 'Dog moms': Maya, Alexia, Aga, Marta and Ponti (Bacon's honorary godmother) for all the evenings interrupted by occasional smashing noises. Thank you to my wonderful family for getting me to where I am today, for all the hours of WhatsApp calls, unforgettable visits (Sorry about that ice cave, Julie!), and care/PhD-survival packages. Lastly, I would like to thank my favourite distractions, Bjørn and Bacon, for all of the adventures and just for being your lovable selves.

Without you all, this would not have been possible. Thank you!

Longyearbyen, October 2020

Katie Herlingshaw

Contents

Chapter 1

Introduction

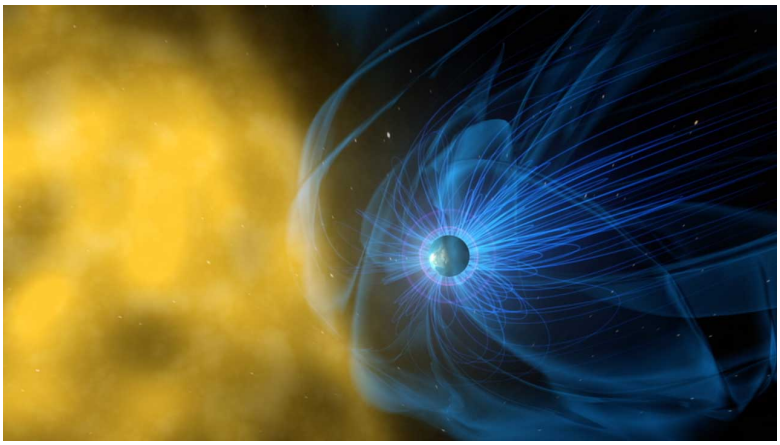

Figure 1.1: Artistic view of the solar wind impacting the Earth's magnetosphere. Courtesy of *NASA* [2020].

The Earth's magnetosphere shields our planet and protects all life and technology within it from the solar wind, a constant stream of high energy particles from the Sun. The response of the magnetosphere to the continuous buffeting by the solar wind strongly depends on the strength and orientation of the interplanetary magnetic field (IMF) embedded within it. The coupling of the IMF and the magnetosphere drives the circulation of the ionosphere, one of the uppermost layers of the Earth's atmosphere. This process is driven by the merging of magnetic fields, called magnetic reconnection. Through reconnection, the IMF can connect to the Earth's magnetic field on the day-side and the Earth's field can connect together deep in the magnetotail on the nightside. Signatures of this cycle are clear in the high-latitude regions of Earth's ionosphere and a convection pattern is formed. Plasma typically drifts antisunwards in the polar cap region, where the Earth's magnetic field lines are connected to the IMF and considered 'open'. After reconnection in the magnetotail, the field lines are considered 'closed' as they loop around from the Earth's Northern Hemisphere to the Southern Hemisphere. These closed magnetic field lines move sunwards at auroral and sub-auroral latitudes. The shape and flows of the convection pattern depend on the orientation of the IMF, which will be discussed in greater detail in Section 2.4.

Ionospheric convection over the polar cap region has often been expected to be a smooth, homogeneous process that is constant over thousands of kilometers with typical speeds of several hundreds of meters per second [*MacDougall and Jayachandran*, 2001]. However, more recent findings suggest that the large scale background convection is punctuated by dynamic mesoscale (100–500 km) high velocity structures. These features are known as ionospheric flow channels, and were first detected during periods of enhanced dayside reconnection [*Pinnock et al.*, 1993; *Provan et al.*, 1998]. These flow channels were detected in the dayside cusp region, which is in the proximity of the first open field line on the dayside, where solar wind particles can directly access the magnetosphere. Since then, flow channels have been detected deep within the polar cap [*Sandholt and Farrugia*, 2009], on the nightside *Zou et al.* [2014], and in the return flow region [*Moen et al.*, 1995]. The research into ionsospheric flow channels has mostly been based on case studies, many of which have been undertaken using satellite crossings. In these cases, only a few minutes of data are available for analysis and only along the satellite trajectory. This provides limited temporal and spatial information about the flow channel and only under specific IMF driving conditions. Although some statistical studies regarding ionospheric flow channels have been carried out, they have been limited to either a single SuperDARN radar beam, or to only a specific range of latitudes and longitudes.

In this thesis, a statistical distribution of ionospheric flow channels in the polar cap will be presented for the first time in both hemispheres. The statistical characteristics of the flow channels will be examined, including width, velocity, duration, and seasonal occurrence. The solar wind conditions that lead to the formation of flow channels will be studied in detail, determining the most important components and the IMF stability conditions that are required to drive the flow channels. Case studies will also be examined, to investigate the relative importance of flow channels in the distribution of magnetic flux across the polar cap. In general, this thesis is concerned with fast flow channels >900 m/s, in cases where there are high velocity gradients with the large-scale background convection on either side of the channel. These fast flow channels are associated with intervals of strong coupling between the solar wind-magnetosphere-ionosphere system.

The findings of the thesis are important because the current statistical models of ionospheric convection only include the large-scale, global responses of Earth's atmosphere to various inputs from the Sun. They do not capture dynamic mesoscale features, which play important roles in flux transferal across the polar cap. Density features associated with ionospheric flow channels have also been observed to lead to severe phase and amplitude scintillation in trans-ionopsheric radio signals, such as those used in global navigation systems [*Oksavik et al.*, 2015; *Spicher et al.*, 2020]. This can affect both navigation and communication systems, which can have adverse implications, especially for aircraft in the polar regions. A comprehensive understanding of flow channels and their driving conditions will allow improvements to forecasts that predict such disturbances. In addition, research into flow channels will enhance our understanding of solar wind-magnetosphere-ionosphere coupling. This will lead to superior space weather forecasts, which are becoming increasingly vital with expansions in space-based infrastructure and increased activity on manned space missions.

Thesis Objective

The overall objective of this thesis is to investigate the role of fast ionospheric flow channels (>900 m/s) within the polar cap. Both case studies and statistics are used to investigate the following knowledge gaps:

1. What are the typical characteristics of fast flow channels?
2. What is the spatial distribution of fast flow channels?
3. How important are fast flow channels in the transport of magnetic flux across the polar cap?
4. What interplanetary magnetic field conditions drive fast flow channels?

Approach

These questions are addressed through work presented in three scientific papers:

- **Paper I**: A Study of Automatically Detected Flow Channels in the Polar Cap Ionosphere (Published Article)
- **Paper II**: A Statistical Study of Polar Cap Flow Channels and their IMF By dependence (Accepted Article)
- **Paper III**: A Statistical Study of Polar Cap Flow Channels observed in Both Hemispheres using SuperDARN Radars (Submitted Article)

In Paper I, an algorithm is developed to detect fast flow channels within SuperDARN Longyearbyen radar data. Case studies are examined where flow channels occur on the side of a polar cap arc and within the convection throat. In Paper II, the algorithm is applied to 2 years worth of SuperDARN Longyearbyen radar data to study the statistical characteristics of zonal flow channels. Particular attention is paid to the relationship of IMF By to the flow channels, as the SuperDARN Longyearbyen radar is optimally aligned to study flow channels under the magnetic tension force applied by IMF By. In Paper III the detection algorithm was applied to 8 SuperDARN radars, 4 in each of the polar hemispheres. A 10 year statistical study was undertaken to investigate the solar wind driving conditions of the flow channels.

Thesis Organisation

The relevant background theory for the thesis is presented in Chapter 2, followed by a description of the instrumentation and data used in Chapter 3. The results are summarised in Chapter 4 and discussed in Chapter 5. Conclusions and future work are presented in Chapter 6, and the Papers are available in the Appendix.

Chapter 2

Theoretical Background

2.1 The Solar Wind and Interplanetary Magnetic Field

A constant stream of charged particles is emitted from the Sun's corona, propagating radially outwards and populating the solar system with plasma. These particles are known as the solar wind, a highly conductive medium consisting primarily of ions and electrons (mainly fully ionized hydrogen and helium atoms) due to the high temperatures of 10^6K in the solar corona. In a highly conducting medium, magnetic field lines are frozen into the plasma [*Alfvén*, 1942]. The Sun's magnetic field is therefore carried with the solar wind and permeates the solar system. This is known as the interplanetary magnetic field (IMF), which was first measured and mapped by the Pioneer V probe in 1960 [*Coleman Jr et al.*, 1960].

Although the Sun's magnetic field is carried radially outwards with the solar wind, the foot of the magnetic field line remains fixed to the Sun. The rotation of the Sun therefore has a twisting effect on the configuration of the IMF and it ultimately forms a spiral shape [*Parker*, 1963], as illustrated in Fig.2.1. The direction of the magnetic field in the Northern Hemisphere is opposite that of the field in the Southern Hemisphere and a thin current sheet separates the two [*Smith*, 2001]. This current sheet does not lie in the equatorial plane, as the dipole axis and rotation axis of the Sun are offset. This leads to a distortion of the current sheet, which is usually described as the 'ballerina skirt' configuration. The relative location of the Earth to the current sheet determines which sense of the IMF is measured at Earth, with the IMF varying between sectors of magnetic field directed towards and away from the Sun [*Hoeksema*, 1995].

There are now near continuous measurements of the solar wind and IMF recorded from in-situ spacecraft, dating back to 1996 and the advent of the WIND and ACE spacecraft [*Ogilvie and Desch*, 1997; *Papitashvili and Rich*, 2002; *Smith et al.*, 1998]. At the Earth, a distance of 1 AU from the Sun, the IMF typically has a speed of 450 km/s, an electron density and temperature of 5 cm^{-3} and 10^5 K, and a magnetic field strength of 5 nT [*Baumjohann and Treumann*, 1997]. The IMF and solar wind display both long term predictable variability and short term, stochastic variations. The Sun goes through an 11-year activity cycle. This is characterised by the rise and fall of the number of visible sunspots, which are cooler regions of the Sun's photosphere from which the Sun's magnetic field protrudes almost vertically upwards [*Beckers and Schröter*, 1968]. At solar minimum, there are very few sunspots and the Sun's magnetic field is approximately dipolar. At solar maximum, there is a higher number of

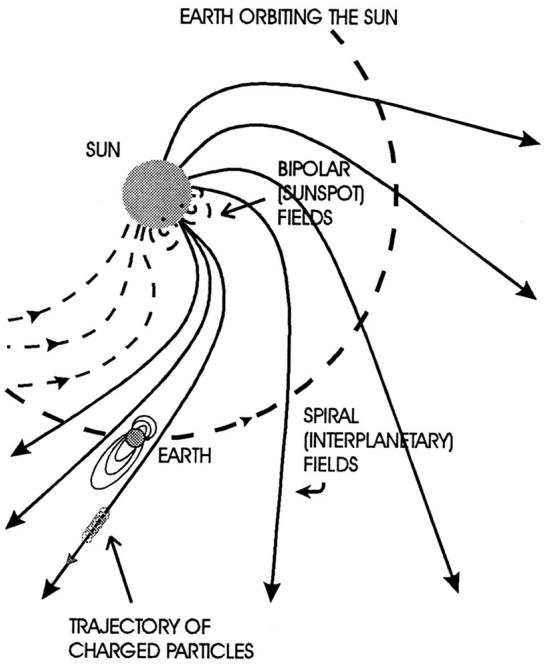

Figure 2.1: Schematic showing the Sun and the interplanetary magnetic field, which twists into a Parker spiral configuration due to the Sun's rotation [*Nishida et al.*, 2009].

sunspots and the Sun's magnetic field is highly disordered [*Babcock*, 1959]. Over the next 11 years, the sunspot number drops, the polarity of the field reverses and the cycle begins again. On shorter time scales, phenomena such as coronal mass ejections and co-rotating interaction regions produce IMF conditions which can strongly couple to and drive the Earth's magnetosphere and ionosphere [*Lindsay et al.*, 1995].

2.2 The Ionosphere

The ionosphere is a part of the terrestrial atmosphere that contains weakly ionized plasma, spanning from 50–1000 km in altitude. This region includes the thermosphere and parts of the mesosphere and exosphere (Fig.2.2a). There are two sources of ionisation in the ionosphere: photoionisation by solar Extreme UltraViolet (EUV) and X-ray radiation, and impact ionisation from energetic particle precipitation.

The ionosphere is divided into layers, based on peaks in the ionospheric electron density profile, as shown in Fig.2.2b. There are 3 principle layers: the D region (below 90 km), E-region (90–130 km), and F-region (above 130 km). The F-region can also be further divided into the F1- and F2-layers due to the smaller peak sometimes present in the density profile below the main F2 peak, during daytime (EUV illuminated) hours.

Production due to solar EUV and particle precipitation and loss due to radiative and dissociative recombination occur at varying rates [*Biondi*, 1969]. This results in a dynamic ionosphere, with the ionospheric layers often changing in shape and altitude.

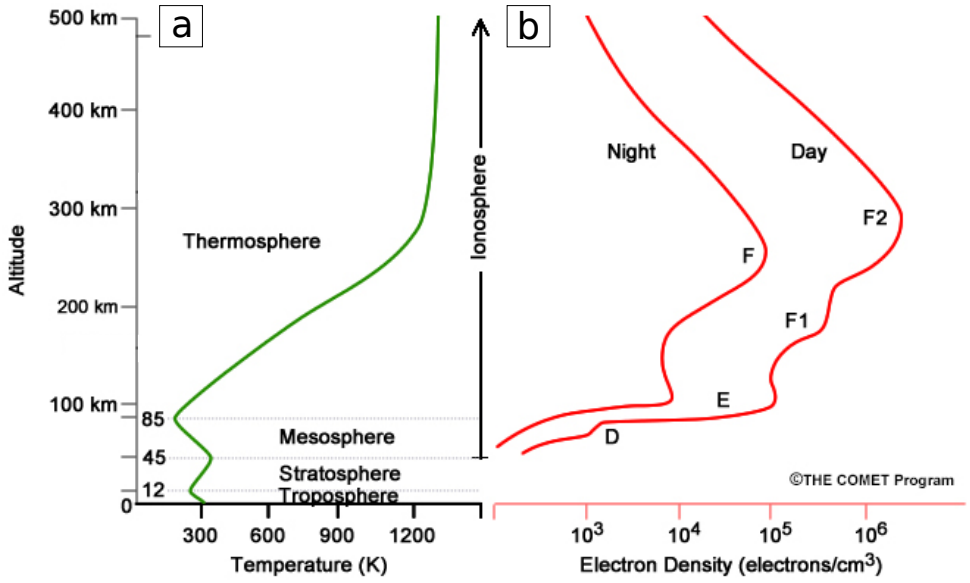

Figure 2.2: Graphs showing a) the atmospheric temperature profile and associated regions and b) the ionospheric electron density profile with the associated regions for both day and night. Image courtesy of *The Comet Program*® [2018].

There are some predictable variations, such as the changes in the layers from day to night, as shown in Fig.2.2b. The removal of the photoionisation source at night results in a significant reduction in the D- and E-layers. The F-region persists throughout the night due to its lower ion-neutral collision frequency and therefore slower recombination rate. The ionosphere also shows predictable seasonal and solar cycle variations [*Richards*, 2001].

2.3 Coordinate Systems

The geocentric solar magnetospheric (GSM) coordinate system (e.g. *Laundal and Richmond* [2017]) is considered to be the most appropriate system to use when studying the effects of the IMF components on the Earth's magnetospheric and ionospheric phenomena. This is because the direction of the geomagnetic field near the nose of the magnetosphere is well ordered by this system. The orientation of the x-, y-, and z-axes are shown in Fig.2.3a. The x-axis points along the line from the center of the Earth (the origin) towards the center of the Sun. The y-axis is perpendicular to both the magnetic dipole axis and the Earth-Sun line, and is positive towards dusk. The z-axis completes the right hand set and is in the plane containing both the Earth-Sun line and the dipole axis, positive towards the northern magnetic pole. References to northward and southward IMF indicate a +Bz and -Bz component, respectively.

When studying features in the polar regions of Earth that are ordered by Earth's magnetic field, it is conventional to take a top-down view of the Earth and plot in geomagnetic coordinates. Geomagnetic latitude is measure with respect to the geomagnetic

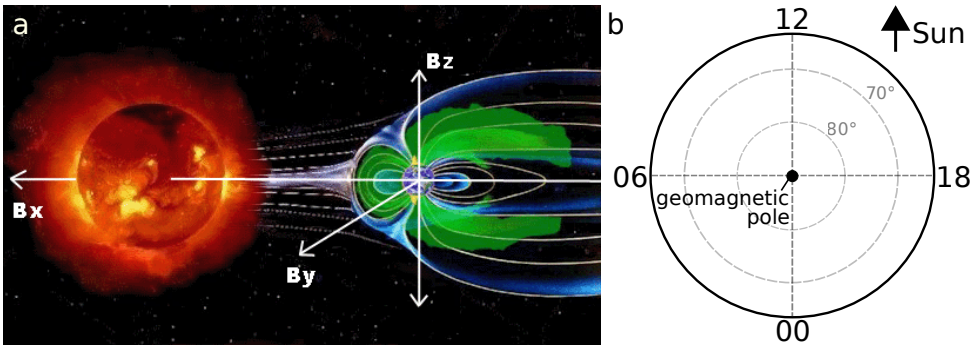

Figure 2.3: Schematic showing a) the orientation of the geocentric solar magnetospheric coordinate system (image courtesy of *SpaceWeatherLive* [2020]) and b) a plot of the northern polar region in the magnetic local time/magnetic latitude (MLT/MLAT) coordinate system.

pole and geomagnetic longitude is fixed to the surface of the Earth, so it rotates with the planet. A convenient way to visualize processes in the polar regions of Earth that are driven by the interaction with the Sun is to introduce magnetic local time (MLT), and use this instead of magnetic longitude. MLT allows us to organise data with respect to the position of the Sun, and is defined by *Baker and Wing* [1989] as

$$MLT = UT + (\phi + \phi_N)/15, \tag{2.1}$$

where UT is universal time, ϕ is the magnetic longitude, and ϕ_N is the geographic longitude of the North centered dipole pole. Fig.2.3b shows an example plot of the polar region MLT/magnetic latitude(MLAT) coordinates. The MLT hours of 12, 06, 00, and 18 are often referred to as noon, dawn, midnight and dusk. An observer at a given MLAT will rotate though all hours of MLT over the course of a day, will see the Sun rise at dawn and set at dusk, and be directed towards the Sun and magnetotail at noon and midnight.

2.4 The Dungey Cycle

Similar to the solar wind and the IMF, the Earth's magnetospheric plasma and geomagnetic field are also frozen together (to a first approximation) due to Alfvén's theorem. The Earth's magnetic field acts an an obstacle to the solar wind plasma flow. The two fields cannot mix, and a current sheet is formed at the boundary between them, which is called the magnetopause [*Russell and Elphic*, 1978]. The solar wind is deflected around the magnetosphere, compressing the dayside magnetosphere and extending the nightside out into a long magnetotail. The solar wind speed is slowed from supersonic to subsonic speeds when it encounters the Earth's magnetosphere, and a shock boundary called the bow shock is formed upstream [*Farris and Russell*, 1994; *Formisano*, 1979]. The solar wind is slowed, compressed, and heated across the bow shock, which creates a turbulent region between the bow shock and the Earth's magnetosphere known as the magnetosheath. These regions are illustrated in Fig.2.4.

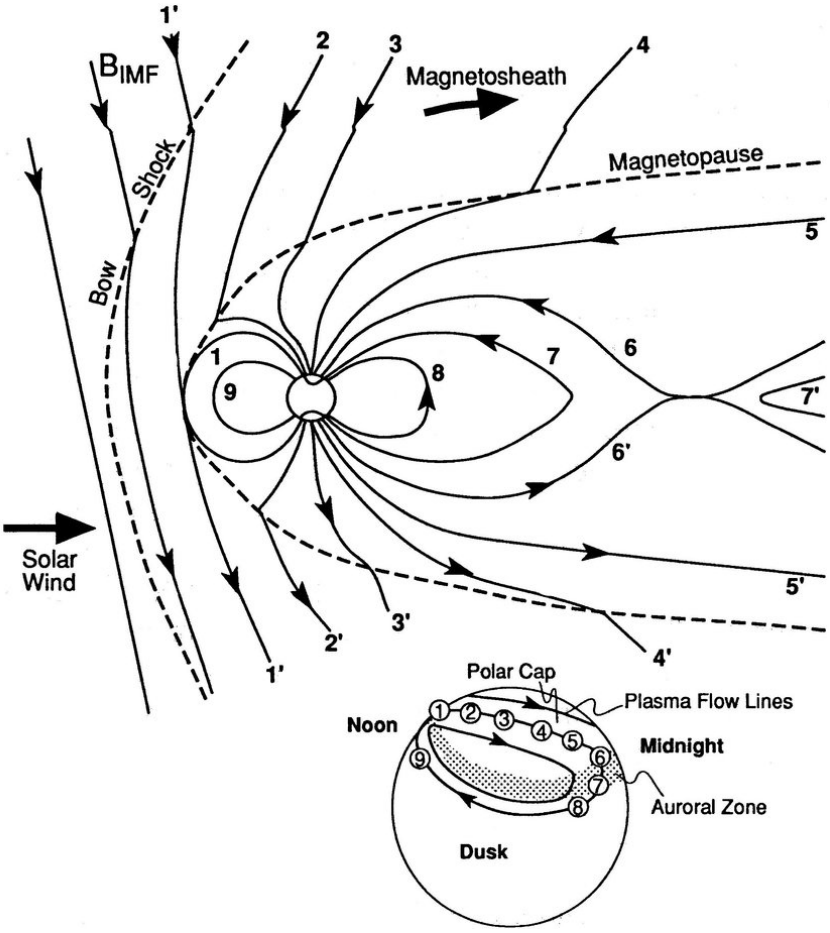

Figure 2.4: The Dungey cycle of the Earth's open magnetosphere under southwards IMF. On the top, there is a magnetospheric view of a southward IMF line as it reconnects with the northward directed field at Earth's magnetopause. Boundaries are labelled and field lines are numbered at different stages in the Dungey cycle to help facilitate discussion. On the bottom, there is an ionospheric projection of the cycle and the resulting convection, with the numbers corresponding to the same stages as in the magnetospheric view [*Kivelson et al.*, 1995].

If Alfvén's theorem was always valid, the magnetic fields and plasma of the Earth and the Sun would remain separated by the magnetopause and the Earth's magnetosphere would form a closed cavity [*Chapman and Ferraro*, 1930]. There would be no transfer of plasma, mass or momentum across this boundary. However, the approximation only holds when the spatial scales under consideration are large compared with the electron and ion gyroradii. The magnetopause is a thin current sheet, so the approximation can break down. This break down is referred to as magnetic reconnection (e.g. *Biskamp* [1996]), which allows IMF field lines to diffuse through the magnetopause and connect with the terrestrial field lines, allowing the separate fields to merge and the plasmas to mix. Magnetic reconnection is most effective when the magnetic shear angle is large between the two regimes, maximising when the two fields are anti-parallel [*Dungey*, 1961].

In 1961, Jim Dungey first realised the far reaching implications of magnetic reconnection on the Sun-Earth interaction and the consequent circulation of the Earth's magnetic field and plasma. He proposed an open magnetospheric model, which is now known as the Dungey cycle [*Dungey*, 1961]. Fig.2.4 shows a sequence of field lines from 1–9, which occur under the specific case of a southwards IMF. Closed field lines map to lower latitudes and are defined as field lines with both of their footpoints connecting to the Earth, one in each of the Northern and Southern Hemispheres. Open field lines map to high-latitudes and have one footpoint on Earth and the other connecting out into the IMF. The region of open field lines emerging from the north and south poles are known as the polar cap regions. The boundary between these two types of field lines in the Earth's magnetosphere is known as the open-closed field line boundary (OCB). *Dungey* [1961] suggested that at the nose of the magnetopause, magnetic reconnection could occur between the oppositely directed northward terrestrial field and the southward IMF (point 1 in Fig.2.4). This creates an open field line from a previously closed field line and allows mass, momentum and energy transfer from the solar wind to the Earth's magnetosphere. The newly-opened field lines convect anti-sunwards across the polar cap and gather in the magnetotail (points 2–5 in Fig.2.4). The additional field lines exert pressure on the magnetotail, forcing the oppositely directed magnetotail lobes together. This initiates further reconnection within the magnetotail (point 6 in Fig.2.4) and ejects a plasmoid away from Earth (point 7 in Fig.2.4). The field lines are then closed and flow back towards Earth and the dayside magnetopause (points 8–9 in Fig.2.4) and the cycle begins again.

The field lines undergoing the Dungey cycle are frozen into the ionized plasma in the high-latitude ionosphere. The motion of the field lines therefore cause the ionosphere to flow. Fig.2.4 also shows the resultant horizontal motion of the ionosphere, where the numbers refer to the stages of the field lines indicated in the magnetospheric section of the diagram. The circulation takes a twin-cell convection pattern [*Heelis*, 1984; *Heppner and Maynard*, 1987], convecting anti-sunwards over the polar cap at high-latitudes on open field lines. At lower latitudes, the flow is in the sunwards direction on closed field lines and is often called return flow.

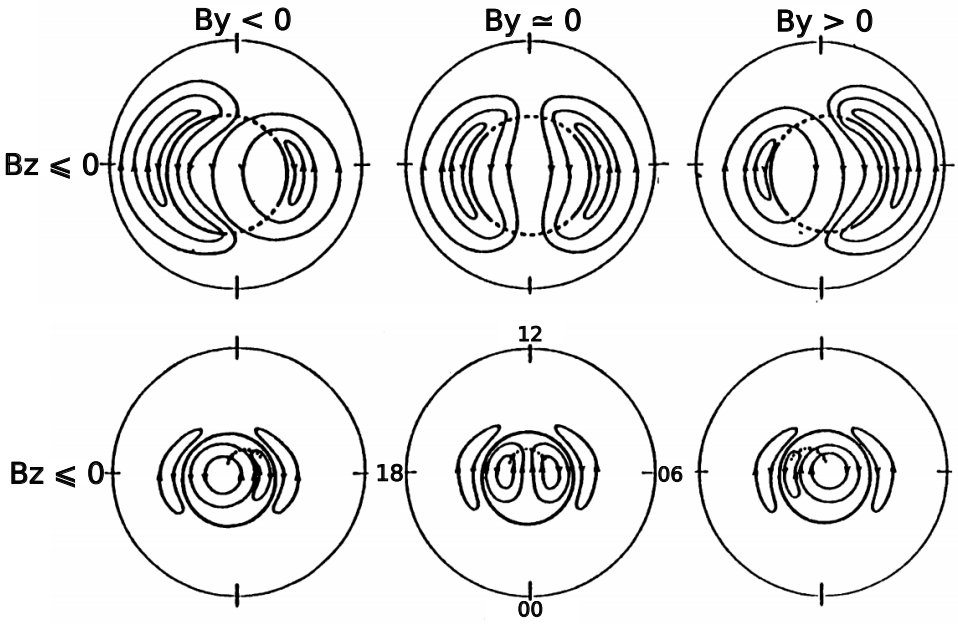

Figure 2.5: Sketch showing the form of the high-latitude convection in the Northern Hemisphere for different orientations of the interplanetary magnetic field (Adapted from *Cowley and Lockwood* [1992]).

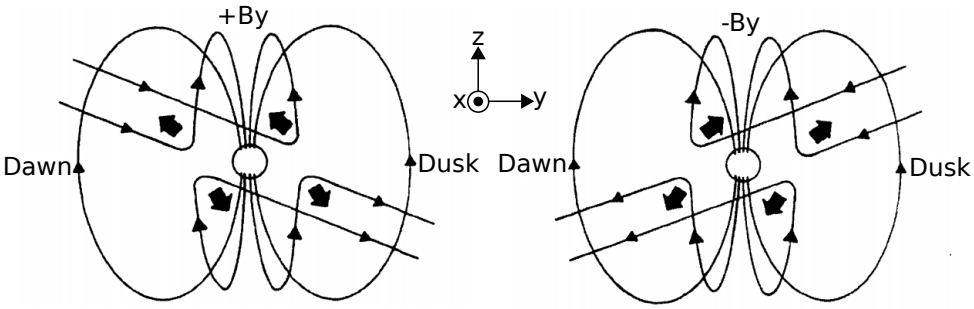

Figure 2.6: Schematic of the dayside magnetosphere as viewed from the Sun, showing different magnetic field configurations after reconnection under +IMF By (left) and -IMF By (right). The thick black arrows indicate the direction of the magnetic tension force on the newly opened field lines. The GSM coordinate system is indicated by the x, y, and z arrows. Figure adapted from *Gosling et al.* [1990].

2.5 Different Reconnection Geometries

The size, shape and location of the ionospheric convection cells are affected by the strength and orientation of the IMF. The orientation of the IMF is often referred to in terms of IMF clock angle, the angle of the IMF relative to north in the Y-Z plane, which is defined as:

$$\theta = \tan^{-1}\left(\frac{B_y}{B_z}\right), \tag{2.2}$$

where θ ranges from 0 - 360°. When θ is 0° and 180°, the IMF is directed purely northwards and southwards respectively, without an IMF By component. At angles of of 90° and 180°, the IMF has no Bz component and is directed towards +By and -By respectively. Although reconnection is most effective at the dayside magnetopause for anti-parallel fields ($\theta = 180°$), it can occur for a wide range of clock angles (30° to 330°) [*Neudegg et al.*, 2000]. For strongly northward IMF ($45° < \theta$ and $\theta > 315°$), the location of the reconnection shifts to high-latitudes in the region of the magnetospheric lobes [*Cowley and Lockwood*, 1992]. Statistically, a four-cell convection pattern exists during this IMF orientation, with two 'reverse cells' at higher latitude (poleward of 80°) that are driven by lobe reconnection, and an additional two cells at lower latitudes driven by viscous processes at the magnetopause [*Ruohoniemi and Greenwald*, 1996]. As By becomes more dominant, the location of the reverse cells changes and one of the cells diminishes in size, until a three-cell convection pattern is observed (Fig.2.5, bottom row) [*Huang et al.*, 2001].

For purely southwards IMF ($\theta = 180°$), the convection cells are symmetrical and expanded due to ongoing dayside reconnection at the subsolar magnetopause. The addition of a By component in this case causes open flux tubes to be added asymmetrically into the magnetotail lobes [*Jørgensen et al.*, 1972]. Evidence to support the IMF By effect on the convection cells was first reported by *Svalgaard* [1969] and *Mansurov* [1969] and the phenomenon was later named the Svalgaard-Mansurov effect. They observed that in the dayside cusp region, deflections in ground based magnetometer data

were dependent on IMF By. These signatures were interpreted as the magnetic signature of an azimuthal flow driving a Hall current along the poleward edge of the OCB, which ultimately causes the asymmetrical loading of the magnetotail. Fig.2.6 shows the magnetospheric configuration for reconnection with a positive By component and a negative By component. An +IMF By component causes the addition of flux tubes to the dawn side of the northern tail lobe and the dusk side of the southern tail lobe. The opposite case is true for -IMF By. The resultant ionospheric convection patterns are shown in Fig.2.5. In the Northern Hemisphere under +IMF By, the round dusk cell dominates over the crescent shaped dawn cell, and westward flows are initiated immediately poleward of the OCB. For -IMF By in the Northern Hemisphere, the cells show the opposite configuration and eastward flows are initiated immediately poleward of the OCB. The opposite cases are true in the Southern Hemisphere. The flows excited by the azimuthal component of the IMF agree with the magnetic signatures observed by *Svalgaard* [1969] and *Mansurov* [1969].

2.6 The Magnetospheric Current System

In the early twentieth century, Kristian Birkeland proposed the existence of large scale currents that flow along Earth's magnetic field lines, connecting the magnetosphere to the high-latitude ionosphere [*Birkeland*, 1908]. This theory sparked fierce debate within the scientific community until the space age, where in-situ measurements of the Earth's magnetic field at high altitudes could be made by satellites. Early satellites detected magnetic perturbations associated with the large scale field aligned currents [*Zmuda et al.*, 1966], and the morphology of the currents, now named Birkeland Currents, was first deduced using Triad satellite observations [*Iijima and Potemra*, 1978].

The Birkeland currents are generally split into two regions: Region 1 (R1), which flows into the ionosphere on the dawn side and out of the ionosphere on the dusk side, and Region 2 (R2), which has the opposite polarity. These current systems form two concentric rings, where R1 lies polewards of R2. R1 is co-located with the flow shear between sunward and antisunward plasma flow within the two-cell convection pattern, which is in the general region of the boundary between open and closed field lines. The currents serve as a component in a giant magnetospheric circuit, schematically shown in Fig.2.7. Other large scale currents flow in the magnetosphere, directed dawn-to-dusk at the magnetopause [*Chapman and Ferraro*, 1930], dawn-to-dusk within the magnetotail at the boundary between the Northern and Southern tail lobes, and westwards due to the ring current within the inner magnetosphere [*Milan et al.*, 2017]. The magnetopause currents can close either through the magnetotail in large current loops, or also through the R1 Birkeland current, linking the magnetosphere to the ionosphere. In the second case, Pedersen currents then flow in the ionosphere, linking the R1 and R2 current systems on the dawn side. The R2 currents connect to the partial ring current, which then flows towards the dusk region 2 current. The Pedersen current once again connects the dusk side R2 to the R1 current, which then flows back up to the magnetopause, completing the circuit [*Cowley*, 2000]. Pedersen currents can also link the R1 current systems on the dawn and the dusk side, but generally these currents are weaker than in the auroral zones due to a lower conductance within the polar cap [*Coxon et al.*, 2014]. The Birkeland currents are a fundamental link in magnetosphere-ionosphere

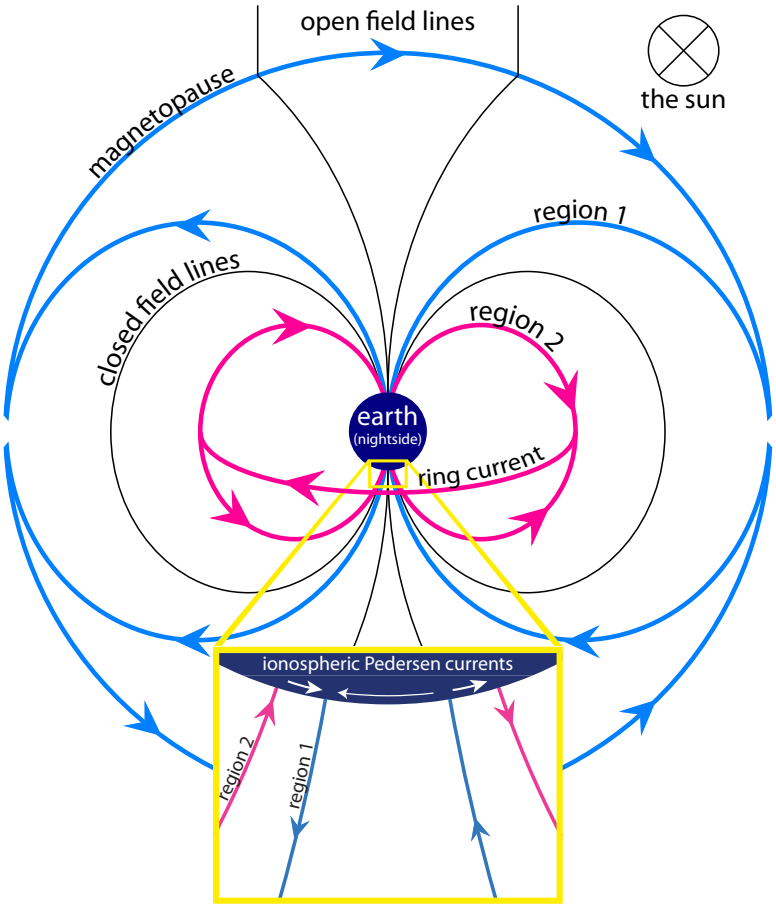

Figure 2.7: Diagram viewed from the nightside of Earth, showing the Birkeland currents (Region 1 and Region 2), Pedersen currents in the ionosphere, and the magnetopause and ring currents. The regions of open and closed field lines are indicated on the figure, as well as a zoomed in view of the Birkeland currents connecting with the Pedersen currents in the Southern Hemisphere [*Coxon et al.*, 2014].

coupling. Plasma can be set into motion in the ionosphere because stresses are transferred through the current systems from the magnetosphere to the ionosphere when reconnection occurs.

2.7 Statistical Models of the Large-Scale Ionospheric Convection

Statistical ionospheric convection patterns are crucial for understanding the overall motion of plasma over the polar cap. There have been numerous attempts to describe the convection pattern by using a variety of observations and techniques. These include: satellite measurements from low-altitude spacecraft (e.g. DMSP) [*Hairston and Heelis*, 1990; *Heppner and Maynard*, 1987; *Heppner*, 1977; *Papitashvili et al.*, 1999; *Papitashvili and Rich*, 2002; *Rich and Hairston*, 1994; *Weimer*, 1995, 1996, 2005], high altitude spacecraft (e.g. Cluster) [*Föerster et al.*, 2007; *Förster and Haaland*, 2015; *Förster et al.*, 2009; *Haaland et al.*, 2007], incoherent scatter radars (e.g. Millstone Hill) [*Foster et al.*, 1986; *Foster*, 1983; *Holt et al.*, 1987; *Oliver et al.*, 1983; *Peymirat and Fontaine*, 1997; *Senior et al.*, 1990; *Zhang et al.*, 2007], ground-based magnetometer arrays [*Friis-Christensen et al.*, 1985; *Papitashvili et al.*, 1994; *Ridley et al.*, 2000], and coherent scatter radars (e.g. SuperDARN) [*Cousins and Shepherd*, 2010; *Pettigrew et al.*, 2010; *Ruohoniemi and Greenwald*, 1996, 2005; *Thomas and Shepherd*, 2018].

The most widely used statistical convection maps are derived by combining many years of velocity measurements from radars within the SuperDARN network to produce global maps of electrostatic potential, expressed as series expansions in spherical harmonics [*Ruohoniemi and Greenwald*, 1996]. The method behind the convection map is shown in Section 3.1.3, along with an example plot. These models allow a prediction of the overall plasma motion in the ionosphere with respect to IMF orientation and dipole tilt angle conditions. They are well constrained in areas of good data coverage, but are entirely model dependent in areas without data. The model used to produce the convection map has evolved over the years, as more radars were built to increase coverage, longer time series became available, and software improvements allow a higher quality of data for input. Currently, the TS18 model [*Thomas and Shepherd*, 2018] is used as the default model in convection map generation, which was derived using measurements for mid, high, and polar latitude radars from the years 2010-2016.

However, each cell in a global convection map is a 111 km x 111 km square, and small scale velocity structures will not reproduce as well as large-scale features in convection map contours. *Bristow et al.* [2016] has addressed this issue by implementing a new technique termed Local Divergence-Free Fitting (LDFF). This technique assumes the velocity field to be divergence free to produce high resolution local convection maps. This work will allow for smaller scale velocity features to be examined in unprecedented detail. However, the uncertainty in the location of the observations due to high frequency (HF) signal propagation becomes more critical at higher resolution and can be larger than the specified grid resolution. This uncertainty should be minimised to allow the technique to give the most realistic results at high resolutions, and show accurate spatial relations between features in other data, such as optical auroral arcs.

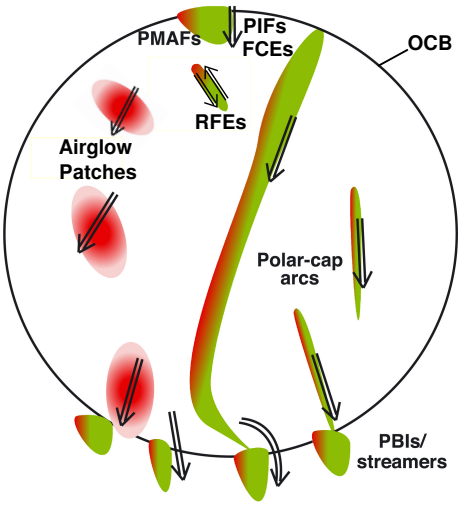

Figure 2.8: Schematic showing the approximate location of flow channels in the polar cap region. The OCB is indicated as the black encompassing circle. The view of the polar cap is that of an MLAT/MLT diagram, with noon at the top and dusk to the left. Various types of flow channels and optical features are indicated in the diagram and discussed further in the text. Figure adapted from *Lyons et al.* [2016].

2.8 Distribution of Flow Channels in the Polar Ionosphere

The large-scale convection is frequently punctuated by mesoscale (100-500 km) features, that flow in the same direction as the background convection, but at an enhanced velocity. These structures are called ionospheric flow channels and are the main topic of this thesis. The following sections will summarise the research on flow channels in different regions of the ionosphere, including their signatures in different types of data, the configuration of the magnetic field lines they occur on, their characteristic length and duration, and the driving mechanisms behind their excitation.

Fig.2.8 shows a schematic of flow channels detected within different regions of the polar cap and their associated auroral forms. On the dayside, close to the cusp region there are observations of Flow Channel Events (FCEs; Section 2.9.1), Pulsed Ionospheric Flows (PIFs; Section 2.9.2), and Reversed Flow Events (RFEs; Section 2.9.3), which have been linked with an optical signature known as a Poleward Moving Auroral Form (PMAF; Section 2.13). Deeper into the polar cap, flow channels are associated with airglow patches (Section 2.13), which drift from the dayside to the nightside, embedded within the background convection flow. Flow channels have also been associated with polar cap arcs (Section 2.12). On the nightside, flow channels have been observed in associated with Poleward Boundary Intensifications (PBIs) and auroral streamers (Section 2.10.1). All of the aforementioned flow channels except the auroral streamers occur on open field lines in the polar cap and are the most relevant flow channels to this thesis. However, there have also been cases of flow channels on closed field lines, in the sub-auroral return flow regions, which are also presented for completeness (Section 2.11).

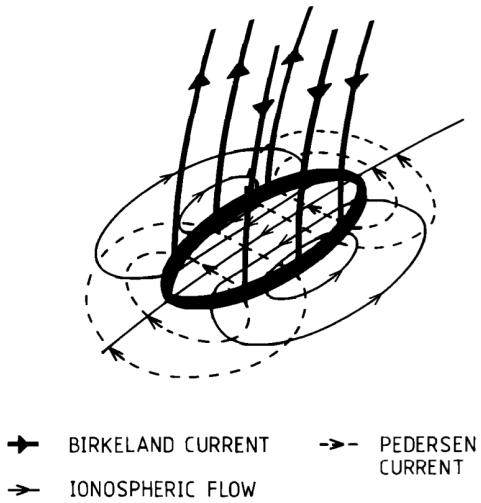

Figure 2.9: The current, ionospheric flow and magnetic field orientation surrounding a flux transfer event [*Southwood*, 1987]. The directions are appropriate for a location in the high-latitude Northern Hemisphere, where the Earth's magnetic field is orientated vertically downward.

There is a large body of literature on certain types of flow channels with locations that are constrained in MLT/MLAT. The links, if there are any, between the different types of flow channels is an open question in the field. The following sections will give a detailed insight into ionospheric flow channels and their optical counterparts.

2.9 Dayside Transients

Transient recconnection at the dayside magnetopause occurs in bursts known as Flux Transfer Events (FTEs), characterised by a bi-polar variation in the boundary-normal component of the magnetic field within spacecraft data [*Haerendel et al.*, 1978; *Russell and Elphic*, 1978, 1979]. *Southwood* [1987] predicted that as a flux tube accelerates away from the reconnection site, the information is communicated from the magnetosphere to the ionosphere via Alfvén waves (1–2 mins), and the foot of the flux tube begins to move through the ionosphere. To overcome the drag caused by ion-neutral collisions and continue its motion in the ionosphere, the solar wind transfers momentum via field aligned currents (Birkeland currents) on the flanks of the flux tube [*Glassmeier and Stellmacher*, 1996; *Southwood*, 1985, 1987; *Southwood and Hughes*, 1983]. These field aligned currents are closed in the ionosphere via Pedersen currents. The **j** x **B** force associated with the Pedersen currents points in the direction of motion of the flux tube, providing the momentum to counter the drag from the ion-neutral collisions, driving a vortex-like flow in the ionosphere. The orientation of the currents and flows discussed are shown in Fig. 2.9, where the FTE moves to the left in this case. *Southwood* [1987] suggested that these ionospheric FTE signatures should be detectable as anti-sunward jets of high speed plasma flow in the vicinity of the dayside polar cap

boundary.

2.9.1 Flow Channel Events (FCEs)

Many years after FTEs were identified in satellite data, the first observations of ground-based FTE signatures were reported [*Goertz et al.*, 1985; *Van Eyken et al.*, 1984]. Since then, the ground-based signatures of FTEs have been observed multiple times, including many observations by the HF SuperDARN radars. *Pinnock et al.* [1993] measured the ionospheric response to FTEs in SuperDARN radar data as a high velocity flow channel in the F-region ionosphere. The structure, which they named a Flow Channel Event (FCE), was detected with the Halley radar (Antarctica), one of the two radars in the Polar Anglo-American Conjugate Experiment (PACE), which later became part of the SuperDARN network [see Section 3.1]. *Pinnock et al.* [1993] described the flow channel as a longitudinally elongated (> 900 km), latitundinally narrow (100 km) channel of enhanced convection at high negative velocities (< -2-3 km/s). The flow channel is shown in Fig.2.10a as a velocity enhancement away from the radar, contained within the black oval. The flow channel occurred under -IMF Bz (-12 nT), -IMF By (-3nT) conditions, and moved in a westward, anti-sunward direction, which is consistent with the magnetic tension forces exerted on the newly opened field lines in the Southern Hemisphere.

Marchaudon et al. [2004] detected signatures associated with an FTE within Northern Hemisphere SuperDARN data and coincident data from the Ørsted satellite. This satellite data was the first in-situ measurement of the FAC system surrounding a flow channel. Fig. 2.10b shows the direction of the FACs surrounding the flow channel along the satellites orbit. The flow channel is associated with the high-latitude pair of FACs (3 & 4), where (3) is pointing downward on the equatorward flank of the flow channel and (4) is pointing upwards on the poleward flank of the flow channel. This orientation of currents confirmed the *Southwood* [1987] model and the same configuration of currents can be seen in the schematic in Fig.2.9.

2.9.2 Pulsed Ionospheric Flows (PIFs)

The FTE category of flow channel was further researched by *Provan et al.* [1998]. They employed a special two-beam, high temporal resolution scanning mode on the Hanksalmi SuperDARN radar and observed a series of FCE signatures poleward of the dayside convection reversal boundary. They noted that the signatures occurred periodically with a recurrence rate of between 7 to 8 minutes, similar to the mean recurrence rate of FTEs (8 minutes) [*Lockwood and Wild*, 1993; *Rijnbeek et al.*, 1984]. *Neudegg et al.* [2000] conducted a survey of FTEs and flow bursts in the polar ionosphere using data from the Equator-S spacecraft and SuperDARN HF radars. They found the two features to be statistically associated with greater than 99% confidence.

In a two-year statistical study of PIFs between March 1995 - February 1997 using the same high resolution radar mode as in the previously mentioned study, *Provan et al.* [1999] researched the influence of the IMF By component on the magnetic local time location of PIFs. They observed that in the Northern Hemisphere, the PIF location shifted towards the post-noon for a +IMF By and the pre-noon for -IMF By. The flow direction of the PIFs is then west (east) for positive (negative) IMF By. This

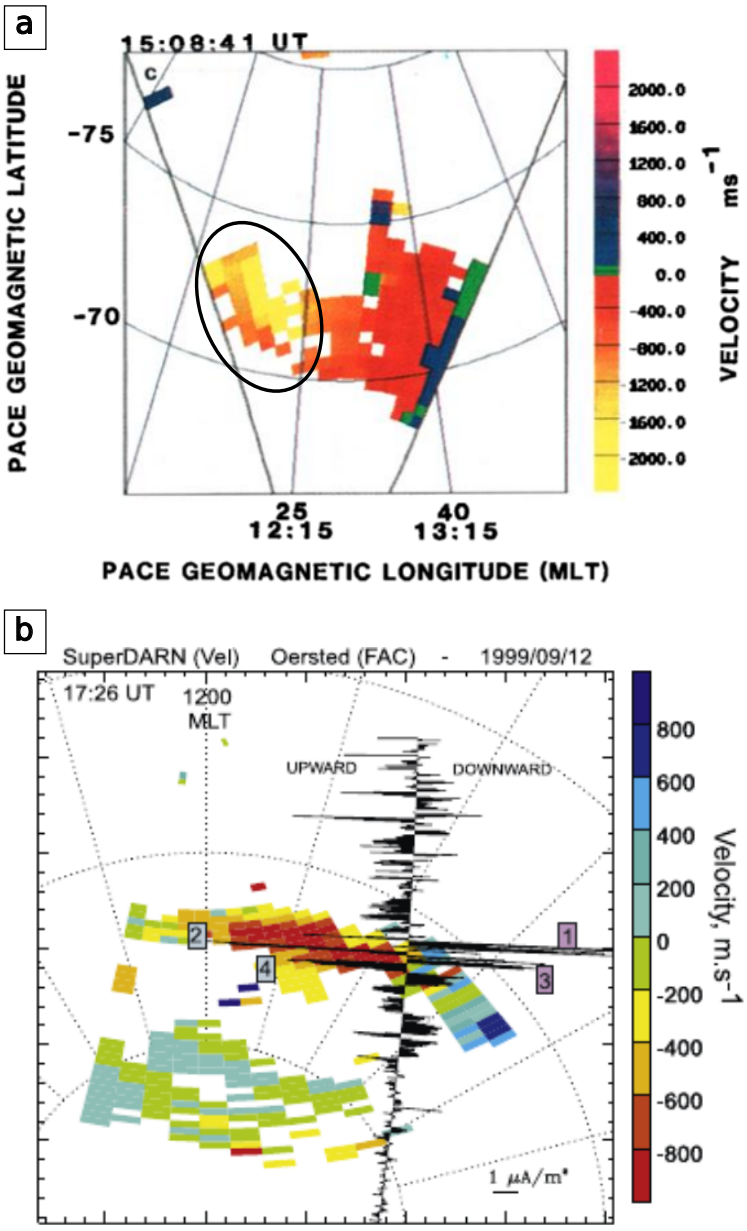

Figure 2.10: Examples of flow channels within SuperDARN data. Panel A shows a flow channel, which is indicated by a black oval, measured by the Halley radar in Antarctica on 6 October 1998 at 15:08 UT [*Pinnock et al.*, 1993]. Panel B shows a flow channel, the region of red cells indicating fast flow away from the radar, measured by the Kapuskasing radar in the Northern Hemisphere on 12 September 1999 at 17:26 UT [*Marchaudon et al.*, 2004]. The Ørsted satellite orbit is shown on the map with calculated field aligned currents plotted perpendicular to the orbit, where labels 1–4 correspond to different small-scale current sheets. Note that noon is at the bottom in panel A and at the top in panel B, and different velocity scales have been used for each plot.

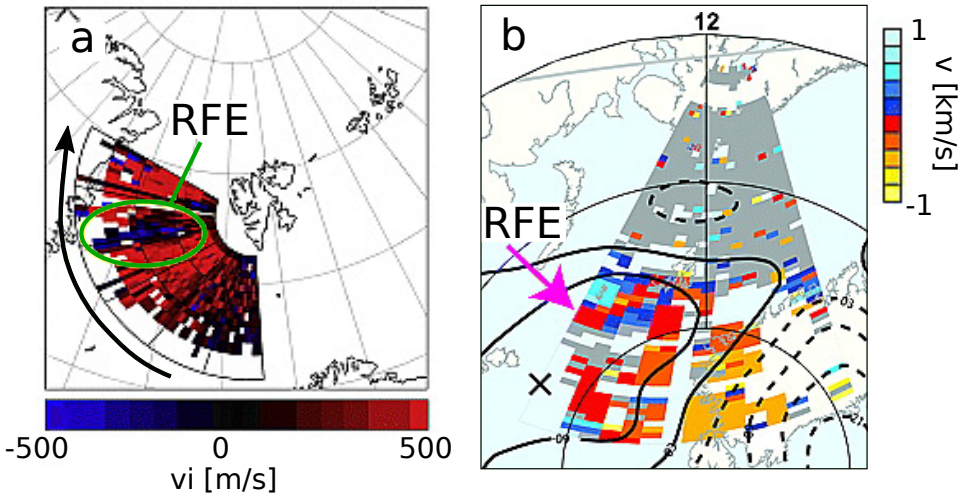

Figure 2.11: Example plots showing Reversed Flow Events (RFEs). Panel A shows measurements from the EISCAT Svalbard radar, which in this case scans in the clockwise direction (as indicated by the black arrow) over the course of ∼3 minutes. Positive ion velocities (red) are directed away from the radar, and negative (blue) are directed towards the radar. The RFE, circled in a green ellipse, is a thin channel of flow moving towards the radar. Panel B shows a RFE within SuperDARN Hankasalmi data. In this case, positive (negative) flows are towards (away) from the radar. The RFE, indicated with a magenta arrow, is the thin channel of red (westwards) velocity embedded in blue (eastwards) background flow. Convection contours are indicated by solid and dashed lines. Figures adapted from a) *Rinne et al.* [2007] and b) *Oksavik et al.* [2011].

supports the theory that the PIFs map to newly reconnected field lines at the dayside magnetopause, as the flow is still dominated by the field tension effect associated with IMF By.

2.9.3 Reversed Flow Events (RFEs)

The flow directions of all the flow channels discussed have so far been in the same direction as the large-scale ionospheric convection. Using the EISCAT Svalbard Radar (ESR), *Rinne et al.* [2007] discovered a new type of flow channel near the cusp inflow region, where the enhanced flow opposed the IMF By induced magnetic tension pull on newly opened field lines, and was therefore in the opposite direction to the background convection. They named this feature a Reversed Flow Event (RFE), which characterises a ∼100-200 km wide East-West (E-W) elongated flow channel that extends out of the ESR field-of-view (600 km) with an average duration of ∼18 minutes. *Oksavik et al.* [2011] later observed several examples of RFEs within SuperDARN data. Examples of observations by *Rinne et al.* [2007] and *Oksavik et al.* [2011] are presented in Fig.2.11.

The *Southwood* [1987] model (described in Section 2.9) predicts that there should be return flows on either side of the center flux. If RFEs were signatures of these return flows, they should be generated in pairs. However, *Rinne et al.* [2007] noted only

one return flow, or two that developed at different instances and must be assumed to be linked to separate FTEs. To explain these observations, which occur during significant IMF By conditions, they propose an asymmetric version of the *Southwood* [1987] model. In this case, only the poleward cell of the *Southwood* [1987] model becomes observable, as flow on the equatorward side lies close to the adiaroic OCB, across which plasma cannot flow. Later observations by *Moen et al.* [2008] showed for every RFE, there was a thin auroral form aligned with the clockwise convection reversal. They suggest two alternative explanations to the *Southwood* [1987] model interpretation. Either RFEs are located between two large-scale current loops, or RFEs are the ionospheric footprint of an inverted-V type coupling region. These two explanations may also be related to each other, but further research is required to determine the exact RFE driver.

2.10 Nightside Flow Channels

Flow channels have also been observed in association with optical features within and close to the nightside auroral oval. As on the dayside, these features have been suggested to be driven by reconnection, except now the key region involved lies within the magnetotail instead of the dayside magnetopause. Specifically, nightside flow channels have been associated with poleward boundary intensifications (PBIs) [*Zou et al.*, 2014], auroral streamers [*Gallardo-Lacourt et al.*, 2014], and auroral substorms [*Nishimura et al.*, 2010a,b; *Ohtani et al.*, 2018].

2.10.1 Poleward Boundary Intensifications & Auroral Streamers

PBIs are a rapid, localised brightening at or near the poleward boundary of the nightside auroral oval, which occur during all levels of geomagnetic activity [*Lyons et al.*, 2011]. *Zesta et al.* [2002] investigated the two-dimensional structure of PBIs and found that they can appear as arcs that are aligned North-South (N-S), East-West (E-W), or tilted, or as more complicated structures, such as beads, swirls, and patches. Thin features called auroral streamers can stem from PBIs, extending toward the equatorwards edge of the auroral oval [*Henderson et al.*, 1998]. The orientation of the streamer may be N-S, E-W, or a mixture of both. The streamers follow the convection pattern and are turned azimuthally when they approach the equatorward boundary of the auroral oval [*Kauristie et al.*, 2003]. The distinction between PBIs and auroral streamers is not well defined, just as the definitions of PBIs and streamers themselves are not well defined. This introduces ambiguities between the two phenomena as there is not a clear, definite point in their evolution where PBIs can then be classified as streamers. However, in general, PBIs are considered to be transient auroral intensifications at the poleward boundary of the auroral oval, while auroral streamers are arcs that are approximately aligned in the N-S direction [*Farrugia et al.*, 2001; *Zesta et al.*, 2011].

A statistical study by *Zou et al.* [2014] using SuperDARN and All Sky Imager data found that PBIs and flow channels were associated in 90% of cases. These flow channels extended from the polar cap region on open field lines towards the poleward boundary of the auroral oval, where the PBI was located. The flow channel either occurred simultaneously with the PBI, or one minute before the PBI during times when

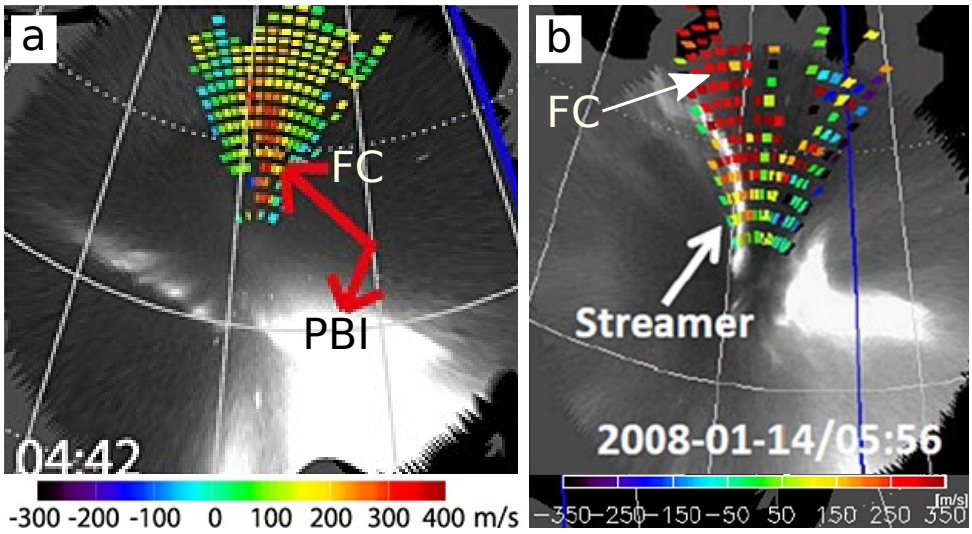

Figure 2.12: Examples of flow channels observed in SuperDARN Rankin Inlet data with optical features shown in white light from the THEMIS All Sky Imager at Rankin Inlet. Panel A shows a flow channel (FC) moving toward the auroral oval in conjunction with a poleward boundary intensification (PBI) [*Zou et al.*, 2014]. Panel B shows a thin North-South aligned auroral streamer with a flow channel on the eastern edge [*Gallardo-Lacourt et al.*, 2014]. Positive/negative flows indicate flows towards/away from the radar.

8 second resolution SuperDARN data were available, as opposed to 1 or 2 minute resolution data. An example of a FC-PBI event from this study is shown in Fig.2.12a. *Zou et al.* [2014] suggest that these results indicate that as the flow channel reaches the OCB, its magnetospheric counterpart in the magnetotail lobe triggers nightside reconnection. They suggest that PBIs can be the ionospheric manifestation of the association between flow channels in the polar cap/lobe region, magnetotail reconnection and fast flows in the plasma sheet when mapped to the ionosphere.

PBIs can develop into N-S aligned auroral streamers. *Gallardo-Lacourt et al.* [2014] used SuperDARN data and All Sky Imager data to confirm that equatorward flow channels were associated with streamers in ∼90% of 135 cases. The equatorwards flows had an average width of 75 km and were located 58 km to the east of the streamer. An example of a FC-streamer event from this study is shown in Fig.2.12b. These flows have been suggested to be the ionospheric signature of longitudinally localised earthward flow bursts in the plasma sheets, called Bursty Bulk Flows (BBFs) [*Angelopoulos et al.*, 1992; *Henderson et al.*, 1998; *Xing et al.*, 2010]. BBFs are triggered by magnetotail reconnection and play a key role in flux transport processes in the magnetosphere. Note that in both Fig.2.12a and b, the velocity does not reach over 400 m/s. These speeds are still considered fast as the location of the echos are within the first 11 range gates of the RKN radar. These short range echos likely scatter from the E-region ionosphere, where flows cannot exceed the ion acoustic speed (∼400 m/s) [*Koustov et al.*, 2005].

2.10.2 Nightside Flow Channels & Substorm Onset

Nishimura et al. [2010b] suggests that PBIs, streamers and their associated ionospheric flow and current systems could play an important role in the initiation of substorm onset. They present statistics and event studies that show the following sequence of events: PBIs develop into N-S aligned auroral streamers, the streamers propagate towards the equatorwards arc in the auroral oval, and a substorm onset is triggered. However, *Ohtani et al.* [2018] highlights that caution must be taken in the interpretation of observations of PBIs and streamers. They point out that streamers and PBIs have no clear definition, which can lead to different kinds of phenomena being identified as PBIs. For example, some studies focus on new arcs that quickly diminish and others on events where the aurora is dynamic for several minutes. PBIs also evolve in many different ways [*Zesta et al.*, 2002], and although much attention has been directed to the type of PBIs that produce streamers, it is unknown if all types of PBIs have the same cause or are driven by completely separate processes. Also, in many cases the poleward boundary of the auroral oval is difficult to identify visually and only in very few cases are spacecraft conjunctions available to validate the boundary with particle precipitation measurements [*Zou et al.*, 2014]. *Forsyth et al.* [2020] also points out that magnetic mapping using available models is rather uncertain, and is particularly challenging at the outer edge of the auroral oval. Here, small changes in latitude can map to large distances downtail and therefore, determining the magnetospheric regions that are linked to PBIs and streamers may be challenging and could be easily confused as the phenomena are spatially close to one another in the ionosphere.

The concern of *Ohtani et al.* [2018] on the onset sequence proposed in *Nishimura et al.* [2010b] that is most relevant to this thesis involves the arrival of the flow channels at the nightside auroral oval. *Zou et al.* [2014] suggests that flow channels and PBIs are linked through magnetotail reconnection. *Ohtani et al.* [2018] suggest that an alternate (or additional) mechanism may be at play. When the flow channel approaches the boundary, its associated E-field could drive ionospheric currents which diverge and converge at the boundary due to the sharp increase in ionospheric conductivity from the polar cap to the auroral oval in this region. PBIs could then result from electron precipitation in conjunction with the upwards field aligned current [*Ohtani and Yoshikawa*, 2016]. This process is called ionospheric electrostatic polarisation. It is currently unknown if magnetotail reconnection, ionospheric electrostatic polarisation, or a combination of the two are the consequence of flow channels approaching the nightside auroral boundary. This problem could potentially require the presence of more spacecraft missions at a range of distances within the magnetotail to fully resolve [*Forsyth et al.*, 2020].

2.11 Flow Channels on the Flanks

In contrast to the view that momentum transfer from the magnetosphere to the ionosphere is restricted to 'newly-opened field lines' [*Lockwood et al.*, 1990], flow channels have been reported deeper inside the polar cap on 'old-open field lines'. These are field lines that have reconnected >10 minutes previously and drifted downstream of the cusp. This type of flow channel has been attributed to the solar wind magnetosphere

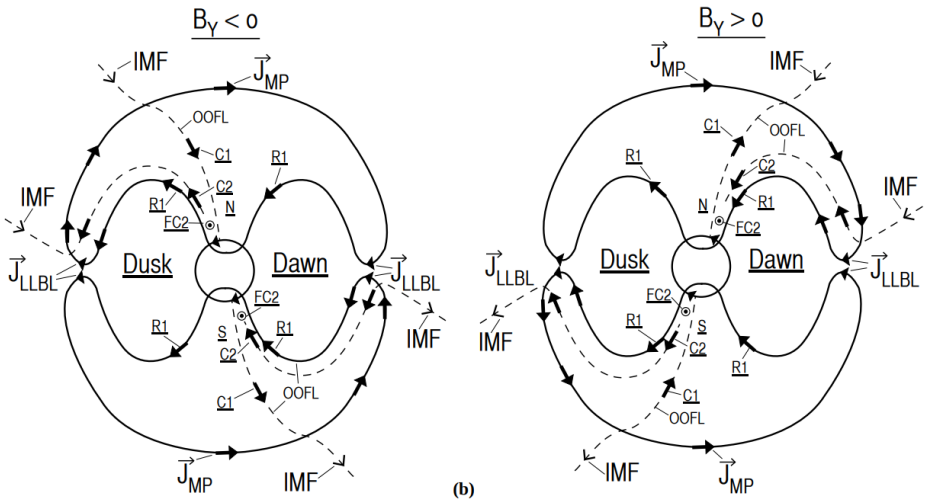

Figure 2.13: Schematic of the current systems related to FC 2, with a view from the magnetotail towards the Sun. The configuration in both the Northern Hemisphere and the Southern Hemisphere are shown for left) -IMF By and right) +IMF By. Current systems are labelled for the magnetopause (J_{MP}), the low latitude boundary layer (LLBL) and for the R1/R2 and C1/C2 systems. The particular fields involved with FC 2 are represented by dashed lines, occurring on old open field lines (OOFL). Figure from *Sandholt and Farrugia* [2009].

dynamo in the high-latitude boundary layer [*Farrugia et al.*, 2004; *Sandholt and Farrugia*, 2007; *Sandholt et al.*, 2004]. The feet of the field lines are then located in mantle or polar rain precipitation. Using data from DMSP satellites under intervals of stable IMF (during interplanetary coronal mass ejections), *Sandholt and Farrugia* [2009] detected flow channels between 6–9 MLT and 15–18 MLT that were a few hundred km wide and travelled anti-sunward at velocities between 1.5-3 km/s. The location of the channel (dawn or dusk) depended on the sign of IMF By, occurring on the dawn side for +IMF By and the dusk side for -IMF By, with the reverse true in the Southern Hemisphere. The corresponding currents and fields around the flow channel for +IMF By and -IMF By in both hemispheres are shown in Fig.2.13. The flow channel, marked as FC 2, occurs on old-open field lines (marked as OOFL), and is the result of the Pedersen current closure of the C1/C2 system (defined by *Sandholt and Farrugia* [2009], shown in Fig.2.13) in the ionosphere and therefore maximises at the interface between the C1/C2 Birkeland currents. Using particle data from the DMSP satellites, *Sandholt and Farrugia* [2009] showed that C1 is distributed over a wide latitudinal range in the polar cap in a region of polar rain precipitation and connects to the magnetopause current at high altitudes. They also showed that C2 flows on the poleward side of the convection reversal boundary, in the same direction as the R1 current. The precipitation associated with C2 is boundary plasma sheet and Low Latitude Boundary Layer (LLBL) type precipitation.

There have also been observations of flow channels occurring on closed field lines. In the mid-latitude, dusk/night ionosphere, strong polewards electric fields equatorward of the auroral oval drive a phenomenon named sub-auroral polarisation streams

(SAPS) [*Foster and Burke*, 2002]. The polewards electric fields are thought be due to the separation of the inner electron and ion boundaries of the ring current in response to enhanced magnetospheric convection. A localised (1–2°) enhancement often called a sub-auroral ion drift (SAID) is observed within the SAPS, predominantly between 18-2 MLT at the equatorwards edge of the auroral oval, which can exceed 1 km/s in the westward direction [*Spiro et al.*, 1979]. In addition to SAPS/SAIDs, there have been reports of flow bursts on closed field lines within the sunward return flow region at lower latitudes in the morning and/or afternoon sectors [*Moen et al.*, 1995]. These flow occur during periods of transient dayside reconnection and are consistent with the *Cowley and Lockwood* [1992] model of flow generation by pulsed reconnection.

2.12 Polar Cap Arcs (PCAs)

Polar cap arcs (PCAs) have also been associated with flow channels. PCAs are thin bands of auroral emission caused by precipitating electrons. They occur predominantly under northward IMF and geomagnetically quiet conditions [*Berkey et al.*, 1976; *Gussenhoven*, 1982]. These arcs can often be aligned in the direction of the sun, and have consequently also been referred to as Sun-aligned arcs. PCAs usually connect to the nightside auroral oval in the midnight or dawn/dusk sectors, but on occasion also connect to the dayside oval, spanning the entire polar cap [*Frank et al.*, 1982]. There are many types of polar cap arcs that each have different shapes and motions. Bending arcs, for example, are faint polar cap arcs that form under IMF By-dominated conditions and in most cases IMF Bz is close to zero. While the tailward arc end remains attached to the oval, the dayside arc end can detach from the oval and move successively antisunward before fading within tens of minutes [*Carter et al.*, 2015; *Kullen et al.*, 2015].

Zou et al. [2015a] identified 34 polar cap arcs using all sky imagers and used the poleward directed SuperDARN radars at Rankin Inlet and Inuvik to measure the ionospheric convection velocity. They observe a good correspondence between polar cap arcs and equatorward flow channels on the nightside when radar echos were available. They note that as polar cap arcs extend towards and connect to the nightside oval, PBIs are triggered in 85% of the cases. The PBIs occur within 10 mins of the connection and $\pm$ 1 hr MLT from the location of contact. They suggest that extensive monitoring of the ionospheric flow channels associated with the PCAs as they stretch towards the auroral oval could then allow for a forecast of the nightside oval disturbances.

2.13 The Propagation & Evolution of Dayside Transients

Attempts have been made to track the ionospheric response to FTEs as the associated mesoscale flow systems move away from the polar cap boundary and into the polar cap. One way this can be achieved is by monitoring the optical signatures of FTEs, which are known as Poleward Moving Auroral Forms (PMAFs) [*Fasel et al.*, 1993; *Horwitz and Akasofu*, 1977; *Vorobjev et al.*, 1975]. PMAFs are characterised by a brightening in the aurora near the equatorward boundary of the dayside aurora (known as equatorward boundary intensifications (EBIs)), followed by a poleward motion, ending in a fading

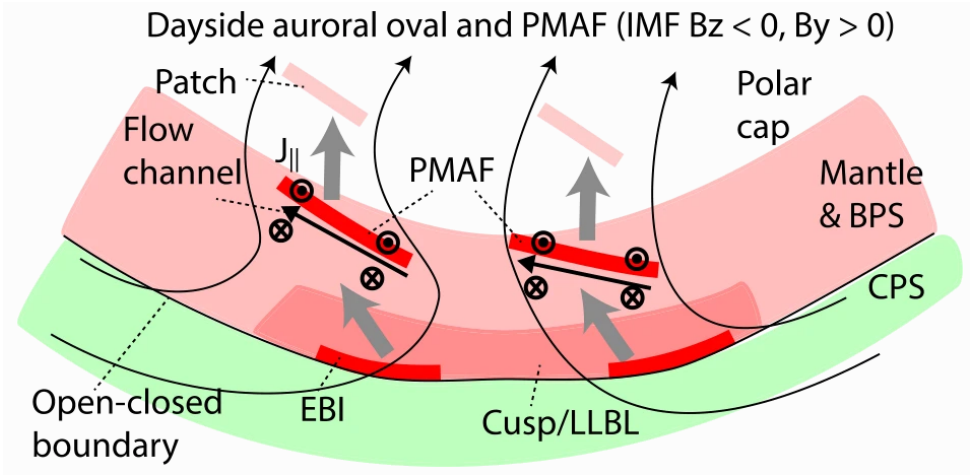

Figure 2.14: Schematic of the evolution of a PMAF from an EBI into a patch and the associated currents and flows. In this case the PMAF occurs under -IMF Bz and +IMF By conditions. Figure from *Frey et al.* [2019].

of the PMAF ∼500 km poleward of its formation point [*Fasel*, 1995; *Sandholt et al.*, 1989]. The auroral emissions due to PMAFs appear in both the red (630 nm) and green (557.7 nm) lines, but are most prominent in the red line. The emissions are caused by particle precipitation in the region of upward FACs on the appropriate flank of flow channels. In the Northern Hemisphere, for -IMF By the flow direction in the flow channel is duskward, the configuration of the current systems are shown in Fig.2.9, and the emissions and upwards FACs are located on the equatorward boundary of the flow channel. For the case of +IMF By in the Northern Hemisphere, the flow direction in the flow channel is dawnwards and the upwards FACs and emissions are located on the poleward boundary of the flow channel, as in Fig.2.14. The opposite case is true in the Southern Hemisphere. PMAFs are typically 2-10 min in duration with a periodicity of 5–15 min [*Sandholt et al.*, 1986] and a poleward propagation speed of ∼1 km/s [*Oksavik et al.*, 2005].

Lorentzen et al. [2010] observed a series of PMAFs with in-situ data from the Investigation of Cusp Irregularities 2 sounding rocket, data from the EISCAT Svalbard Radar, and optical data from all sky cameras and a meridian scanning photometer. They noted that in relation to each PMAF, a patch of enhanced ionisation moved into the polar cap. When measured in the 630 nm emission line, these regions of enhanced electron density in the F-region ionosphere are known as airglow patches. The enhancement in the 630 nm line is due to excited oxygen atoms that are created by slow recombination (around 1 hour) between electrons and molecular oxygen ions [*Weber et al.*, 1986]. This evolution is shown in Fig.2.14 for a -IMF Bz and +IMF By configuration. An EBI is closely followed by a PMAF and its associated flow channel, which then propagates poleward and evolves into an airglow patch when the 557.7 nm precipitation associated with the PMAF fades.

This diagram seems to suggest that the flow channel fades with the PMAF and is not present deeper into the polar cap. This is an open area of research and the precise

way in which the mesoscale flow features move from the dayside and over the polar cap, and what the magnetospheric drivers of such features are is unknown [*Lyons et al.*, 2016]. *Milan et al.* [2000] suggested that an initially confined region of newly opened flux will spread out as it is transported and assimilated into the polar cap. However, *Rinne et al.* [2010] observed a sequence of flow channels in the cusp region resulting from alternating IMF By positive and IMF By negative driving conditions. These flow channels were stacked next to each other and remained separated as they moved into the polar cap. This separation remained until the magnetic tension forces associated with the IMF By component relaxed and the FACs separating the flow channels were no longer driven.

Zou et al. [2015b] also observes that flow channels can persist deeper into the polar cap, and suggests that they coexist with airglow patches as they traverse the polar cap. They show that within a case study of 93 airglow patches, 67% of the patches were related to flow channels for over 70% of their propagation. These flow channels are however at a lower velocity than those typically seen in the dayside cusp region, moving with the patches at speeds of 600 m/s, which was ∼200-300 m/s higher than the background flow. Although it is difficult to obtain appropriate simultaneous coverage of both the plasma flows and the optical signatures of the patches across the entire polar cap, *Nishimura et al.* [2014] showed a case of nearly continuous observations of a dayside PMAF evolving into an airglow patch, drifting to the nightside, and triggering a PBI at the nightside auroral oval. Analysis of line-of-sight SuperDARN data from radars located close to the cusp and nightside oval suggest that flow channels are associated with the patch, with a 900 m/s magnitude near the dayside cusp and a 500 m/s magnitude close to the nightside auroral oval. *Goodwin et al.* [2019] uses conjunctions between the Cluster spacecraft and the Resolute Bay image to investigate the drivers for the system of currents and flow channels surrounding airglow patches. Their observations suggests that a magnetospheric driver is responsible, where more visible associated lobe structures are observed for newly-created, luminous patches than for older, fading patches. However, further observations and statistical studies are required to fully understand the role, characterisation, and link between flow channels in different areas of the polar cap.

2.14 The Sandholt & Farrugia (SF) Framework

The past few sections highlight that flow channels have been associated with a multitude of different features at a range of different MLT/MLATs. To study flow channels at different stages within the Dungey cycle, works mainly by Sandholt and Farrugia [*Sandholt and Farrugia*, 2009; *Sandholt et al.*, 2010] have classified flow channels into different categories. Fig.2.15 shows a schematic from *Andalsvik et al.* [2011] that depicts the fields and flows related to the various categories of flow channels at different stages in the Dungey cycle. The illustration is based on a combined high-latitude boundary layer (HBL) - low-latitude boundary layer (LLBL) - tail plasma sheet model. The flow channel categories include: FC 1 (red arrows), FC 2 (blue arrows), FC 3 (green arrows), FC 4 (yellow arrows) and FC 0 (not shown in the diagram). From now on the collection of these flow channels will be referred to as the SF framework.

FC 1 and FC 2 are dayside driven flow channels. The difference between the two

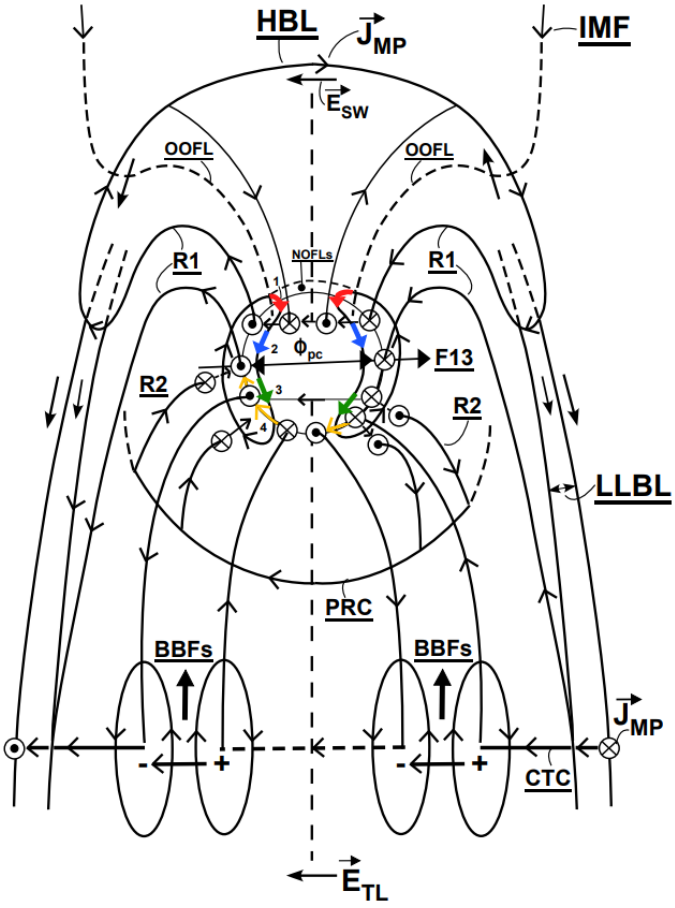

Figure 2.15: Schematic of the Sandholt & Farrugia framework for flow channels at different stages in the Dungey cycle. FC 1, 2, 3, and 4 are marked by red, blue, green and yellow arrows respectively. Upwards currents are represented by dots and downward by crosses. Newly Opened Field Lines (NOFL) and Old Opened Field Lines (OOFL) are labelled, as are the High-latitude Boundary Layer (HBL) and Low-latitude Boundary Layer (LLBL) regions. The current systems are labelled for the magnetopause (J_{MP}), Partial Ring Current (PRC), Cross Tail Current (CTC), and Birkeland currents (R1 and R2). The electric fields of the solar wind and tail lobes are labelled E_{SW} and E_{TL} respectively. The electric fields and currents surrounding Bursty Bulk Flows (BBFs) are also displayed in the magnetotail. Figure from *Andalsvik et al.* [2011].

lies in the duration since the field lines experienced dayside reconnection. FC 1 occurs on newly opened field lines (NOFL) close to the dayside OCB, with time since reconnection <10 minutes. This category contains flow channels such as FCEs and PIFs. FC 2 occur on old open field lines (OOFL), which reconnected ∼10-20 minutes previously. These field lines are seen in the vicinity of the dawn and dusk flanks. FC 2 characteristics are explained in detail in Section 2.11.

FC 3 and FC 4 are driven by processes on the nightside and their field lines are connected to the tail lobe and plasma sheet respectively. FC 3 occurs on open field lines that are located immediately polewards of the nightside auroral oval and are related to the closure of lobe flux [*Wang et al.*, 2010]. This category contain the equatorward flows seen in relation to PBIs (Section 2.10.1). FC 4 are associated with westward electrojet enhancements and auroral streamer events (Section 2.10.1) and their magnetospheric link to bursty bulk flows is shown in the diagram. FC 4 can be seen to extend towards the dusk flank on closed field lines and therefore also contains the SAPS/SAIDs category of flow channel (Section 2.11). Lastly, FC 0 (not shown in the diagram) occurs on closed field lines in the dayside return flow region, and can therefore be associated the category of flow channel observed by *Moen et al.* [1995] (Section 2.11).

2.15 Unresolved Problems & Open Questions

The previous sections on ionospheric flow channels have summarised the research in the field so far. Many different types of flow channels have been identified within the polar cap with various associated optical signatures. The SF framework provides the basis to begin to classify these flow channels in relation to their stage of evolution, with respect to the Dungey cycle. The majority of these studies focus on case studies using DMSP passes to investigate flow channels [*Andalsvik et al.*, 2011; *Sandholt and Farrugia*, 2009]. However, the data have a limited coverage both temporally and spatially as the observations are limited to the few minutes that the satellite traverses the FC and only along the satellite track. While case studies have been invaluable in providing incite about certain types flow channels, they are limited to the particular solar wind and ionospheric conditions at the time of measurement. When statistical case studies have been used, they focus only on a range of certain MLT/MLATs.

In this thesis, an algorithm is developed that can detect flow channels in both hemispheres, at all MLTs, with an extensive MLAT coverage in the high-latitude polar cap regions. The algorithm targets fast flow channels >900 m/s, as during these times there is a high degree of solar-wind-magnetosphere-ionosphere coupling. The following knowledge gaps will be addressed:

- What is the characteristic velocity, duration, and width of ionospheric flow channels in the polar cap?
- What is the distribution of flow channels within the polar cap, as open field lines pass through different stages of the Dungey cycle?
- What solar wind conditions drive fast flow channels, and how does the distribution of flow channels change for different IMF orientations?

- How important is the role of flow channels in the transportation of flux across the polar cap?

The instrumentation and methods required to address these questions are presented in Chapter 3.

Chapter 3

Instrumentation & Methods

3.1 Radar Measurements of Ionospheric Flows

The Super Dual Auroral Radar Network (SuperDARN) is an international chain of high-frequency coherent scatter radars, which are used to measure horizontal plasma flow in the F-region ionosphere [*Chisham et al.*, 2007; *Greenwald et al.*, 1995]. The fields-of-view (FOVs) of the radars are each approximately 2500 km in range and 52° in azimuth, therefore covering large areas in both hemispheres, as shown in Fig.3.1. The FOVs are coloured green, blue, and red to indicate polar, high-latitude and mid-latitude radars and a unique three letter station ID is indicated at the position of each radar. Particularly relevant to this thesis, are the Longyearbyen (LYR), Rankin Inlet (RKN), Inuvik (INV) and Clyde River (CLY) radars in the NH and the South Pole Station (SPS), Dome C (DCE), McMurdo (MCM) and Zongshan (ZHO) radars in the SH.

Each SuperDARN radar is a monostatic, phased-array radar with a main array and an interferometer array. Fig.3.2 shows a section of the 16 twin-terminated folded dipole antennas in the main array of the SuperDARN Longyearbyen radar. The main array can both transmit and receive, whereas the interferometer array, not included in the image, consists of 4 antenna with receive capability only and is used for elevation angle determination [*Milan et al.*, 1997a].

Each radar is low power (around 10 kW) and operates continuously throughout the year. Electronic phasing is used to direct 3° wide beams through 16–24 longitudinally-spaced directions, spanning the entire FOV. Each beam is divided into range gates of 45 km resolution. There are various modes of possible operation. In common mode, there is a typical dwell time of 3 seconds or 7 seconds on each beam, corresponding to a full azimuthal scan time of 1 or 2 minutes. Typically, the radars run in common mode for 50% of each month. Another mode used in this thesis is known as two-f-sound mode. In the two-f-sound mode, the radar completes a scan every 1 minute, but alternates between 2 different transmission frequencies. The remainder of the available time is allocated to special and discretionary modes, where a range of different beam scanning or beam swinging patterns are possible upon request.

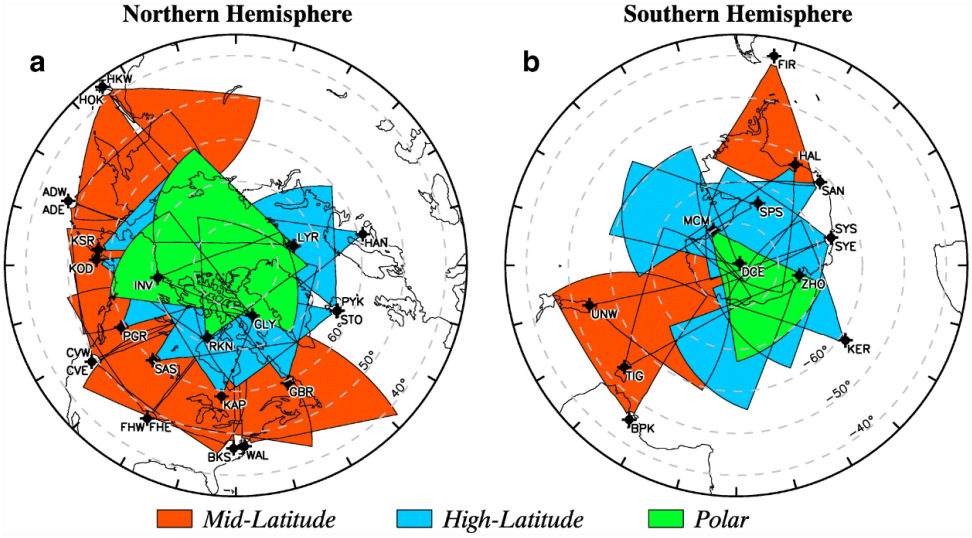

Figure 3.1: Fields-of-view of the SuperDARN radars in a) the Northern Hemisphere and b) the Southern Hemisphere. The fields-of-view are coloured based on latitude, where green, blue, and red represent polar, high-latitude, and mid-latitude radars respectively. The radar codes are indicated at the location of each radar. Image from *Nishitani et al.* [2019].

Figure 3.2: Image of a section of the main antenna array of the SuperDARN Longyearbyen radar. Image courtesy of *Mikko Syrjäsuo (UNIS)* [2017].

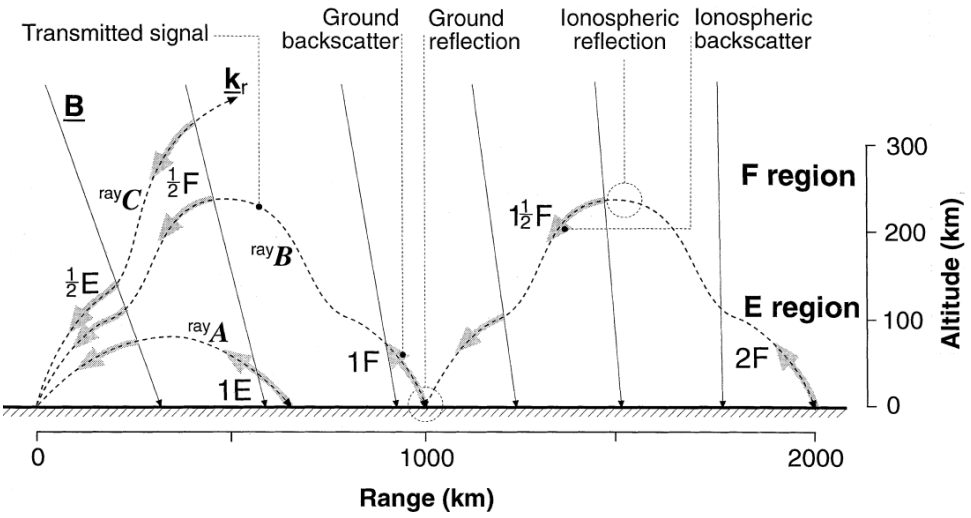

Figure 3.3: Schematic showing possible radio wave propogation modes and regions where backscatter can occur. Half integers indicate ionospheric backscatter, while whole numbers are ground scatter. Three rays are shown, which are elaborated on within the text. Figure adapted from *Milan et al.* [1997b].

3.1.1 High Frequency Radio Wave Propagation & Backscatter

SuperDARN radars are frequency agile, operating within the high frequency range (8-20 MHz). This range was chosen as at high latitudes, where Earth's magnetic field is near-vertical, the wave can be continuously refracted in the ionosphere until it propagates almost horizontally. The wave thus becomes orthogonal to the Earth's ambient magnetic field, satisfying the Bragg condition in Eqn.3.1, in both the E- and F-regions and ionospheric backscatter can be observed. At the point of reflection when the wave first encounters the E- or F-region ionosphere, only a fraction of the wave is reflected, while the rest continues along its path and can be refracted back towards the ground. At ground incidence, some power is scattered back along the propagation direction but most is reflected forward back up towards the ionosphere. Is it therefore possible to observe scatter from both the ground and ionosphere at different distances from the radar and up to far ranges.

Some example propagation modes are shown in Fig.3.3. The figure shows three different rays, labelled rays A-C, which can propagate either individually or simultaneously at the displayed ranges depending on the electron density profile in the ionosphere. The numbers refer to how many 'hops' the beam has completed and the letter (E or F) represents the ionospheric region the scatter originates. Groundscatter is denoted by whole numbers, while ionospheric scatter is represented by half-integers. Ray A has a low elevation angle, backscattering from the E-region and the ground. Ray B has a slightly higher elevation angle and reflects in the E-region, producing backscatter in both the E- and F-regions for both 1 and 2 hops. Ray C has the highest elevation angle and penetrates the ionosphere before sufficient refraction can occur that will allow the ray to reflect. For SuperDARN radars, the furthest detectable ionospheric scatter is

3.5 hop, but generally the majority of the scatter comes from 0.5 and 1.5 hop [*Milan et al.*, 1997b].

The agile nature of the radar operating frequency allows adjustments to be made based on predictable changes in the ionospheric conditions. For example, different frequencies are usually used between day and night due to the different levels of ionisation present in the ionosphere. A higher frequency wave that achieved orthogonality to the magnetic field in the daylight hours is more likely to penetrate the ionosphere and continue into space during the weakly-ionized ionosphere at night.

SuperDARN radars receive signals that have been backscattered from plasma density structures in the ionosphere, known as irregularities. In the F-region, the dominant instability mechanism that creates irregularities is the gradient-drift instability [*Hosokawa et al.*, 2001]. This instability is generated in the presence of electron density gradients and acts on the edges of regions of enhanced electron density, produced primarily by solar EUV or auroral precipitation. This mechanism results in the production of smaller-scale field-aligned, irregularities travelling at the **E** x **B** drift velocity [*Ossakow and Chaturvedi*, 1979].

The SuperDARN radars are able to detect these irregularities through Bragg scattering, when the transmitted radio wave achieves orthogonality to the magnetic field [*Greenwald et al.*, 1995]. To achieve this, the Bragg condition must be satisfied:

$$\lambda_r = 2\lambda_{irr} \sin\left(\frac{\theta}{2}\right), \tag{3.1}$$

where λ_r is the wavelength of the transmitted wave, λ_{irr} is the distance between the irregularities, and θ is the angle of the scattered wave relative to the incident wave in the plane perpendicular to the magnetic field. When the Bragg condition is satisfied, incident radio waves scattered by the irregularities add coherently, constructive interference occurs, and a strong signal is received back at the radar. For this reason, the name of this type of scatter is 'coherent scatter'. In order for the transmitted wave to be received back at the radar, the angle must be set to $\theta = 180$, which then means that

$$\lambda_{irr} = \frac{\lambda_r}{2}. \tag{3.2}$$

Coherent scatter radars therefore measure strong backscatter when the irregularity width is is half that of the wavelength of the transmitted wave, which for SuperDARN radars occurs in the decameter range.

3.1.2 SuperDARN Parameters

The three main parameters measured by the SuperDARN radars are the backscatter power, line-of-sight (LOS) doppler velocity, and spectral width. To obtain these values, the radars transmits a pulse sequence containing 7 or 8 unevenly-spaced 300 microsecond pulses. Different combinations of these pulses can then form the different lags of an autocorrelation function. The pulse sequences are averaged together over a 3 second integration time for each beam to reduce noise and gain a statistically significant signal. Weighted linear least-squares regression is applied firstly to the magnitude of the ACF to obtain the power and spectral width parameters, and secondly to the phase of the ACF to obtain the LOS doppler velocity [*Nishitani et al.*, 2019].

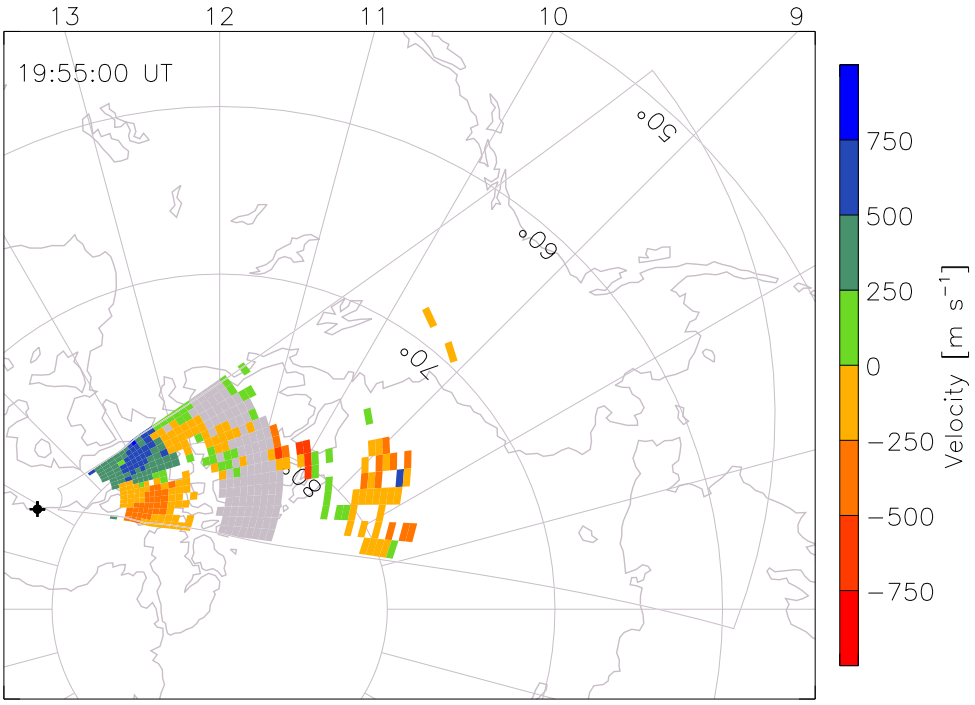

Figure 3.4: A field-of-view plot in MLT/MLAT coordinates from the Clyde River SuperDARN radar at 19:55 UT on 4 March 2016. The velocity at each beam and range gate is shown, where positive (negative) velocities represent flows towards (away) from the radar. The figure was generated using online plotting tools [*VT SuperDARN*, 2020].

3.1.3 SuperDARN Data Visualization

Field-Of-View Plots

A useful way of visualizing the measured parameters of the radar is to use field-of-view (FOV) plot, as shown in Fig.3.4. This plot shows the LOS velocity for each range gate along all 16 beams of the Clyde River SuperDARN radar. Similar plots can also be generated for the power and spectral width. Positive velocities indicate motion towards the radar along the beam direction and the opposite is true for negative values. Ground scatter values are marked in grey and typically identified by slow speeds (velocity less than 30 m/s) and narrow spectral widths (less than 35 m/s). In this plot, the band of ground scatter surrounding 12 MLT clearly marks the 1 hop region, where closer ionospheric scatter is 0.5 hop and further is 1.5 hop. It is also worth noting that large sections of the field-of-view remain empty as ionospheric conditions at these range gates do not support backscatter.

Convection Maps

The velocity data from all radars in the network can be combined to produce a global-scale view of the ionospheric convection. To achieve this goal, *Ruohoniemi and Baker*

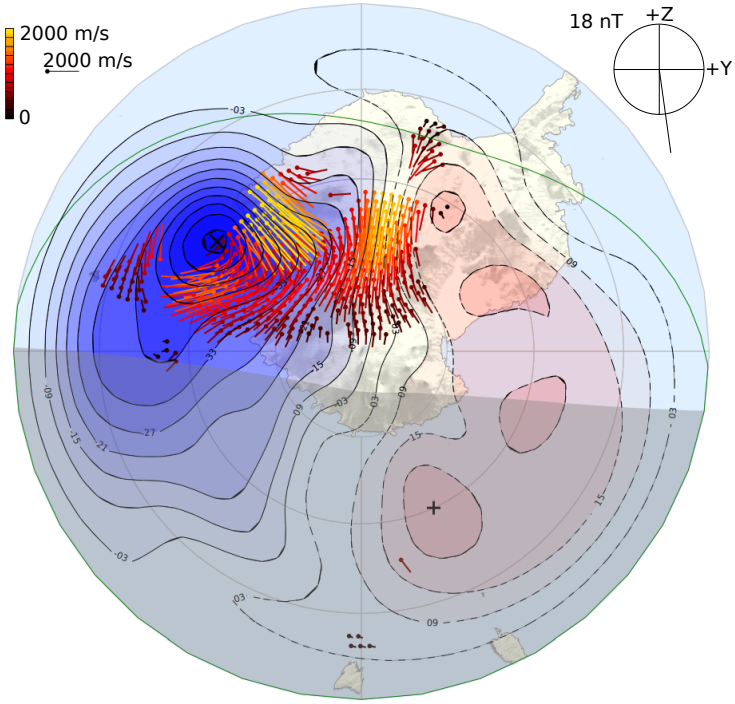

Figure 3.5: Convection map for the Southern Hemisphere on 20 March 2001 from 13:50-13:52 UT. The map is in MLAT/MLT coordinates, where noon is to the top and dusk is to the left. Small coloured dots show the location of the velocity vectors and the length and colour of the lines represent the magnitude of the flow. A colour bar and reference vector are shown in the top left. The equipotential contours are shown for the dusk cell (solid lines, contoured blue) and for the dawn cell (dashed lines, contoured red). The green line represents the Heppner-Maynard boundary. The IMF clock angle is shown in the top right, showing a high magnitude (18 nT) southward IMF. Figure adapted from *Andalsvik et al.* [2011].

[1998] implemented what is now known as the map potential technique. Firstly, the LOS velocity data from each radar is binned into a global grid of approximately equal area cells that measure 1° in geomagnetic latitude. The gridded data are then fitted to an expansion of the electrostatic potential in the ionosphere, Φ, in terms of spherical harmonic functions:

$$\Phi(\theta,\phi) = \sum_{l=0}^{L} \sum_{m=0}^{Min(l,M)} (A_{lm}\cos m\phi + B_{lm}\sin m\phi) P_l^m(\cos\theta), \tag{3.3}$$

where θ and ϕ are the magnetic colatitude and local time, P_l^m are the associated Legendre functions, L and M are the order and degree of the expansion, and A_{lm} and B_{lm} are complex coefficients with dimensions l x m. The electrostatic potential, convection electric field $\mathbf{E}$ and velocity $\mathbf{v}$ are related by

$$\mathbf{E} = -\nabla\Phi; \quad \mathbf{v} = \frac{\mathbf{E}\times\mathbf{B}}{B^2}. \tag{3.4}$$

The result of the map potential technique is shown in Fig.3.5 by a convection map of the northern high-latitude polar region. The blue and red contours map the electrostatic potential, while the velocity vectors are represented by coloured dots to indicate the magnitude of the flow and scaled lines to show the direction. There are large areas in Fig.3.5 that are devoid of data. To ensure that the solution remains realistic in these areas, the velocity data are supplemented with data from a statistical model that provides convection patterns based on prevailing IMF conditions [*Ruohoniemi and Greenwald*, 1996]. In areas where velocity data is present, the data has more weight than the statistical model, allowing the data to constrain the convection pattern in these regions. For example, the IMF clock angle in the top right of Fig.3.5 shows that the IMF is directed southwards without a high By component. In this case, a symmetric twin cell convection pattern pattern is expected. This is the overall pattern we observe in the figure, however the data allows the convection to be displayed in greater detail where velocity data is present, and the cells are warped to account for that in those areas. Finally, the data below the convection boundary, shown in green and otherwise known as the Heppner-Maynard boundary, is given a lower weighting to again allow for a more realistic pattern [*Heppner and Maynard*, 1987]. The cross polar cap potential (CPCP), Φ_{PC}, is the difference in voltage between the centers of the two convection cells in Fig.3.5. It is therefore the maximum potential difference across the polar region and acts as a proxy for the strength of the convection.

3.1.4 Limitations of SuperDARN data

The SuperDARN radars are the main instruments used within this thesis and the flow channel detection algorithm used in Papers I-III is applied to SuperDARN data (described in detail in Section 4.1). It is therefore especially important to consider the limitations and potential sources of error of the data set. The SuperDARN data set has limitations due to radio propagation and space weather environment, hardware, and software and a detailed discussion of these aspects is presented in the following sections.

Radio Propagation & Space Weather Environment

There must be a sufficient amount of ionospheric backscatter available to allow the flow channel and an observable background flow to be detected. This requires that ionospheric irregularities are present to act as targets for the radio waves to scatter from. The high frequency wave propagation environment must also support at least 1/2 hop propagation to be received at the radar and the operational frequency of the radar must be chosen correctly to achieve the reflection conditions [*Milan et al.*, 1997b]. If incorrectly chosen, the rays may penetrate the ionosphere or refract before reaching the ionosphere, which would prevent the detection of the echos from the flow channel.

Significant disruptions to the propagation environment can be caused by space weather phenomena, which can cause absorption in the D-region ionosphere and hinder HF propagation in the E and F-regions by altering the available ionospheric propagation paths. In the case of solar proton events for example, the ionospheric backscatter in the SuperDARN radars can effectively drop to zero for several days [*Bland et al.*, 2018], which would prevent the detection of any flow channels which may have been present during this interval. General ionospheric electron density enhancements by auroral precipitation can also have a similar (but not as prolonged) effect, causing enhanced D-region absorption and a dropout in HF radar backscatter [*Bland et al.*, 2019; *Milan et al.*, 1999].

Resolution Considerations

Another limitation stems from the resolution of the measurements. For common modes of radar operation, the field-of-view is scanned across all beams at a 1 minute resolution and for two-f-sound modes the resolution is effectively 2 minutes as each frequency is separated into its own data set. The beam dwell time is typically 3 seconds. The range gate resolution of 45 km also applies a lower limit to the structures that we are able to resolve. However, the spectral width can be used as an indicator of whether smaller scale, turbulent structuring is present within the flow channel.

The Line-Of-Sight Velocity Component

A problematic limitation is that the SuperDARN radars can only measure the line-of-sight velocity component. Flow channels that travel perpendicular to the beams will therefore not be detected. As the flow channel detection threshold is set very high (900 m/s), the flow must have a large component in the beam direction to be detected. Large scale flows that change over the field-of-view will also be observed as gradually increasing/decreasing velocities due to the line-of-sight limitation.

Extent of Radar Coverage

Another limitation is the radar coverage in relation to the flow channel location. The flow channel must be located centrally within the radar field-of-view so that is possible to detect the steep gradients on either side of the flow channel. If the flow channel occurs in one of the gaps in radar coverage within the SuperDARN network, then it is of course also not possible to detect. These coverage gaps therefore also pose a limitation.

Data Availability & Quality

The SuperDARN network, although it has not always been known by that name, has expanded steadily since the 1980s. Data availability and extent is therefore different for each radar, as they were all built at different times. Paper III makes use of data from several radars in the polar regions, the oldest of which were built in 2008 (Clyde River and Rankin Inlet) and the newest in 2016 (Longyearbyen). The build year is not the only factor on data availability as hardware can fail and structural components can break, which can cause data gaps. In the polar regions, it can take long periods of time before engineers can fix the hardware and structural problems, so these data gaps can be substantial.

The degradation of the radar hardware over time can also contribute to poorer data quality. In addition, some received signals can be interpreted as ionospheric scatter, when in reality they are due to transmitter interference from external radio sources or from thermal noise within the system. Even after software processing, noise is sometimes still present in the data but since it is random, it is usually confined to individual range gates.

Geolocation Uncertainties

There is an element of uncertainty related to the location of the observed backscatter from the SuperDARN radars. This is due to the method of projecting SuperDARN echos using a straight line with a fixed virtual height. This method does not account for variations in the ionospheric electron density and can introduce mapping errors between the backscatter location and the location of the ionospheric plasma irregularities. *Yeoman et al.* [2001] used an ionospheric heater to produce artificially-induced radar backscatter in a known location and used this to provide a range calibration for the SuperDARN radars. They found that the typical ground range errors were $\sim$16 km for 1/2 hop F-region backscatter and $\sim$60 km for 1 1/2 F-region backscatter.

Despite these limitations, SuperDARN is undoubtedly the most appropriate available instrument network to use for this thesis. The distribution of radars across both polar caps, with field-of-views covering large areas at a range resolution of 45 km, provides excellent coverage for detecting flow channels in the polar cap region. The continuous operations of the radars results in a large, 1-2 minute resolution, synchronised data set spanning multiple years. The signatures of flow channels are easily identifiable within the data set, which allows for automation of the processes and makes the choice of events less subjective than manual identification. The available temporal and spatial resolutions are sufficient for the purpose of mesoscale flow channel detection. Through statistical studies, it is possible to determine the key flow channel characteristics. Averaging over the large numbers of events in the statistical studies is also a way to mitigate some errors introduced by the limitations.

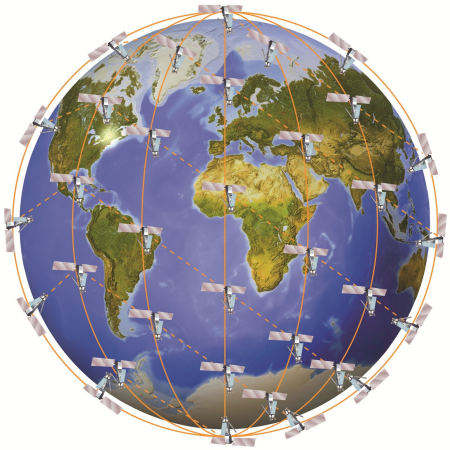

Figure 3.6: A schematic view of the distribution of satellites in the Iridium constellation. Image courtesy of *ESA* [2012].

3.2 Global Measurements of Field Aligned Currents

Magnetometer data from the Iridium telecommunications satellite network can be used to construct maps of current density in the northern and southern polar regions [*Anderson et al.*, 2014]. These maps were used in Paper III to determine if the flow channels were located inside or outside of the polar cap. A schematic view of the network is shown in Fig.3.6, which consists of 66 spacecraft in 6 different polar orbital planes, uniformly spaced in local time by ∼2 hr of MLT, at an altitude of 780 km. There are 11 satellites in each orbital plane, each with an orbital period of 104 minutes. The dense constellation provides global coverage of the Earth's magnetic field. Although the onboard 3-axis, vector fluxgate magnetometers were originally intended to monitor the attitude of the spacecraft, the data were re-purposed to monitor global FACs using the Active Magnetosphere and Planetary Electrodynamics Response Experiment (AMPERE) [*Anderson et al.*, 2002, 2000; *Waters et al.*, 2001].

The AMPERE project provides estimates of the field aligned currents in the region poleward of 50° MLAT. This is achieved by expanding the cross-track component of the magnetic field measurements using spherical cap harmonics [*Waters et al.*, 2001]. The spherical harmonic fit of the magnetic field perturbations is used in conjunction with Ampere's law to derive the global FACs for each of the polar regions. An example of an AMPERE map in the Northern Hemisphere can be seen in Fig.3.7a. The map shows the distribution of current density with a resolution of 1 hr in MLT and 1° in MLAT. The R1 and R2 current systems are clearly visible as two rings of current close to 70° MLAT, flowing upwards (coloured red) at dusk and downwards (coloured blue) at dawn for R1 and with the opposite sense for R2.

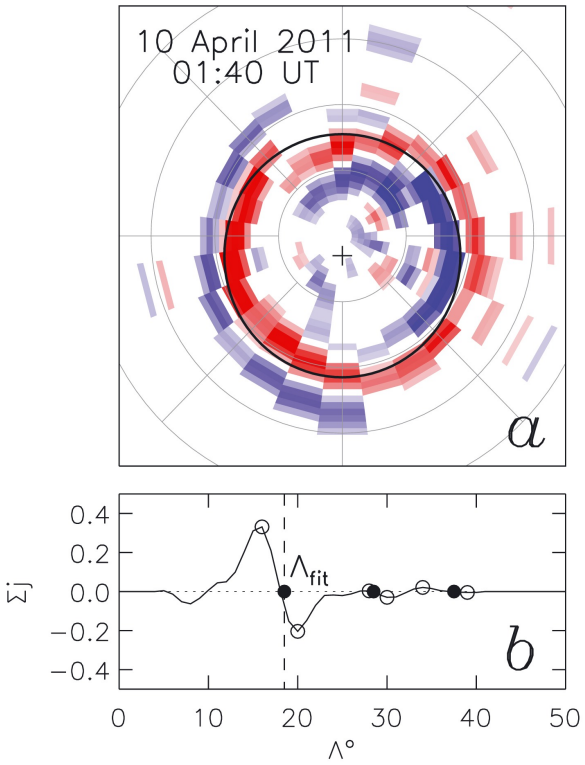

Figure 3.7: Panel A shows an example of an AMPERE current map from 10 April 2011 01:40 UT in the Northern Hemisphere. The red and blue colours show upward and downward currents respectively, with magnitudes between $\pm$ 1 μA m^2. The black circle is fitted to the boundary between the R1/R2 current systems and the black cross shows the center of the circle. Panel B shows the integrated currents (Σj) around the circumference of circles of radii Λ. The zero crossing, Λ_{fit}, marks the radius of best fit for the R1/R2 boundary. Figure from *Milan et al.* [2015].

3.2.1 Determination of the Open Closed Boundary Location

The AMPERE current maps can be used to determine the location of the OCB. The technique, proposed by *Milan et al.* [2015], begins by assuming that the R1/R2 currents are approximately circular with radius Λ, and are displaced from the geomagnetic pole by an offset, Λ_0, of a few degrees. Positive and negative values represent upwards and downwards currents respectively. Currents located on the dawn side ($0 \leq \text{MLT} < 12$) are multiplied by -1, so that all R1 currents become positive, and all R2 currents become negative. The integrated current around circles of increasing radii are then calculated for different circle center positions. The variation of the integrated current, Σj, with varying circle radius, Λ, is shown in Fig.3.7b. A bipolar signature is visible, maximising in the positive (negative) sense at the location of R1 (R2). The placement of the circle center that maximises the peak-to-peak magnitude of the bipolar signature is selected as the circle of best fit. The zero crossing in the center of the bipolar signature marks the boundary between the R1 and R2 current systems. It is this radius, Λ_{fit}, that approximately corresponds with the OCB location, which is marked in Fig.3.7a with a black circle.

Burrell et al. [2020] compared the AMPERE boundary to electron flux boundaries measured by the Special Sensor J instrument onboard the Defense Meteorological Satellite Program satellites. They noted an MLT-dependent relationship between the OCB measured by DMSP and the AMPERE boundary. At noon/midnight, the AMPERE boundary lies 4°/2° equatorward of the OCB. Therefore, subtracting 3° from the AMPERE boundary radius will give an approximate location of the OCB, which can be used as a proxy. All locations poleward of this latitude can then be considered to be inside the polar cap.

3.2.2 Limitations & Uncertainties

The quality of the fit depends on the strength of the R1/R2 currents. Very weak currents can result in the incorrect bipolar signature being selected as the R1/R2 location and the radius of the circle will therefore be incorrectly chosen. To reduce the number of bad fits, if the peak-to-peak magnitude of the bipolar signature is less than 0.15 μA m^2, the fit is considered unreliable and then not available for that time and hemisphere. However, in general the currents are stronger than this threshold, and 79% of the maps were successfully fitted [*Milan et al.*, 2015]. The current magnitudes measured in the Northern Hemisphere are systematically higher than those in the Southern Hemisphere, which will result in a greater number of successful fits in the Northern Hemisphere [*Coxon et al.*, 2016].

The spatial resolution of the AMPERE data is also limited. Smaller scale structures under 1° MLAT and 1 hr MLT cannot be resolved. As the main interest in the fitting procedure is the large scale R1/R2 systems, the available resolution is adequate for these purposes. The AMPERE maps are available at a cadence of 10 minutes, although 2 minute maps are also available and used within this thesis, which are produced by a sliding 10 min average. The OCB expands and contracts at an average speed of 0.1°/min with a maximum speed of 0.2°/min [*Sotirelis et al.*, 1998], which suggests that 2 min resolution is adequate, and the maximum uncertainty due to the OCB movement is $\pm$ 0.4°.

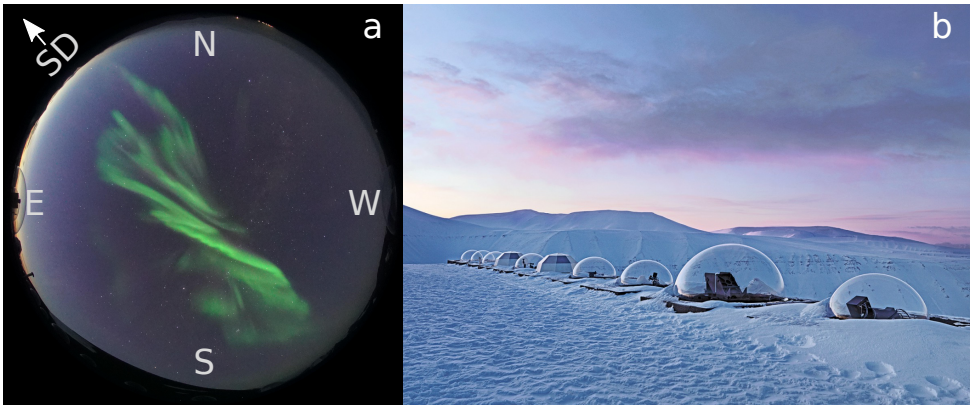

Figure 3.8: Panel A shows an image from the Sony a7s all sky camera. Cardinal directions are indicated, as is the orientation of the SuperDARN Longyearbyen radar (SD) in the North-East. Panel B shows instruments in heated glass domes on the roof of the Kjell Henriksen Observatory (image courtesy of *Vincent Fournier* [2010]).

3.3 Auroral Imaging

The auroral forms associated with flow channels (e.g. polar cap arcs and poleward moving auroral forms) can be imaged with ground-based or space-based optics. Local small-scale features can be captured by all sky cameras, while global imagers can provide context for auroral observations. All sky cameras and Defense Meteorological Satellite Program data were used for these purposes for the case studies in Paper I. In the next sections, information about the optical instrumentation relevant to this thesis is presented.

3.3.1 All Sky Cameras

All Sky Cameras (ASCs) are used to image large areas of the sky over a given location. In Paper I, the Sony a7s ASC imaged an auroral arc potentially associated with a flow channel. The ASC is a full format CMOS camera that uses a fish-eye lens to capture 180° RGB images of the sky with a 4 s exposure time and a time resolution between 10-30 seconds. The ASC has a spatial resolution of 12 megapixels and uses a Sigma 8mm f/3.5 EX DG Circular Fisheye lens. An example image from the ASC is shown in Fig.3.8a. North, south, east and west are indicated on the image at the top, bottom, left and right respectively. The auroral form is clear in the center of the image, aligned with the direction of the SuperDARN Longyearbyen FOV to the North-East. The camera is located at the Kjell Henriksen Observatory (KHO) at 78.148°N, 16.043°E, 520 m altitude, approximately 1 km from the SuperDARN Longyearbyen radar. Each instrument at KHO is positioned inside heated glass domes (Fig.3.8b) to allow full views of the sky in a temperature controlled environment.

All sky cameras require favourable weather conditions with a lack of cloud cover to image the aurora. This is often the main limiting factor for ground-based optical studies. The ASC used in Case 1 of Paper I is also not calibrated so it not possible

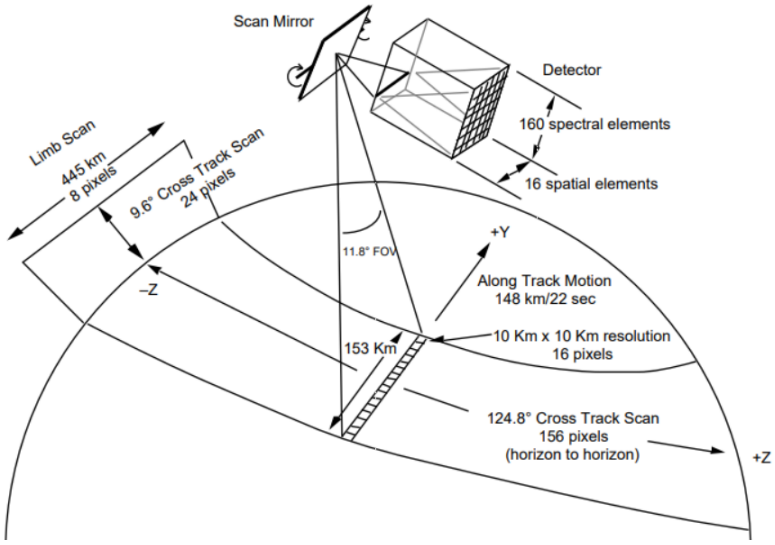

Figure 3.9: Schematic showing the operation of the SSUSI Scanning Imaging Spectrograph (SIS). Figure from *Paxton et al.* [1992].

to know the absolute intensity of the emissions. The emission altitude must also be assumed when mapping onto a geographical grid. The coverage of the all sky camera did not overlap with the other data sets in the case study. The all sky camera provided a local view and general orientation of auroral features above Longyearbyen at a high resolution in comparison to the other instruments, but was not used for anything more extensive.

3.3.2 Defense Meteorological Satellite Program

Space-based satellite images can provide a global context for auroral observations. The Defense Meteorological Satellite Program (DMSP) began in the mid-1960s and has launched many satellites since then, allowing in-situ measurements of the polar ionosphere. The DMSP spacecraft are in near-polar, Sun-synchronous orbits at an altitude of 840 km and a period of 101 min. Since 2003, DMSP spacecraft (DMSP F16–F19) have housed the Special Sensor Ultraviolet Spectrographic Imager (SSUSI) [*Paxton et al.*, 1992], which measures emissions in the far-ultraviolet spectrum from the Earth's upper atmosphere in five different wavelength bands.

The SSUSI sensor contains a line Scanning Imaging Spectrograph (SIS), and a Nadar Photometer System (NPS). The SIS, which is the component used in this thesis, is a Rowland circle spectrograph with a cross-track scanning mirror at the input to a telescope and a diffraction grating. Fig.3.9 shows a schematic of the SSUSI instrument during a scan. The spectrum from the diffraction grating is imaged on the detector in 16 along-track spatial pixels on the disk, and 8 pixels on the limb. During a scan, the mirror rotates from horizon to horizon (perpendicular to the spacecraft motion), taking $\sim$15 seconds to capture each thin slice of the image, and $\sim$20 minutes to build up an overview image of the auroral region [*Paxton et al.*, 1992, 2002].

Onboard processing bins the spectral images into the five wavelength bands: HI Lyman α (121.6 nm), OI (130.4 nm), OI (135.6 nm), N2 LBHS (140–160 nm), and N2 LBHL (160–180 nm). In this thesis, the LBHL measurements are used as this wavelength clearly resolves arcs within the polar cap (e.g. *Reidy et al.* [2017]) for comparison to flow channels within SuperDARN radar data.

Due to the long orbital period of the DMSP satellite (101 min), the temporal evolution of the flow channels cannot be measured. The polar cap arc that DMSP SSUSI imaged in case study 1 in Paper I had disappeared before the next satellite passed over its location, so only one measurement was available for the case study. The DMSP footprint did not intersect the arc, so particle data which would reveal more information about the arc was unavailable. The resolution of the auroral oval maps and the extent of the particle precipitation data are therefore the main relevant limitations for this thesis.

3.4 Solar Wind Measurements

OMNI is a multi-source data set of the near-Earth IMF conditions and plasma parameters, available at high-resolution (1 min) [*Papitashvili and Rich*, 2002]. This thesis utilises the IMF components: Bx, By, Bz (GSM). The OMNI dataset uses data from spacecraft in orbit around the first Lagrangian point (L1), where they monitor the solar wind conditions upstream of the Earth. Much of the data is supplied by the ACE [*Smith et al.*, 1998] and WIND [*Ogilvie and Desch*, 1997] spacecrafts. The data is pre-processed to shift the data from the point of measurement to the Earth's bow shock [*King and Papitashvili*, 2006]. Each spacecraft is assumed to lie along a phase front, which propagates through the heliosphere at the solar wind velocity, first passing both spacecraft and then the bow shock at a later time. Model boundary locations are assumed for the location of the bow shock [*Farris and Russell*, 1994]. The data from both spacecraft are averaged to give a combined 1 min resolution data set.

3.4.1 Limitations & Uncertainties

There are some uncertainties associated with the propagation method. The phase front can be titled at an angle with respect to the solar wind velocity, and the satellites orbit the Lagrangian point and can be a considerable distance (up to 100 R_e) from the Sun-Earth line [*Haaland et al.*, 2007; *Walsh et al.*, 2019]. Therefore, the local measurement at the spacecraft could be probing a region of plasma that never impacts the Earth's magnetosphere, or does so at a different time than the propagation predicts. Even if the plasma is on course to strike the Earth, it can be significantly altered in the dynamic and turbulent regions of the bow shock and magnetosheath, so the L1 measurements may not always accurately describe the conditions at the magnetopause. *Walsh et al.* [2019] compared measurement from the THEMIS spacecraft [*Auster et al.*, 2008] in the magnetosheath with corresponding measurements from monitors at L1 and found a standard deviation in the IMF clock angle of 38°. This value was larger when the L1 monitors were far from the Earth-Sun line.

Chapter 4

Summary of Results

This thesis investigates the characteristics of fast flow channels in the polar cap ionosphere and their solar wind driving conditions. The main part of the work has been presented in three separate scientific papers, Papers I-III, which are included in the Appendix. In this chapter, a description of the flow channel detection algorithm is presented and then a summary is provided for each of the papers.

4.1 Flow Channel Detection Algorithm

A flow channel detection algorithm was developed to identify fast flow channels with sharp gradients between the flow channel velocity and the background convection. Before using the algorithm, the SuperDARN data had to be appropriately filtered. The scans were required to contain all available beams, during times where the chosen radar was transmitting at a constant operational frequency. Data with common program ids (CPIDs) that were between 150–157 (common mode data) and 3500–3505 (two-f-sound data) were selected. Scans with less than 16 beams or with multiple frequencies were discarded.

In preparation for the detection algorithm, consecutive scans were averaged together to make an average grid. The averaging was done by making each scan into a 16 x 70 (beams x range gates) array of velocity values. Each element, or 'cell', in the array was then averaged with the same element in the other scans to create an average scan. The average was based on any available data, so the average velocity of each cell consists of 1–3 velocity values. The average scan was created to maximise the amount of available backscatter, so that the algorithm can more easily detect velocity structures. For common mode data, 3 scans of data were averaged together, which covers a period of 3 mins. In the two-f-sound mode, the radar switches between 2 different frequencies, and each frequency forms its own data set, with a 2 min resolution. For the average grid in this case, two scans on a constant frequency were averaged together for each available frequency, which covers a period of 4 minutes.

For ease of description, from this point on a 'grid' now refers to the averaged grid of beams and range gates, where each 'cell' contains an average velocity at that specific beam and range gate. The scan now goes through a series of tests:

1. The velocity test
2. The structure test

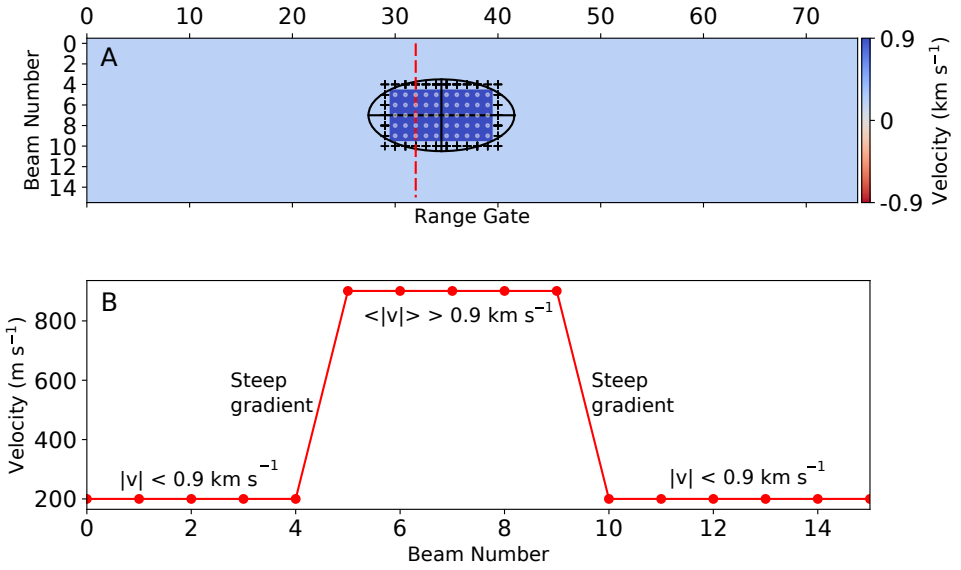

Figure 4.1: Plot from Paper I, showing the analysis of a simulated flow channel. Panel A shows a grid of velocities, with a visible flow enhancement (>900 m/s) in a slower background flow (200 m/s) directed towards the radar (coloured blue). The grey dots indicate identified cells and the black crosses indicate identified edges. The dashed red line shows a slice through the velocities on all beams at a constant range. Panel B shows the resulting velocity profile along the slice shown in Panel A. The profile is annotated to point out notable features and facilitate discussion in the text.

3. The gradient test

4. The background test

For the velocity test, the grid was searched for values above a threshold of 900 m/s. If none were found, then the grid cannot contain a fast flow channel, so it was discarded and the next one was then tested.

If the velocity test was passed, then it was important to check if the fast flows were simply isolated cells of noise, or a structured, high velocity flow channel. The structure test involves checking the neighbouring cells around a cell that had passed the velocity test. If all the neighbouring cells contained scatter, and all the velocities were in the same direction (towards or away from the radar), and the average velocity of the neighbouring cells was over 900 m/s, then the structure test was considered successful. Checking the average value of the neighbouring cells rather than imposing a strict threshold allows for some variation in the flow channel. As the structure test requires data on either side of the cell, the largest and smallest beams and ranges were not considered (i.e at the edge of the radar field-of-view), even if fast flows exist there.

If the structure test was passed, then the next step was to test the gradient between the flow channel and the background convection. As the radar measures the line-of-sight component of the velocity, a constant flow at an angle to the look direction can manifest as low speeds that gradually change to high speeds. These instances should be eliminated from the results as they are not flow channels. Fig.4.1 shows an illustration of the gradient test for a simulated flow channel. A slice (red dashed line in Fig.4.1a) was taken through the cell that has passed all the previous tests. The gradient in the velocity was calculated by taking the difference in the velocity ($v_1 - v_2$) in a sliding window across the entire slice. The velocity over the slice for each beam is shown in Fig.4.1b. The velocity profile shows that on either side of the channel, sharp gradients exist with opposite signs.

The gradient test involves searching for this pair of sharp, oppositely directed gradients within the slice. The magnitude of the gradient on each side must be greater than 400 m/s/cell. These points mark the 'edges' of the flow channel, which are marked with crosses in Fig.4.1b. Outside of the edges, the velocity is low in the background flow and should not exceed 900 m/s. Inside the edges, the velocity is high and on average $\geq$ 900 m/s. There should also be no missing data in the cells within the channel, between the two identified edges, and the edges should not be at the smallest or largest beams and ranges, to identify flow channels that are centrally located in the field-of-view. Slicing only in one direction could bias the results to certain orientations of flow channel. To avoid this bias, slices were taken in a circle around the identified cell in 30° increments. To ensure that the flow channel really is a boundary between fast and slower flows and not a misidentification, a minimum of 6 edges must be present for the flow channel to pass the gradient test. Lastly, the velocity inside the flow channel should be in the same direction as the flow outside of the edges. This condition eliminates any reverse flow events (Section 2.9.3) and allows us to detect only flow channels that are enhanced in the direction of the background convection.

The final test was to check if there was an identifiable background convection, in which the flow channel was embedded. The velocities immediately outside of the edges for each slice were then examined. If >80% of these points were present, then an

identifiable background flow was considered to exist, that is substantially slower than the flow channel. If the grid satisfies all of the aforementioned criteria, then the velocity structure inside is flagged as a fast flow channel.

After the flow channel was detected, an oval was fitted to the distribution of positively identified cells (grey dots), as shown in Fig.4.1. This was achieved through principle component analysis of the distribution of identified cells, and the calculated eigenvectors (semimajor and semiminor axis of the ellipse) were scaled so that 96% of the identified cells were required to be within the ellipse. The length of the semiminor axis can then be used as an estimate for the width of the flow channel and the semimajor axis can be used to estimate the orientation of the flow channel.

To ensure our statistics were not biased by periods where flow channels occurred for long periods of time, it was necessary to group the detections into events. A gap of $\geq$4 min was chosen to signify a new event. This threshold was chosen because it allowed one (two-f-sound) or two (common mode) scans without detections during events, which can occur if the flow channel velocity drops slightly below the velocity threshold of 900 m/s, before rising again. The event separation was also kept purposefully short at $\geq$4 min as some transient features on the dayside have a recurrence rate of 7-8 min (e.g. PIFs), and should be resolved as separate events.

4.2 Paper 1: A Study of Automatically Detected Flow Channels in the Polar Cap Ionosphere

In Paper I, a newly developed algorithm to identify structured fast flow within Super Dual Auroral Radar Network (SuperDARN) data is presented. This algorithm targets fast flows (>900 m/s) embedded within the slower moving, large scale background convection. The algorithm was applied to 1 year of data from the Longyearbyen radar (78.2°N, 16.0°E geographical coordinates), which is ideally situated for observing flows within the polar cap. Over 500 events were identified, the majority of which were in the dayside polar cap, and 2 were selected for in depth analysis.

In Case 1 (2 October 2017), satellite data, ground based optics, and the Longyearbyen SuperDARN radar were used to observe a flow channel which was located between the main auroral oval and a polar cap arc. The flow channel occurred on the dawn flank, was 418 km in width, and persisted for 13 min. The location of the flow channel and the preceding solar wind conditions suggest that this is within the directly driven FC 2 category of flow channels on old open flux within the SF framework.

In Case 2 (7 November 2017), a flow channel was intermittently excited in the cusp region for approximately an hour. Once again, satellite data and ground based optics and the Longyearbyen SuperDARN radar were used to observe the flow channel. This flow channel represents FC 1 in the SF framework, occurring on newly opened field lines, spontaneously driven, forming under strong solar wind driving.

Both flow channel events accounted for large values of the cross polar cap potential (60% and 40% at the peaks), suggesting that polar cap flow channels play an important role in magnetic flux transfer over the polar cap.

4.3 Paper 2: A Statistical Study of Polar Cap Flow Channels and their IMF By dependence

In Paper II, a statistical study is conducted on flow channel events identified by the detection algorithm from Paper I, during the interval October 2016 - November 2018. The algorithm detected 1048 flow channel events, the majority of which occurred on the dayside (998 events).

General characteristics of the flow channels were determined. The flow channel duration was between 3-15 mins, with most events detected for the minimum time of 3 min. The flow channel width and peak velocity were typically between 200-300 km and 1.1–1.3 km/s respectively. There was a notable absence of fast (>1500 m/s) flows.

This is the first statistical study on flow channels using the Longyearbyen SuperDARN Radar, which is statistically located in the polar cap with a zonally oriented field-of-view. This orientation is ideal for investigating the azimuthally directed flows due to magnetic tension resulting from an IMF By component. The dayside events were used to investigate the influence of IMF By on the flow channel location, which shifted duskwards for a +IMF By with mostly westward flows and dawnwards for -IMF By with mostly eastward flows.

4.4 Paper 3: A Statistical Study of Polar Cap Flow Channels observed in Both Hemispheres using SuperDARN Radars

In Paper III, the fast flow channel detection algorithm is applied to the polar SuperDARN radars in the Northern and Southern Hemisphere over a 10 year period (2008-2018). The occurrence distributions of the flow channel location in MLT/MLAT reveal that flow channels are detected at all MLTs, but the majority of the flow channels are observed on the dayside in both hemispheres. The occurrence distribution shows a statistical picture of the flow channels at different stages in their evolution. This is the first time that flow channels on old-open field lines have been studied statistically.

The solar wind driving conditions of the flow channels were also studied. The flow channels showed a preference for a By-dominated IMF, with clock angle distributions peaking close to 90° and 270°. Under +IMF By (-IMF By) conditions in the Northern (Southern) hemisphere, flow channels were detected deep into the polar cap on the dawn flank on old open field lines. A Monte Carlo simulation was used to derive a probability distribution for the IMF. This simulation was then used to calculate the standard deviation of the typical IMF components. The median of the probability distribution of the standard deviation was then used to definite the stability criterion. Values greater than the median were considered to be unstable. Using this criterion, the flow channel events were found to occur mainly under unstable IMF. Flow channels generally do not require large magnitudes of IMF By or Bz to form, peaking in occurrence for magnitudes of $\pm$3.5 nT for IMF By and -0.5 nT for IMF Bz.

Chapter 5

Discussion

5.1 A New Approach for Detecting Flow Channels

The flow channel detection algorithm presented in Paper I and used throughout Paper II and Paper III makes it possible for the first time to automatically detect flow channels over all MLTs, within a large area of both the Northern and Southern polar caps. Previous works have included detections via satellite passes (e.g *Sandholt and Farrugia* [2009]), where the flow channel is sampled once per orbit (101 min), but more frequently for time periods where there are multiple DMSP satellites in orbit. The algorithm uses 1–2 minute resolution SuperDARN data, which makes it possible to monitor the temporal evolution of the flow channel, from formation to decay and any periodicity or other temporal effects during its lifetime. Although flow channels have been detected in SuperDARN data many times before, these works have either focused on case studies [*Marchaudon et al.*, 2004; *Pinnock et al.*, 1993], used only a single beam of the radar and have been unable to determine 2D spatial structure [*Provan et al.*, 1999], used global SuperDARN convection maps for a large scale, low-resolution view of the flow channel [*Andalsvik et al.*, 2011], or applied algorithms that work well only in certain orientations of radar field-of-views over a small range of magnetic local times [*Gabrielse et al.*, 2018].

With the algorithm, it is possible to follow the two dimensional temporal and spatial evolution of flow channels at a 1–2 minute resolution. This allows mesoscale flow structures to be mapped in high resolution (45 km range resolution) in greater spatial detail than single-beam studies. The solar wind driving conditions are not constrained in any way, as done in previous studies with case studies during interplanetary coronal mass ejections where the solar wind varies slowly over long periods of time [*Andalsvik et al.*, 2011; *Sandholt and Farrugia*, 2009; *Sandholt et al.*, 2010]. This allows flow channels due to variable IMF conditions and during low magnitude fields to be detected, and it was possible to evaluate under which conditions flow channels are observed most frequently.

5.2 Limitations of the Algorithm

The limitations of the SuperDARN data set have been discussed in Section 3.1.4, so the following discussion will be focused specifically on the limitations of the algorithm, al-

though they share similar themes. For example, the flow channel detection algorithm is limited by the spatial and temporal resolution of the SuperDARN data. As the flow channels are moving at high velocities and 3 (2) scans are averaged together for common (two-f-sound) mode, the channel may appear elongated and it could become difficult to distinguish between small features that move quickly and longer, static features. It is also not possible to resolve smaller structures than the range gate resolution (45 km), although in Paper I, the spectral width measurements indicated that structuring likely occurred on smaller scales.

Another consideration is the placement of the flow channel within the radar field-of-view. The algorithm cannot detect flow channels if they are not contained centrally within the field-of-view. The flow channels are known to be longitudinally elongated (>900 km), so the algorithm may only sample a section of the flow channel, which can extend out of the field-of-view depending on its location and orientation relative to the radar.

In addition, the line-of-sight velocity data must be approached with caution when using the algorithm and interpreting the results. The requirement of sharp gradients on each side of the flow channel means that the variations due to gradual changes in direction will not be incorrectly identified by the algorithm as flow channels. However, flows perpendicular to the beam direction will not be detected at all. The algorithm threshold is set high at 900 m/s and the most commonly detected flow channel speed was 1200 m/s. If the flow channel is orientated >40° from the line of sight direction, a 1200 m/s flow is reduced to under 900 m/s and will not be detected by the algorithm. Paper II was concerned with the statistics of flow channels within the Longyearbyen radar, which is zonally directed. Aware of the line-of-sight velocity limitation, only flow channels occurring under By-dominated conditions were further investigated. This mitigated the limitation, as these flow channels are expected to move in the zonal direction, approximately in the beam direction. In previous studies, overlapping SuperDARN radar fields-of-view have allowed two-dimensional measurements of the velocity to be determined. Paper I and II were concerned with the use of only one radar, but this approach was considered during the multi-radar study in Paper III. However, out of ∼33,000 flow channels detected, only ∼500 were detected by 2 radars within the same hemisphere at exactly the same time, and less occur in an exactly overlapping region. This is therefore not a viable solution for a large statistical study on the scale of what was achieved with Paper III, but would make an excellent subset of fast flow channels for case studies or a smaller statistical study.

5.3 Typical Characteristics of Flow Channels in the Polar Cap

5.3.1 Duration

The flow channels detected by the algorithm were typically variable pulses, 1 scan in duration (2-3 minutes). There were less events as the flow channel duration increased, but a number of flow channels were still noted up to 20 minutes in duration. This was seen in the statistics for the Longyearbyen radar in Paper II and also in the larger statistical study with multiple radars in Paper III. This value is likely an underestimation of the flow channel duration. This is shown in Paper I, as the case study on old open

field lines revealed that although the algorithm detected the flow channel for 3 scans from 1:10-1:12, through manual inspection, the flow channel was seen to actually began forming at 1:07, peak at 1:12, and decay by 1:20, which is a total duration of 13 min. The algorithm was therefore most effective at detecting the flow channel at its peak. A more realistic duration could be estimated by iterating through the scans before and after each peak detection and either decreasing the velocity and gradient threshold and rerunning the algorithm, or examining the velocity distribution within each scans and comparing the time series in search of the formation and decay of the flow channel.

If the one-scan detections are removed from the sample, the median duration of the flow channels is 6 minutes. Although the flow channels are mostly detected on the dayside, this duration is comparable to nightside results from *Gabrielse et al.* [2018]. Their algorithm detects flow channels on the nightside within SuperDARN data which show a similar duration distribution, where the majority of their events were detected for only one scan, but if the single scans were neglected then the flow channels in the polar cap had a median duration of 4 minutes. Dayside flow channels have previously been estimated to range from 5-25 minutes [*Lockwood et al.*, 1990] in duration, which is also comparable with the range of durations in the statistics of Paper II and Paper III.

5.3.2 Peak Velocity

The peak velocity of the flow channels was typically between 1.1–1.3 km/s. The statistics from Paper II and Paper III both agree on these values, suggesting that the characteristic peak velocity is not biased by each radar, operational frequency, or field-of-view orientation. These velocities are much higher than typical background convection speeds, which are several hundred m/s [*MacDougall and Jayachandran*, 2001]. The observed flow channels are the extreme cases, creating strong velocity shears, associated field-aligned current systems, and strong coupling within the solar wind-magnetosphere-ionosphere system.

The velocity of flow channels in other studies can be much lower than our threshold, such as those associated with airglow patches [*Zou et al.*, 2015b], which are approximately 600 m/s and only 200 m/s larger than the background convection velocity. Also, the peak occurrence of nightside flow channels studied by *Gabrielse et al.* [2018] was at $\sim$250 m/s and the distribution tailed off towards 600 m/s. If the velocity and gradient threshold of the algorithm were relaxed, then naturally many more flow channels would be detected. This thesis is strictly concerned with the properties of the very fastest population of flow channels and their relation to solar wind driving conditions. As the velocity and gradient thresholds are high, this allows only the detection of very fast flow channels which are significantly higher than the background flows. This thesis is the first time that these high flows have been investigated in such a comprehensive statistical study.

The peak velocities that were measured with SuperDARN data are likely underestimates of the true velocity of the flow channel. When compared with DMSP flow velocities and Resolute Bay incoherent scatter radar measurements, the SuperDARN velocities are systematically a factor of $\sim$1.2 and $\sim$1.3 lower [*Gillies et al.*, 2009; *Koustov et al.*, 2016]. This underestimation was thought to be due to the assumption that the radar waves propagate in a vacuum, which therefore neglected the index of refraction in the scattering region [*Ponomarenko et al.*, 2009]. Efforts have been made to correct

for the underestimation [*Gillies et al.*, 2009; *Ponomarenko et al.*, 2009], however *Koustov et al.* [2016] has shown that this can in turn lead to an overestimation, at least in the case of the Rankin Inlet radar. In this thesis, it was decided to not attempt to correct the velocities and instead to highlight that caution should be taken when directly comparing SuperDARN flow channel velocities to those detected in DMSP observations [*Andalsvik et al.*, 2011; *Sandholt and Farrugia*, 2009] and EISCAT measurements [*Oksavik et al.*, 2010; *Rinne et al.*, 2010].

5.3.3 Width

The flow channels from the Longyearbyen statistics (Paper II) ranged between 72 to 660 km in width but more typically had widths between 200-300 km. Paper 3 was in agreement with the typical widths, as the peak of the flow channel width occurrence was between 200-250 km and the mean value of the width was ∼300 km. This could be the characteristic width of mesoscale flow channels in the polar cap. These values are of a similar order to previous studies, such as *Provan et al.* [1998] (250 km), *Wang et al.* [2016] (300 km), *Zou et al.* [2015b] (200-300 km) and *Gabrielse et al.* [2018] (∼180 km median values within the polar cap).

The width values from Paper II are favoured towards measurements of the latitudinal width of the flow channel, as the Longyearbyen Radar orientation is most favourable to detect longitudinally oriented channels in the dayside cusp region. In other radar orientations, such as the polar directed Rankin Inlet, more of a latitudinal width component may be measured, especially on the nightside where FC 3 (associated with PBIs) is expected to be equatorward directed flows. The value of the width in Paper III therefore cannot be considered to be a latitudinal width in all cases.

In Paper II, the data suggests an absence of fast, wide flow channels, which could imply that high velocity flows in the polar cap can concentrate into localised, narrower channels. Although, it was noted that the population of flow channels with very high speeds (>1500 m/s) and large widths (>500 km) is small, so further study with more data was required to confirm this relationship. The statistics in Paper III still do not provide a clear trend to support the idea and the results remain inconclusive.

5.4 The Solar Wind Driving of Fast Flow Channels

The majority of the detected flow channels in Paper I, Paper II, and Paper III were driven by By-dominated conditions. The work in Paper II confirms earlier work by *Provan et al.* [1999], as the flow channel location distribution is shifted postnoon (prenoon) for +IMF By (-IMF By) conditions with an westwards (eastwards) flow in the dayside ionosphere. The *Provan et al.* [1999] study used the Hankasalmi radar in Finland, which is orientated polewards. The Longyearbyen radar used in Paper II is more zonally orientated and therefore has a much more appropriate field-of-view and latitude for observing the IMF By influence on dayside transients near the cusp region. Paper III data showed the same shifting of the flow channel location due to the IMF By as in Paper II.

All three Papers also provide evidence that the IMF components are not required to be high magnitude to drive flow channels in the polar cap. Case 1 in Paper I shows a

flow channel on the dusk flank (79 MLAT, 7 MLT) that is driven by small magnitude magnetic fields (Bz -0.5–2.5, By -1–2.5 nT). Although, Case 2 in Paper I shows that flow channels driven by higher IMF magnitudes (Bz -5 to -7 nT, By 10 nT) can last for long periods of time (up to an hour) if the magnitudes remain high. The statistics of Paper III show that it is the low magnitude, short duration, unstable, IMF By-dominated fast flow channels that are observed the most, with mean magnitudes of By=4 nT, Bz=2 nT, Bx=3 nT. This is an interesting finding as many previous studies on fast flow channels have been constrained to times of strong solar wind driving with high magnitude magnetic fields, such as during Interplanetary Coronal Mass Ejections (ICMEs) [*Andalsvik et al.*, 2011; *Sandholt and Farrugia*, 2009; *Sandholt et al.*, 2010]. Findings from all three Papers suggest that these rare cases of extreme IMF are not required to drive fast flow channels and the ionosphere-magnetosphere system is driven more frequently by average conditions, and are therefore a more common phenomena.

It is likely that flow channels are also present on the dusk flank, but that ionospheric conditions are not favourable for them to be detected within SuperDARN data. Under +IMF By (-IMF By) conditions in the NH (SH), higher density plasma is drawn from the postnoon sector into the convection pattern towards the dawn flank. This higher density plasma can result in more irregularities and can therefore create more favourable conditions for the radars to detect flow channels than on the dusk flank, where the lower density plasma is circulating [*Jin et al.*, 2015; *Oksavik et al.*, 2010].

It is also noted that findings in Paper II (where mostly dayside flow channels are observed) suggest a seasonal preference of the fast flow channels. The occurrence distribution peaks close to the spring and autumn equinoxes. This may be due to the Russell-McPherron effect, where the southward component becomes statistically more geoeffective at the equinoxes and there is a stronger coupling between the solar wind-magnetosphere-ionosphere system. Overall, this suggests that dayside reconnection with a strong IMF By component is the dominant mechanism in accelerating the flow channels in the dayside region to the high velocities detected with the algorithm.

5.5 The Role of Flow Channels in Flux Transfer over the Polar Cap

In Paper I, the flow channels from Case 1 on the dawn flank and Case 2 in the cusp region were found to account for 60% and 46% of the cross polar cap potential (CPCP) at their peak values. This suggests that flow channels can account for a substantial amount of the polar cap potential and that they are important in the redistribution of flux over the polar cap, occurring both at the ionospheric footprint due to dayside reconnection and deeper into the polar cap on the flank of a polar cap arc. However, these values could be an overestimation, as the CPCP is estimated from the SuperDARN convection maps, where data coverage is not present across all points in the polar cap. Other estimates in literature find that polar cap flow channels account for 35% [*Andalsvik et al.*, 2011] and 25% [*Sandholt et al.*, 2010] of the CPCP. All of these estimates suggest that polar cap flow channels can account for a substantial amount of the CPCP, and that it is important to have radar coverage in the polar cap in order to obtain realistic values of the CPCP, as without coverage in these regions the CPCP would likely be severely underestimated.

Fig.5.1a and b show a conceptual overview of the different flow channel stages from

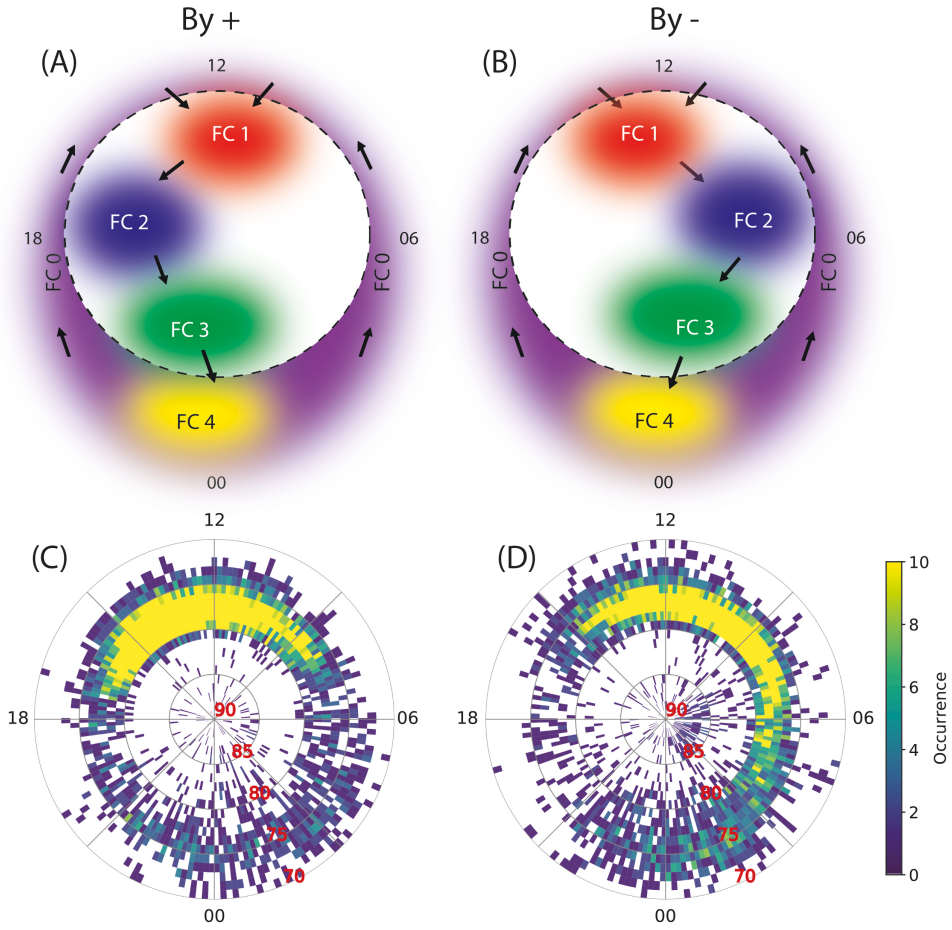

Figure 5.1: Panels A and B show a conceptual MLAT/MLT overview of the different stages of flow channels in the Southern Hemisphere for +IMF By and -IMF By respectively. Approximate regions of the flow channels at different stages of evolution across the polar cap are indicated by the different shaded regions for FC 0 (purple), FC 1 (red), FC 2 (blue), FC 3 (green), and FC 4 (yellow). Black arrows mark the direction of plasma flow at the indicated locations and the OCB is indicated by a dashed circle. Panels C and D show the flow channel MLAT/MLT occurrence distribution (including flow channels on closed field lines) in the Southern Hemisphere for +IMF By and -IMF By respectively.

the SF framework (see Section 2.14) for positive and negative IMF By in the Southern Hemisphere. Black arrows mark the direction of plasma flow at the indicated locations. Fig.5.1c and d show the occurrence distribution of flow channel location in MLT/MLAT for positive and negative IMF By in the Southern Hemisphere (from the supplementary material of Paper III). These distributions include flow channels detected on both open and closed field lines. The occurrence distributions show that FCs were detected over all MLTs. This indicates that flow channels play an important role in the redistribution of magnetic flux across the entire polar cap.

The dayside driven channels (FC 1/ FC 2, up to 20-25 minutes after dayside reconnection), are the most prominent in the statistics, and are present in high occurrences (in agreement with Paper II). This could be due to the cusp region acting as a a hot spot for ionospheric irregularities, as seen in both GPS phase scintillation and HF radar backscatter over longer duration and larger areas than observed on the nightside [*Prikryl et al.*, 2011]. The occurrence distributions also show the shifting of the FC 1 and FC 2 location in MLT under different senses of IMF By that is present in the conceptual overview. For +IMF By (-IMF By) the area of high occurrence (yellow region) in Fig.5.1c and d is shifted duskward (dawnwards), in agreement with the direction of the magnetic tension forces from dayside reconnection in response to a By-dominant IMF. The population of FCs on the flanks likely contains FC 2 on old open field lines, which are no longer directly driven by active dayside reconnection but are instead driven by momentum transfer from field lines connected to the high-latitude boundary layer, tailwards of the cusp [*Stern*, 1984].

The nightside driven flow channels (FC 3 and FC 4) and flow channels in the return flow regions on closed field lines (FC 0) are present in the occurrence distribution, but are much less abundant than the dayside driven channels. This could be due to the selection of radars, which is discussed in more detail in the following paragraph. It is important to note that the different regions of flow channels indicated in Fig.5.1a and b are not fixed in MLT/MLAT and the position of the flow channels depends on the prevailing solar wind and geomagnetic driving conditions. The displayed regions are rather a conceptual approximation of the average FC locations over all IMF conditions. The SH distribution was chosen for discussion as there were a higher number of flow channels observed than in the NH. The IMF By dependency is also visible in the NH, but with an opposite sense of IMF By to that in the SH.

The aim of the thesis was to study the characteristics and solar wind driving of polar cap flow channels, so only the radars with fields-of-view at high latitudes were chosen. FC 3 and FC 4 are linked to substorm activity and auroral streamers. Statistical studies [*Wang et al.*, 2005] show that the most poleward latitudes of substorm onsets occur at 73° magnetic latitude. It is likely that the constraint of using the highest latitude SuperDARN radars leads to low occurrences of nightside driven flow channels, as their field-of-views extend to a minimum latitude of 60° in the SH and 65° in the NH. It is also difficult to observe scatter at the far ranges as this requires multiple-hop propagation. Propagation conditions have to be favourable to support these modes, and during auroral substorms the ionosphere is very disturbed and can lead to decreases in backscatter at the radars [*Wild and Grocott*, 2008]. The radars which were able to view the flow channels associated with auroral activity in their close ranges (e.g. Rankin Inlet) likely observe the flow channels within E-region scatter, which is limited to the ion acoustic speed and cannot reach the high magnitudes required by the detection algo-

rithm [*Koustov et al.*, 2005; *Zou et al.*, 2014]. The nightside flow channels are therefore less abundant in the statistics, and the algorithm (when applied to the polar radars) is more suitable for detecting dayside flow channels. Paper III is the first time that FC 2 on the dawn flank has been successfully statistically examined.

The majority of flow channels in Paper II and Paper III are polar cap flow channels. In Paper I, satellite imaging and global convection maps were used to determine that the flow channels were inside the polar cap. In Paper II, it was argued that the Longyearbyen radar is located in the polar cap in a statistical sense, as the radar field-of-view measures a latitudinal range of 76–82° (magnetic coordinates) while the most poleward section of the OCB is statistically located at 75° [*Yeoman et al.*, 2002]. In Paper III, the AMPERE data were used to determine the OCB location and the flow channel location was then evaluated to confirm whether the flow channel was inside or outside of the polar cap. However, this method does have some associated uncertainties. Firstly, the auroral oval is approximated as a circle. This could lead to an underestimation of the radius of the OCB on the dayside and an overestimation on the nightside. The R1/R2 current system can also be unstructured due to disturbances or faint current system, which can lead to an unrealistic fit. Although, to combat the bad fits due to weak currents, all fits with a peak-to-peak current density magnitude less than 0.15 μA/m are discarded [*Milan et al.*, 2015].

Of the flow channels with AMPERE data in the period 2010–2016, 84% were classified as inside the polar cap and 16% were classified as outside the polar cap. Closer study of the flow channels that are classified as outside the polar cap shows that 81% of these were detected using the South Pole Station (SPS) and Zhongshan (ZHO) radars. Most of these flow channels occurred at 13–15 MLT, 78–76 MLAT (with the distributions tailing off at 82° on the poleward size and 70° on the equatorward side). These flow channels are statistically just below the dayside OCB and occur in the postnoon region, so could realistically be flow channels on closed field lines in the return flow region (FC 0) [*Moen et al.*, 1995]. Although these flow channels are an interesting subset, they are not the focus of the thesis and were discarded from the data set in Paper III. After the removal of these events, >95% of the flow channels were within the polar cap and overall the statistics presented within Paper III can be considered to be representative of polar cap flow channels.

Chapter 6

Conclusions & Future Work

6.1 Conclusions

This thesis has investigated the characteristics and interplanetary magnetic field driving conditions of ionospheric flow channels in the polar cap. It includes the first large scale, inter-hemispheric statistical study into ionospheric fast flow channels with velocities >900 m/s in the polar cap. The SuperDARN network of coherent scatter radars have been used together with a newly developed detection algorithm. Both ground-based and satellite auroral imagery have been used in multi-instrument case studies. Through both case studies and statistical studies, the width, peak velocity, duration, location and interplanetary magnetic field drivers of the fast flow channels have been investigated. The key findings of the thesis have been discussed in detail in Chapter 5 and are summarised here:

1. Typical characteristics of fast flow channels

The peak velocity of the fast flow channels was typically between 1.1–1.3 km/s. The fast flow channels were typically 200–300 km in width. Fast flow channels were most frequently observed for 2-3 minutes in duration, corresponding to one radar scan. The majority of the FCs were observed for up to 20 minutes in duration, but a small number of events exceeded 1 hour.

2. Spatial distribution of fast flow channels

This thesis presents the first statistical occurrence distributions of flow channels at all MLTs in the northern and southern polar caps. The majority of the fast flow channels were observed on the dayside in both hemispheres, and the lowest occurrences were on the nightside and the dusk flank. This thesis also presents the first statistical distribution of flow channels on old open field lines. Fast polar cap flow channels were observed deep within the polar cap and on the edge of polar cap arcs.

3. Importance of fast flow channels in the transport of magnetic flux across the polar cap

Fast polar cap flow channels were observed at all stages of their evolution across the polar cap. Fast flow channels can account for significant fractions of the cross polar

cap potential (40-60%) and are therefore important for the redistribution of magnetic flux across the polar cap.

4. Interplanetary magnetic field and fast flow channels

The fast flow channels showed a preference for IMF By-dominant solar wind driving conditions, with clock angle distributions peaking close to 90° and 270°. The fast flow channels were observed mainly under unstable IMF. Under IMF By+ (IMF By-) conditions in the Northern Hemisphere (Southern Hemisphere), flow channels are detected deep into the polar cap on the dawn flank on old open field lines. Flow channels generally do not require large magnitudes of IMF By or IMF Bz to form, peaking in occurrence for magnitudes of $\pm$3.5 nT for IMF By and -0.5 nT for IMF Bz.

6.2 Future Work

The detection algorithm and resultant database of flow channels generated in this thesis has much more to offer than could be achieved in a single PhD. This thesis provides the groundwork for many new and exciting research opportunities. Some suggested projects for future work are listed below.

The Thermospheric Response to Ionospheric Flow Channels

How the neutral thermosphere reacts to sudden changes in plasma velocity, such as those that occur during ionospheric flow channels, is not yet fully understood or substantially researched [*Deng et al.*, 2019]. Such localised strong flows are likely to be significant mesoscale momentum and energy sources to the thermosphere through the ion-neutral coupling process. The database of fast flow channels can be used in conjunction with incoherent scatter radar data (e.g EISCAT Svalbard Radar or Poker Flat Incoherent Scatter Radar) and neutral wind measurements from Scanning Doppler Imagers (SDIs) to answer the following open questions:

- How does the thermospheric wind and temperature change in response to energy deposited by ionospheric flow channels?
- How much energy is deposited in the thermosphere due to particle precipitation associated with flow channel structures (e.g. poleward moving auroral forms and auroral arcs)?
- How much energy/mass is transported up from the thermosphere to the magnetosphere due to ionospheric heating driven by flow channels (e.g. via ion outflow)?
- What is the relationship between the size/velocity/duration of the flow channels and the thermospheric response?

The Evolution of Ionospheric Flow Channels

The flow channel detection algorithm is best suited to detecting the flow channels at their peak. With the peak now identified, the formation and decay stages of the flow

channels can be obtained through manual inspection or computationally by comparing the scans before and after the peak to determine a total duration for each flow channel. The follow open questions can then be addressed:

- What is the typical duration of ionospheric flow channels, from formation to decay?
- Do the formation, peak, and decay of the flow channel occur in discrete stages? If so how long is each stage of the evolution?
- How does the flow channel evolution change with different solar wind driving conditions?
- Do flow channels have the same duration across all MLTs?

These questions can be answered in a statistical sense but there is also value in case studies for this project. There were events in the flow channel database that were identified by two radars in an overlapping backscatter region. Case studies of these events could allow velocity vectors to be determined and the flow channel motion and evolution could be determined in fuller detail.

Interhemispheric Behaviour of Ionospheric Flow Channels

As we include radar data from both hemispheres, a subset of our events include flow channels that are observed simultaneously in both hemispheres. These events can be used to explore the following:

- Do the flow channels show the expected asymmetry due to dayside reconnection under By-dominated solar wind driving?
- Do the flow channels have similar characteristics, e.g width, velocity and duration?
- Can the flow channel width on newly-opened field lines give information on the length of the reconnection region in the magnetosphere?
- Do the nightside flow channels occur simultaneously in both hemispheres and what does this suggest about the dynamics of the magnetotail?

Auroral Forms Associated with Ionospheric Flow Channels

The flow channel database could be compared to ground based (e.g meridian scanning photometers, all sky cameras) and satellite (e.g. DMSP, IMAGE) optics to investigate the relationship between flow channels and auroral features. The following questions could be addressed:

- What type of auroral forms are associated with the flow channels?
- Are these auroral forms confined to a certain range of MLT/MLATs?
- Are flow channels present while the auroral forms develop and evolve on their journey across the polar cap?

- What role do flow channels play in the formation of the auroral features (e.g. airglow patches)?
- Under what IMF driving conditions are the auroral features observed?
- Do the auroral features appear and develop simultaneously in both hemispheres?

Ionospheric Flow Channels on Closed Field Lines

This thesis concentrated on polar cap flow channels, but there are also flow channels occurring on closed field lines in the ionospheric return flow regions [*Moen et al.*, 1995], which are classified as FC 0 in the SF framework. Applying the algorithm to mid latitude flows on closed field lines will allow the detection of flow channels within the auroral zones. The following questions can be addressed:

- What are the characteristics (e.g. velocity, duration, width) of flow channels on closed field lines?
- Are the characteristics similar to polar cap flow channels?
- Where/when are flow channels on closed field lines most frequently observed?
- How significant are flow channels on closed field lines in the redistribution of magnetic flux?

Lower Velocity Flow Channels in the Polar Cap

The velocity and gradient thresholds have been fixed at high values during this thesis to investigate the extreme population of high velocity flow channels. It would also be interesting to decrease the thresholds and examine the statistics of the lower velocity flow channels. Some open questions include:

- Are the lower velocity flow channels more common that the higher velocity flow channels?
- How much of the cross polar cap potential do the lower velocity flow channels account for?
- Are the lower velocity flow channels associated with different magnetospheric/ionospheric phenomena than the higher velocity flow channels?
- What is the velocity distribution of flow channels in the polar cap?
- Does lowering the threshold allow for the tracking of features, such as airglow patches, across the polar cap?

This thesis, in addition to all of the above questions, will allow us to progress beyond the large-scale, static picture of convection in the polar ionosphere. Answering the open questions on ionospheric flow channels will allow us to move towards a more comprehensive understanding of the role of mesoscale high velocity features in the polar cap and their importance in the solar wind-magnetosphere-ionosphere system.

Bibliography

Alfvén, H. (1942), Existence of electromagnetic-hydrodynamic waves, *Nature*, *150*(3805), 405–406. 2.1

Andalsvik, Y., P. Sandholt, and C. Farrugia (2011), Dayside and nightside contributions to cross-polar cap potential variations: the 20 March 2001 ICME case, in *Annales Geophysicae*, vol. 29, p. 2189, Copernicus GmbH. 2.14, 2.15, 2.15, 3.5, 5.1, 5.3.2, 5.4, 5.5

Anderson, B., K. Takahashi, T. Kamei, C. Waters, and B. Toth (2002), Birkeland current system key parameters derived from Iridium observations: Method and initial validation results, *Journal of Geophysical Research: Space Physics*, *107*(A6), SMP–11. 3.2

Anderson, B., H. Korth, C. Waters, D. Green, V. Merkin, R. Barnes, and L. Dyrud (2014), Development of large-scale Birkeland currents determined from the Active Magnetosphere and Planetary Electrodynamics Response Experiment, *Geophysical Research Letters*, *41*(9), 3017–3025. 3.2

Anderson, B. J., K. Takahashi, and B. A. Toth (2000), Sensing global Birkeland currents with Iridium® engineering magnetometer data, *Geophysical Research Letters*, *27*(24), 4045–4048. 3.2

Angelopoulos, V., W. Baumjohann, C. Kennel, F. V. Coroniti, M. Kivelson, R. Pellat, R. Walker, H. Lühr, and G. Paschmann (1992), Bursty bulk flows in the inner central plasma sheet, *Journal of Geophysical Research: Space Physics*, *97*(A4), 4027–4039. 2.10.1

Auster, H., K. Glassmeier, W. Magnes, O. Aydogar, W. Baumjohann, D. Constantinescu, D. Fischer, K. Fornacon, E. Georgescu, P. Harvey, et al. (2008), The THEMIS fluxgate magnetometer, *Space Science Reviews*, *141*(1-4), 235–264. 3.4.1

Babcock, H. D. (1959), The Sun's Polar Magnetic Field, *The Astrophysical Journal*, *130*, 364. 2.1

Baker, K., and S. Wing (1989), A new magnetic coordinate system for conjugate studies at high latitudes, *Journal of Geophysical Research: Space Physics*, *94*(A7), 9139–9143. 2.3

Baumjohann, W., and R. A. Treumann (1997), *Basic Space Plasma Physics*, World Scientific. 2.1

Beckers, J. M., and E. Schröter (1968), The intensity, velocity and magnetic structure of a sunspot region, *Solar Physics*, *4*(2), 142–164. 2.1

Berkey, F., L. Cogger, S. Ismail, and Y. Kamide (1976), Evidence for a correlation between Sun-aligned arcs and the interplanetary magnetic field direction, *Geophysical Research Letters*, *3*(3), 145–147. 2.12

Biondi, M. A. (1969), Atmospheric electron–ion and ion–ion recombination processes, *Canadian Journal of Chemistry*, *47*(10), 1711–1719. 2.2

Birkeland, K. (1908), The norwegian aurora polaris expedition 1902–1903, vol. 1, h, *Aschehoug & Co., Christiania, Norway*. 2.6

Biskamp, D. (1996), Magnetic reconnection in plasmas, *Astrophysics and Space Science*, *242*(1-2), 165–207. 2.4

Bland, E. C., E. Heino, M. J. Kosch, and N. Partamies (2018), SuperDARN radar-derived HF radio attenuation during the September 2017 solar proton events, *Space Weather*, *16*(10), 1455–1469. 3.1.4

Bland, E. C., N. Partamies, E. Heino, A. S. Yukimatu, and H. Miyaoka (2019), Energetic electron precipitation occurrence rates determined using the Syowa East SuperDARN radar, *Journal of Geophysical Research: Space Physics*, *124*(7), 6253–6265. 3.1.4

Bristow, W., D. Hampton, and A. Otto (2016), High-spatial-resolution velocity measurements derived using Local Divergence-Free Fitting of SuperDARN observations, *Journal of Geophysical Research: Space Physics*, *121*(2), 1349–1361. 2.7

Burrell, A. G., G. Chisham, S. E. Milan, L. Kilcommons, Y.-J. Chen, E. G. Thomas, and B. Anderson (2020), AMPERE polar cap boundaries, in *Annales Geophysicae*, vol. 38, pp. 481–490, Copernicus GmbH. 3.2.1

Carter, J. A., S. E. Milan, R. Fear, A. Kullen, and M. Hairston (2015), Dayside reconnection under interplanetary magnetic field By-dominated conditions: The formation and movement of bending arcs, *Journal of Geophysical Research: Space Physics*, *120*(4), 2967–2978. 2.12

Chapman, S., and V. C. Ferraro (1930), A new theory of magnetic storms, *Nature*, *126*(3169), 129–130. 2.4, 2.6

Chisham, G., M. Lester, S. Milan, M. Freeman, W. Bristow, A. Grocott, K. McWilliams, J. Ruohoniemi, T. Yeoman, P. L. Dyson, et al. (2007), A decade of the Super Dual Auroral Radar Network (SuperDARN): Scientific achievements, new techniques and future directions, *Surveys in geophysics*, *28*(1), 33–109. 3.1

Coleman Jr, P., L. Davis, and C. Sonett (1960), Steady component of the interplanetary magnetic field: Pioneer V, *Physical Review Letters*, *5*(2), 43. 2.1

Cousins, E., and S. Shepherd (2010), A dynamical model of high-latitude convection derived from SuperDARN plasma drift measurements, *Journal of Geophysical Research: Space Physics*, *115*(A12). 2.7

Cowley, S. (2000), Magnetosphere-ionosphere interactions: A tutorial review, *Magnetospheric Current Systems, Geophys. Monogr. Ser*, *118*, 91–106. 2.6

Cowley, S., and M. Lockwood (1992), Excitation and decay of solar wind-driven flows in the magnetosphere-ionosphere system, *Annales Geophysicae*, *10*(1-2), 103–115. 2.5, 2.5, 2.11

Coxon, J., S. Milan, L. Clausen, B. Anderson, and H. Korth (2014), The magnitudes of the regions 1 and 2 Birkeland currents observed by AMPERE and their role in solar wind-magnetosphere-ionosphere coupling, *Journal of Geophysical Research: Space Physics*, *119*(12), 9804–9815. 2.6, 2.7

Coxon, J., S. Milan, J. Carter, L. Clausen, B. Anderson, and H. Korth (2016), Seasonal and diurnal variations in AMPERE observations of the Birkeland currents compared to modeled results, *Journal of Geophysical Research: Space Physics*, *121*(5), 4027–4040. 3.2.2

Deng, Y., R. Heelis, L. R. Lyons, Y. Nishimura, and C. Gabrielse (2019), Impact of flow bursts in the auroral zone on the ionosphere and thermosphere, *Journal of Geophysical Research: Space Physics*, *124*(12), 10,459–10,467. 6.2

Dungey, J. W. (1961), Interplanetary magnetic field and the auroral zones, *Physical Review Letters*, *6*(2), 47. 2.4

ESA (2012), Iridium constellation, https://www.esa.int/ESA_Multimedia/Images/2012/11/Iridium_NEXT_constellation, [Online; accessed 20 September 2020]. 3.6

Fæhn Follestad, A., K. Herlingshaw, H. Ghadjari, D. Knudsen, K. McWilliams, J. Moen, A. Spicher, J. Wu, and K. Oksavik (2020), Dayside field-aligned current impacts on ionospheric irregularities, *Geophysical Research Letters*, *47*(11), e2019GL086,722. (document)

Farris, M., and C. Russell (1994), Determining the standoff distance of the bow shock: Mach number dependence and use of models, *Journal of Geophysical Research: Space Physics*, *99*(A9), 17,681–17,689. 2.4, 3.4

Farrugia, C., P. Sandholt, M. Lester, S. Cowley, W. Denig, B. Lybekk, and E. Trondsen (2001), Auroral dynamics in relation to plasma sheet particle injections during substorm expansions, *AGUSM*, *2001*, SM52A–11. 2.10.1

Farrugia, C., E. Lund, P. Sandholt, J. Wild, S. Cowley, A. Balogh, C. Mouikis, E. Mobius, M. Dunlop, J. Bosqued, et al. (2004), Pulsed flows at the high-altitude cusp poleward boundary, and associated ionospheric convection and particle signatures, during a Cluster-FAST-SuperDARN-Søndrestrøm conjunction under a southwest IMF, in *Annales Geophysicae*, vol. 22, pp. 2891–2905. 2.11

Fasel, G., L. Lee, and R. Smith (1993), A mechanism for the multiple brightenings of dayside poleward-moving auroral forms, *Geophysical Research Letters*, *20*(20), 2247–2250. 2.13

Fasel, G. J. (1995), Dayside poleward moving auroral forms: A statistical study, *Journal of Geophysical Research: Space Physics*, *100*(A7), 11,891–11,905. 2.13

Föerster, M., G. Paschmann, S. Haaland, J. Quinn, R. Torbert, H. Vaith, and C. Kletzing (2007), High-latitude plasma convection from Cluster EDI: variances and solar wind correlations, *Annales Geophysicae*, *25*. 2.7

Formisano, V. (1979), Orientation and shape of the Earth's bow shock in three dimensions, *Planetary and Space Science*, *27*(9), 1151–1161. 2.4

Förster, M., and S. Haaland (2015), Interhemispheric differences in ionospheric convection: Cluster EDI observations revisited, *Journal of Geophysical Research: Space Physics*, *120*(7), 5805–5823. 2.7

Förster, M., Y. Feldstein, S. Haaland, L. Dremukhina, L. Gromova, and A. Levitin (2009), Magnetospheric convection from Cluster EDI measurements compared with the ground-based ionospheric convection model IZMEM, in *Annales Geophysicae*, vol. 27, pp. 3077–3087, Copernicus GmbH. 2.7

Forsyth, C., V. Sergeev, M. Henderson, Y. Nishimura, and B. Gallardo-Lacourt (2020), Physical processes of meso-scale, dynamic auroral forms, *Space Science Reviews*, *216*, 1–45. 2.10.2

Foster, J., and W. Burke (2002), SAPS: A new categorization for sub-auroral electric fields, *Eos, Transactions American Geophysical Union*, *83*(36), 393–394. 2.11

Foster, J., J. M. Holt, R. Musgrove, and D. Evans (1986), Ionospheric convection associated with discrete levels of particle precipitation, *Geophysical Research Letters*, *13*(7), 656–659. 2.7

Foster, J. C. (1983), An empirical electric field model derived from Chatanika radar data, *Journal of Geophysical Research: Space Physics*, *88*(A2), 981–987. 2.7

Frank, L. A., J. D. Craven, J. Burch, and J. D. Winningham (1982), Polar views of the Earth's aurora with Dynamics Explorer, *Geophysical Research Letters*, *9*(9), 1001–1004. 2.12

Frey, H. U., D. Han, R. Kataoka, M. R. Lessard, S. E. Milan, Y. Nishimura, R. J. Strangeway, and Y. Zou (2019), Dayside aurora, *Space Science Reviews*, *215*(8), 51. 2.14

Friis-Christensen, E., Y. Kamide, A. Richmond, and S. Matsushita (1985), Interplanetary magnetic field control of high-latitude electric fields and currents determined from Greenland magnetometer data, *Journal of Geophysical Research: Space Physics*, *90*(A2), 1325–1338. 2.7

Gabrielse, C., Y. Nishimura, L. Lyons, B. Gallardo-Lacourt, Y. Deng, and E. Donovan (2018), Statistical properties of mesoscale plasma flows in the nightside high-latitude ionosphere, *Journal of Geophysical Research: Space Physics*, *123*(8), 6798–6820. 5.1, 5.3.1, 5.3.2, 5.3.3

Gallardo-Lacourt, B., Y. Nishimura, L. Lyons, S. Zou, V. Angelopoulos, E. Donovan, K. McWilliams, J. Ruohoniemi, and N. Nishitani (2014), Coordinated SuperDARN THEMIS ASI observations of mesoscale flow bursts associated with auroral streamers, *Journal of Geophysical Research: Space Physics*, *119*(1), 142–150. 2.10, 2.12, 2.10.1

Gillies, R., G. Hussey, G. Sofko, K. McWilliams, R. Fiori, P. Ponomarenko, and J.-P. St.-Maurice (2009), Improvement of SuperDARN velocity measurements by estimating the index of refraction in the scattering region using interferometry, *Journal of Geophysical Research: Space Physics*, *114*(A7). 5.3.2

Glassmeier, K.-H., and M. Stellmacher (1996), Mapping flux transfer events to the ionosphere, *Advances in Space Research*, *18*(8), 151–160. 2.9

Goertz, C., E. Nielsen, A. Korth, K. H. Glassmeier, C. Haldoupis, P. Hoeg, and D. Hayward (1985), Observations of a possible ground signature of flux transfer events, *Journal of Geophysical Research: Space Physics*, *90*(A5), 4069–4078. 2.9.1

Goodwin, L., Y. Nishimura, Y. Zou, K. Shiokawa, and P. Jayachandran (2019), Mesoscale convection structures associated with airglow patches characterized using Cluster-imager conjunctions, *Journal of Geophysical Research: Space Physics*, *124*(9), 7513–7532. 2.13

Gosling, J., M. Thomsen, S. Bame, R. Elphic, and C. Russell (1990), Plasma flow reversals at the dayside magnetopause and the origin of asymmetric polar cap convection, *Journal of Geophysical Research: Space Physics*, *95*(A6), 8073–8084. 2.6

Greenwald, R., K. Baker, J. Dudeney, M. Pinnock, T. Jones, E. Thomas, J. Villain, J. Cerisier, C. Senior, C. Hanuise, et al. (1995), DARN/SuperDARN: A global view of the dynamics of high-latitude convection, *Space Science Reviews*, *71*, 761–796. 3.1, 3.1.1

Gussenhoven, M. (1982), Extremely high latitude auroras, *Journal of Geophysical Research: Space Physics*, *87*(A4), 2401–2412. 2.12

Haaland, S., G. Paschmann, M. Förster, J. Quinn, R. Torbert, C. McIlwain, H. Vaith, P. Puhl-Quinn, and C. Kletzing (2007), High-latitude plasma convection from Cluster EDI measurements: method and IMF-dependence, *Annales Geophysicae*, *25*(1), 239–253. 2.7, 3.4.1

Haerendel, G., G. Paschmann, N. Sckopke, H. Rosenbauer, and P. Hedgecock (1978), The frontside boundary layer of the magnetosphere and the problem of reconnection, *Journal of Geophysical Research: Space Physics*, *83*(A7), 3195–3216. 2.9

Hairston, M., and R. Heelis (1990), Model of the high-latitude ionospheric convection pattern during southward interplanetary magnetic field using DE 2 data, *Journal of Geophysical Research: Space Physics*, *95*(A3), 2333–2343. 2.7

Heelis, R. (1984), The effects of interplanetary magnetic field orientation on dayside high-latitude ionospheric convection, *Journal of Geophysical Research: Space Physics*, *89*(A5), 2873–2880. 2.4

Henderson, M., G. Reeves, and J. Murphree (1998), Are north-south aligned auroral structures an ionospheric manifestation of bursty bulk flows?, *Geophysical Research Letters*, *25*(19), 3737–3740. 2.10.1

Heppner, J., and N. Maynard (1987), Empirical high-latitude electric field models, *Journal of Geophysical Research: Space Physics*, *92*(A5), 4467–4489. 2.4, 2.7, 3.1.3

Heppner, J. P. (1977), Empirical models of high-latitude electric fields, *Journal of Geophysical Research*, *82*(7), 1115–1125. 2.7

Hoeksema, J. T. (1995), The large-scale structure of the heliospheric current sheet during the Ulysses epoch, in *The High Latitude Heliosphere*, pp. 137–148, Springer. 2.1

Holt, J., R. Wand, J. Evans, and W. Oliver (1987), Empirical models for the plasma convection at high latitudes from Millstone Hill observations, *Journal of Geophysical Research: Space Physics*, *92*(A1), 203–212. 2.7

Horwitz, J. L., and S.-I. Akasofu (1977), The response of the dayside aurora to sharp northward and southward transitions of the interplanetary magnetic field and to magnetospheric substorms, *Journal of Geophysical Research*, *82*(19), 2723–2734. 2.13

Hosokawa, K., T. Iyemori, A. S. Yukimatu, and N. Sato (2001), Source of field-aligned irregularities in the subauroral F region as observed by the SuperDARN radars, *Journal of Geophysical Research: Space Physics*, *106*(A11), 24,713–24,731. 3.1.1

Huang, C.-S., G. Sofko, A. Koustov, J. MacDougall, R. Greenwald, J. Ruohoniemi, J.-P. Villain, M. Lester, J. Watermann, V. Papitashvili, et al. (2001), Long-period magnetospheric-ionospheric perturbations during northward interplanetary magnetic field, *Journal of Geophysical Research: Space Physics*, *106*(A7), 13,091–13,103. 2.5

Iijima, T., and T. A. Potemra (1978), Large-scale characteristics of field-aligned currents associated with substorms, *Journal of Geophysical Research: Space Physics*, *83*(A2), 599–615. 2.6

Jin, Y., J. I. Moen, and W. J. Miloch (2015), On the collocation of the cusp aurora and the GPS phase scintillation: A statistical study, *Journal of Geophysical Research: Space Physics*, *120*(10), 9176–9191. 5.4

Jørgensen, T. S., E. Friis-Christensen, and J. Wilhjelm (1972), Interplanetary magnetic-field direction and high-latitude ionospheric currents, *Journal of Geophysical Research*, *77*(10), 1976–1977. 2.5

Kauristie, K., V. Sergeev, O. Amm, M. Kubyshkina, J. Jussila, E. Donovan, and K. Liou (2003), Bursty bulk flow intrusion to the inner plasma sheet as inferred from auroral observations, *Journal of Geophysical Research: Space Physics*, *108*(A1). 2.10.1

King, J., and N. Papitashvili (2006), One min and 5-min solar wind data sets at the Earth's bow shock nose, *NASA Goddard Space Flight Cent., Greenbelt, Md*. 3.4

Kivelson, M. G., M. G. Kivelson, and C. T. Russell (1995), *Introduction to space physics*, Cambridge university press. 2.4

Koustov, A., D. Danskin, R. Makarevitch, and J. Gorin (2005), On the relationship between the velocity of E-region HF echoes and E× B plasma drift, *Annales Geophysicae*, *23*. 2.10.1, 5.5

Koustov, A., D. Lavoie, and R. Varney (2016), On the consistency of the SuperDARN radar velocity and E× B plasma drift, *Radio Science*, *51*(11), 1792–1805. 5.3.2

Kullen, A., R. Fear, S. E. Milan, J. Carter, and T. Karlsson (2015), The statistical difference between bending arcs and regular polar arcs, *Journal of Geophysical Research: Space Physics*, *120*(12), 10–443. 2.12

Laundal, K. M., and A. D. Richmond (2017), Magnetic coordinate systems, *Space Science Reviews*, *206*(1-4), 27–59. 2.3

Lindsay, G., C. Russell, and J. Luhmann (1995), Coronal mass ejection and stream interaction region characteristics and their potential geomagnetic effectiveness, *Journal of Geophysical Research: Space Physics*, *100*(A9), 16,999–17,013. 2.1

Lockwood, M., and M. Wild (1993), On the quasi-periodic nature of magnetopause flux transfer events, *Journal of Geophysical Research: Space Physics*, *98*(A4), 5935–5940. 2.9.2

Lockwood, M., S. W. H. Cowley, P. E. Sandholt, and R. P. Lepping (1990), The ionospheric signatures of flux transfer events and solar wind dynamic pressure changes, *Journal of Geophysical Research: Space Physics*, *95*(A10), 17,113–17,135, doi: 10.1029/JA095iA10p17113. 2.11, 5.3.1

Lorentzen, D., J. Moen, K. Oksavik, F. Sigernes, Y. Saito, and M. Johnsen (2010), In situ measurement of a newly created polar cap patch, *Journal of Geophysical Research: Space Physics*, *115*(A12). 2.13

Lyons, L., Y. Nishimura, H.-J. Kim, E. Donovan, V. Angelopoulos, G. Sofko, M. Nicolls, C. Heinselman, J. Ruohoniemi, and N. Nishitani (2011), Possible connection of polar cap flows to pre-and post-substorm onset PBIs and streamers, *Journal of Geophysical Research: Space Physics*, *116*(A12). 2.10.1

Lyons, L., Y. Nishimura, and Y. Zou (2016), Unsolved problems: Mesoscale polar cap flow channels' structure, propagation, and effects on space weather disturbances, *Journal of Geophysical Research: Space Physics*, *121*(4), 3347–3352. 2.8, 2.13

MacDougall, J. W., and P. T. Jayachandran (2001), Polar cap convection relationships with solar wind, *Radio Science*, *36*(6), 1869–1880, doi:10.1029/2001RS001007. 1, 5.3.2

Mansurov, S. (1969), New evidence of a relationship between magnetic fields in space and on Earth, *Geomag. Aeron.*, *9*, 622–623. 2.5

Marchaudon, A., J.-C. Cerisier, R. Greenwald, and G. Sofko (2004), Electrodynamics of a flux transfer event: Experimental test of the Southwood model, *Geophysical research letters*, *31*(9). 2.9.1, 2.10, 5.1

Mikko Syrjäsuo (UNIS) (2017), Image of the SuperDARN Longyearbyen Radar, http://www.radio-science.net/2017/10/phasing-difference.html, [Online; accessed 20 September 2020]. 3.2

Milan, S., T. Jones, T. Robinson, E. Thomas, and T. Yeoman (1997a), Interferometric evidence for the observation of ground backscatter originating behind the CUTLASS coherent HF radars, in *Annales Geophysicae*, vol. 15, pp. 29–39, Springer. 3.1

Milan, S., T. Yeoman, M. Lester, E. Thomas, and T. Jones (1997b), Initial backscatter occurrence statistics from the CUTLASS HF radars, in *Annales Geophysicae*, vol. 15, pp. 703–718, Springer. 3.3, 3.1.1, 3.1.4

Milan, S., J. Davies, and M. Lester (1999), Coherent HF radar backscatter characteristics associated with auroral forms identified by incoherent radar techniques: a comparison of CUTLASS and EISCAT observations, *Journal of Geophysical Research: Space Physics*, *104*(A10), 22,591–22,604. 3.1.4

Milan, S., M. Lester, S. Cowley, and M. Brittnacher (2000), Convection and auroral response to a southward turning of the IMF: Polar UVI, CUTLASS, and IMAGE signatures of transient magnetic flux transfer at the magnetopause, *Journal of Geophysical Research: Space Physics*, *105*(A7), 15,741–15,755. 2.13

Milan, S., J. Carter, H. Korth, and B. Anderson (2015), Principal component analysis of Birkeland currents determined by the Active Magnetosphere and Planetary Electrodynamics Response Experiment, *Journal of Geophysical Research: Space Physics*, *120*(12), 10–415. 3.7, 3.2.1, 3.2.2, 5.5

Milan, S. E., L. B. N. Clausen, J. C. Coxon, J. A. Carter, M.-T. Walach, K. Laundal, N. Østgaard, P. Tenfjord, J. Reistad, K. Snekvik, et al. (2017), Overview of solar wind–magnetosphere–ionosphere–atmosphere coupling and the generation of magnetospheric currents, *Space Science Reviews*, *206*(1-4), 547–573. 2.6

Moen, J., P. Sandholt, M. Lockwood, W. Denig, U. Løvhaug, B. Lybekk, A. Egeland, D. Opsvik, and E. Friis-Christensen (1995), Events of enhanced convection and related dayside auroral activity, *Journal of Geophysical Research: Space Physics*, *100*(A12), 23,917–23,934. 1, 2.11, 2.14, 5.5, 6.2

Moen, J., Y. Rinne, H. Carlson, K. Oksavik, R. Fujii, and H. Opgenoorth (2008), On the relationship between thin Birkeland current arcs and reversed flow channels in the winter cusp/cleft ionosphere, *Journal of Geophysical Research: Space Physics*, *113*(A9). 2.9.3

NASA (2020), Illustration of Earth's Magnetosphere and the Solar Wind, https://science.nasa.gov/heliophysics/focus-areas/magnetosphere-ionosphere, [Online; accessed 20 September 2020]. 1.1

Neudegg, D., S. Cowley, S. Milan, T. K. Yeoman, M. Lester, G. Provan, G. Haerendel, W. Baumjohann, B. Nikutowski, J. Büchner, et al. (2000), A survey of magnetopause FTEs and associated flow bursts in the polar ionosphere, in *Annales Geophysicae*, vol. 18, pp. 416–435, Copernicus GmbH. 2.5, 2.9.2

Nishida, H., H. Ogawa, and Y. Inatani (2009), MHD analysis of force acting on dipole magnetic field in magnetized plasma flow, in *Computational Fluid Dynamics 2006*, pp. 765–770, Springer. 2.1

Nishimura, Y., L. Lyons, S. Zou, X. Xing, V. Angelopoulos, S. Mende, J. Bonnell, D. Larson, U. Auster, T. Hori, et al. (2010a), Preonset time sequence of auroral substorms: Coordinated observations by all-sky imagers, satellites, and radars, *Journal of Geophysical Research: Space Physics*, *115*(A5). 2.10

Nishimura, Y., L. Lyons, S. Zou, V. Angelopoulos, and S. Mende (2010b), Substorm triggering by new plasma intrusion: THEMIS all-sky imager observations, *Journal of Geophysical Research: Space Physics*, *115*(A7). 2.10, 2.10.2

Nishimura, Y., L. R. Lyons, Y. Zou, K. Oksavik, J. Moen, L. Clausen, E. Donovan, V. Angelopoulos, K. Shiokawa, J. Ruohoniemi, et al. (2014), Day-night coupling by a localized flow channel visualized by polar cap patch propagation, *Geophysical Research Letters*, *41*(11), 3701–3709. 2.13

Nishitani, N., J. M. Ruohoniemi, M. Lester, J. B. H. Baker, A. V. Koustov, S. G. Shepherd, G. Chisham, T. Hori, E. G. Thomas, R. A. Makarevich, et al. (2019), Review of the accomplishments of mid-latitude Super Dual Auroral Radar Network (SuperDARN) HF radars, *Progress in Earth and Planetary Science*, *6*(1), 1–57. 3.1, 3.1.2

Ogilvie, K., and M. Desch (1997), The WIND spacecraft and its early scientific results, *Advances in Space Research*, *20*(4-5), 559–568. 2.1, 3.4

Ohtani, S., and A. Yoshikawa (2016), The initiation of the poleward boundary intensification of auroral emission by fast polar cap flows: A new interpretation based on ionospheric polarization, *Journal of Geophysical Research: Space Physics*, *121*(11), 10–910. 2.10.2

Ohtani, S., T. Motoba, J. Gjerloev, J. Ruohoniemi, E. Donovan, and A. Yoshikawa (2018), Longitudinal development of poleward boundary intensifications (PBIs) of auroral emission, *Journal of Geophysical Research: Space Physics*, *123*(11), 9005–9021. 2.10, 2.10.2

Oksavik, K., J. Moen, H. Carlson, R. Greenwald, S. Milan, M. Lester, W. Denig, and R. Barnes (2005), Multi-instrument mapping of the small-scale flow dynamics related to a cusp auroral transient, *Annales Geophysicae*, *23*(7), 2657–2670. 2.13

Oksavik, K., V. Barth, J. Moen, and M. Lester (2010), On the entry and transit of high-density plasma across the polar cap, *Journal of Geophysical Research: Space Physics*, *115*(A12). 5.3.2, 5.4

Oksavik, K., J. Moen, E. Rekaa, H. Carlson, and M. Lester (2011), Reversed flow events in the cusp ionosphere detected by SuperDARN HF radars, *Journal of Geophysical Research: Space Physics*, *116*(A12). 2.11, 2.9.3

Oksavik, K., C. van der Meeren, D. A. Lorentzen, L. Baddeley, and J. Moen (2015), Scintillation and loss of signal lock from poleward moving auroral forms in the cusp ionosphere, *Journal of Geophysical Research: Space Physics*, *120*(10), 9161–9175. 1

Oliver, W., J. Holt, R. Wand, and J. Evans (1983), Millstone Hill incoherent scatter observations of auroral convection over $60° < \Lambda < 75°$: 3. Average patterns versus Kp, *Journal of Geophysical Research: Space Physics*, *88*(A7), 5505–5516. 2.7

Ossakow, S., and P. Chaturvedi (1979), Current convective instability in the diffuse aurora, *Geophysical Research Letters*, *6*(4), 332–334. 3.1.1

Papitashvili, V., B. Belov, D. Faermark, Y. I. Feldstein, S. Golyshev, L. Gromova, and A. Levitin (1994), Electric potential patterns in the northern and southern polar regions parameterized by the interplanetary magnetic field, *Journal of Geophysical Research: Space Physics*, *99*(A7), 13,251–13,262. 2.7

Papitashvili, V., F. Rich, M. Heinemann, and M. Hairston (1999), Parameterization of the defense meteorological satellite program ionospheric electrostatic potentials by the interplanetary magnetic field strength and direction, *Journal of Geophysical Research: Space Physics*, *104*(A1), 177–184. 2.7

Papitashvili, V. O., and F. J. Rich (2002), High-latitude ionospheric convection models derived from Defense Meteorological Satellite Program ion drift observations and parameterized by the interplanetary magnetic field strength and direction, *Journal of Geophysical Research: Space Physics*, *107*(A8), SIA–17. 2.1, 2.7, 3.4

Parker, E. (1963), Interplanetary dynamical process, Wiley-Inter-Science, *New York*. 2.1

Paxton, L. J., C.-I. Meng, G. H. Fountain, B. S. Ogorzalek, E. H. Darlington, S. A. Gary, J. O. Goldsten, D. Y. Kusnierkiewicz, S. C. Lee, L. A. Linstrom, et al. (1992), Special sensor ultraviolet spectrographic imager: An instrument description, in *Instrumentation for planetary and terrestrial atmospheric remote sensing*, vol. 1745, pp. 2–15, International Society for Optics and Photonics. 3.9, 3.3.2

Paxton, L. J., D. Morrison, Y. Zhang, H. Kil, B. Wolven, B. S. Ogorzalek, D. C. Humm, and C.-I. Meng (2002), Validation of remote sensing products produced by the Special Sensor Ultraviolet Scanning Imager (SSUSI): A far UV-imaging spectrograph on DMSP F-16, in *Optical spectroscopic techniques, remote sensing, and instrumentation for atmospheric and space research IV*, vol. 4485, pp. 338–348, International Society for Optics and Photonics. 3.3.2

Pettigrew, E., S. Shepherd, and J. Ruohoniemi (2010), Climatological patterns of high-latitude convection in the Northern and Southern hemispheres: Dipole tilt dependencies and interhemispheric comparisons, *Journal of Geophysical Research: Space Physics*, *115*(A7). 2.7

Peymirat, C., and D. Fontaine (1997), Polar cap convection patterns inferred from EISCAT observations, in *Annales Geophysicae*, vol. 15, pp. 403–411, Springer. 2.7

Pinnock, M., A. S. Rodger, J. Dudeney, K. Baker, P. Newell, R. Greenwald, and M. Greenspan (1993), Observations of an enhanced convection channel in the cusp ionosphere, *Journal of Geophysical Research: Space Physics*, *98*(A3), 3767–3776. 1, 2.9.1, 2.10, 5.1

Ponomarenko, P., J.-P. St-Maurice, C. Waters, R. Gillies, and A. Koustov (2009), Refractive index effects on the scatter volume location and Doppler velocity estimates of ionospheric HF backscatter echoes, in *Annales Geophysicae*, vol. 27, pp. 4207–4219, Copernicus GmbH. 5.3.2

Prikryl, P., P. Jayachandran, S. Mushini, and R. Chadwick (2011), Climatology of GPS phase scintillation and HF radar backscatter for the high-latitude ionosphere under solar minimum conditions, in *Annales Geophysicae*, vol. 29, pp. 377–392, Copernicus GmbH. 5.5

Provan, G., T. Yeoman, and S. Milan (1998), CUTLASS Finland radar observations of the ionospheric signatures of flux transfer events and the resulting plasma flows, in *Annales Geophysicae*, vol. 16, pp. 1411–1422, Springer. 1, 2.9.2, 5.3.3

Provan, G., T. Yeoman, and S. Cowley (1999), The influence of the IMF By component on the location of pulsed flows in the dayside ionosphere observed by an HF radar, *Geophysical research letters*, *26*(4), 521–524. 2.9.2, 5.1, 5.4

Reidy, J., R. Fear, D. Whiter, B. Lanchester, A. Kavanagh, L. Paxton, Y. Zhang, and M. Lester (2017), Multi-instrument observation of simultaneous polar cap auroras on open and closed magnetic field lines, *Journal of Geophysical Research: Space Physics*, *122*(4), 4367–4386. 3.3.2

Rich, F. J., and M. Hairston (1994), Large-scale convection patterns observed by DMSP, *Journal of Geophysical Research: Space Physics*, *99*(A3), 3827–3844. 2.7

Richards, P. (2001), Seasonal and solar cycle variations of the ionospheric peak electron density: Comparison of measurement and models, *Journal of Geophysical Research: Space Physics*, *106*(A7), 12,803–12,819. 2.2

Ridley, A., G. Crowley, and C. Freitas (2000), An empirical model of the ionospheric electric potential, *Geophysical research letters*, *27*(22), 3675–3678. 2.7

Rijnbeek, R., S. Cowley, D. Southwood, and C. Russell (1984), A survey of dayside flux transfer events observed by ISEE 1 and 2 magnetometers, *Journal of Geophysical Research: Space Physics*, *89*(A2), 786–800. 2.9.2

Rinne, Y., J. Moen, K. Oksavik, and H. Carlson (2007), Reversed flow events in the winter cusp ionosphere observed by the European Incoherent Scatter (EISCAT) Svalbard radar, *Journal of Geophysical Research: Space Physics*, *112*(A10). 2.11, 2.9.3

Rinne, Y., J. Moen, H. Carlson, and M. Hairston (2010), Stratification of east-west plasma flow channels observed in the ionospheric cusp in response to IMF By polarity changes, *Geophysical research letters*, *37*(13). 2.13, 5.3.2

Ruohoniemi, J., and K. Baker (1998), Large-scale imaging of high-latitude convection with Super Dual Auroral Radar Network HF radar observations, *Journal of Geophysical Research: Space Physics*, *103*(A9), 20,797–20,811. 3.1.3

Ruohoniemi, J., and R. Greenwald (1996), Statistical patterns of high-latitude convection obtained from Goose Bay HF radar observations, *Journal of Geophysical Research: Space Physics*, *101*(A10), 21,743–21,763. 2.5, 2.7, 3.1.3

Ruohoniemi, J., and R. Greenwald (2005), Dependencies of high-latitude plasma convection: Consideration of interplanetary magnetic field, seasonal, and universal time factors in statistical patterns, *Journal of Geophysical Research: Space Physics*, *110*(A9). 2.7

Russell, C. T., and R. Elphic (1978), Initial ISEE magnetometer results: Magnetopause observations, *Space Science Reviews*, *22*(6), 681–715. 2.4, 2.9

Russell, C. T., and R. Elphic (1979), ISEE observations of flux transfer events at the dayside magnetopause, *Geophysical Research Letters*, *6*(1), 33–36. 2.9

Sandholt, P., and C. Farrugia (2007), Role of poleward moving auroral forms in the dawn-dusk auroral precipitation asymmetries induced by IMF By, *Journal of Geophysical Research: Space Physics*, *112*(A4). 2.11

Sandholt, P., and C. Farrugia (2009), Plasma flow channels at the dawn/dusk polar cap boundaries: momentum transfer on old open field lines and the roles of IMF By and conductivity gradients, in *Annales Geophysicae*, vol. 27, pp. 1527–1554, Copernicus GmbH. 1, 2.13, 2.11, 2.14, 2.15, 5.1, 5.3.2, 5.4

Sandholt, P., C. Deehr, A. Egeland, B. Lybekk, R. Viereck, and G. Romick (1986), Signatures in the dayside aurora of plasma transfer from the magnetosheath, *Journal of Geophysical Research: Space Physics*, *91*(A9), 10,063–10,079. 2.13

Sandholt, P., B. Lybekk, A. Egeland, R. Nakamura, and T. Oguti (1989), Midday auroral breakup, *Journal of geomagnetism and geoelectricity*, *41*(4), 371–387. 2.13

Sandholt, P., C. Farrugia, and W. Denig (2004), Detailed dayside auroral morphology as a function of local time for southeast IMF orientation: implications for solar wind-magnetosphere coupling, *Annales Geophysicae*, *22*, 3537–3560. 2.11

Sandholt, P., Y. Andalsvik, and C. Farrugia (2010), Polar cap convection/precipitation states during Earth passage of two ICMEs at solar minimum, in *Annales Geophysicae*, vol. 28, pp. 1023–1042, Copernicus GmbH. 2.14, 5.1, 5.4, 5.5

Senior, C., D. Fontaine, G. Caudal, D. Alcaydé, and J. Fontanari (1990), Convection electric fields and electrostatic potential over $61^\circ < \lambda < 72^\circ$ invariant latitude observed with the European incoherent scatter facility. 2. Statistical results, in *Annales Geophysicae, Atmospheres, Hydrospheres and Space Sciences*, vol. 8, pp. 257–272. 2.7

Smith, C. W., J. L'Heureux, N. F. Ness, M. H. Acuna, L. F. Burlaga, and J. Scheifele (1998), The ACE magnetic fields experiment, in *The Advanced Composition Explorer mission*, pp. 613–632, Springer. 2.1, 3.4

Smith, E. J. (2001), The heliospheric current sheet, *Journal of Geophysical Research: Space Physics*, *106*(A8), 15,819–15,831. 2.1

Sotirelis, T., P. T. Newell, and C.-I. Meng (1998), Shape of the open–closed boundary of the polar cap as determined from observations of precipitating particles by up to four DMSP satellites, *Journal of Geophysical Research: Space Physics*, *103*(A1), 399–406. 3.2.2

Southwood, D. (1985), Theoretical aspects of ionosphere-magnetosphere-solar wind coupling, *Advances in space research*, *5*(4), 7–14. 2.9

Southwood, D. (1987), The ionospheric signature of flux transfer events, *Journal of Geophysical Research: Space Physics*, *92*(A4), 3207–3213. 2.9, 2.9.1, 2.9.3

Southwood, D., and W. Hughes (1983), Theory of hydromagnetic waves in the magnetosphere, *Space Science Reviews*, *35*(4), 301–366. 2.9

SpaceWeatherLive (2020), Image of the geocentric solar magnetospheric coordinate system, https://www.spaceweatherlive.com/en/help/the-interplanetary-magnetic-field-imf, [Online; accessed 20 September 2020]. 2.3

Spicher, A., K. Deshpande, Y. Jin, K. Oksavik, M. D. Zettergren, L. B. Clausen, J. I. Moen, M. R. Hairston, and L. Baddeley (2020), On the production of ionospheric irregularities via Kelvin-Helmholtz instability associated with cusp flow channels, *Journal of Geophysical Research: Space Physics*, *125*(6), e2019JA027,734. 1

Spiro, R., R. Heelis, and W. Hanson (1979), Rapid subauroral ion drifts observed by Atmosphere Explorer C, *Geophysical Research Letters*, *6*(8), 657–660. 2.11

Stern, D. P. (1984), Magnetospheric dynamo processes, *Magnetospheric currents*, *28*, 200–207. 5.5

Svalgaard, L. (1969), Sector structure of the interplanetary magnetic field and daily variation of the geomagnetic field at high latitudes, *Geophys. Paper*. 2.5

The Comet Program® (2018), Figure showing the layers of the atmosphere and ionosphere, http://kejian1.cmatc.cn/vod/comet/oceans/radio_waves/print.php.htm, [Online; accessed 20 September 2020]. 2.2

Thomas, E., and S. Shepherd (2018), Statistical patterns of ionospheric convection derived from mid-latitude, high-latitude, and polar SuperDARN HF radar observations, *Journal of Geophysical Research: Space Physics*, *123*(4), 3196–3216. 2.7

Van Eyken, A., H. Rishbeth, D. Willis, and S. Cowley (1984), Initial EISCAT observations of plasma convection at invariant latitudes 70°–77°, *Journal of Atmospheric and Terrestrial Physics*, *46*(6-7), 635–641. 2.9.1

Vincent Fournier (2010), Image of the Kjell Henriksen Observatory, http://www.vincentfournier.co.uk/www/b0032p-0083-201/, [Online; accessed 20 September 2020]. 3.8

Vorobjev, V., G. Gustafsson, G. Starkov, Y. I. Feldstein, and N. Shevnina (1975), Dynamics of day and night aurora during substorms, *Planetary and Space Science*, *23*(2), 269–278. 2.13

VT SuperDARN (2020), Field-of-view plot, http://vt.superdarn.org/tiki-index.php?page=DaViT+Multi+Scan+Plot, [Online; accessed 20 September 2020]. 3.4

Walsh, B., T. Bhakyapaibul, and Y. Zou (2019), Quantifying the uncertainty of using solar wind measurements for geospace inputs, *Journal of Geophysical Research: Space Physics*, *124*(5), 3291–3302. 3.4.1

Wang, B., Y. Nishimura, L. Lyons, Y. Zou, H. Carlson, H. Frey, and S. Mende (2016), Analysis of close conjunctions between dayside polar cap airglow patches and flow channels by all-sky imager and DMSP, *Earth, Planets and Space*, *68*, 150, doi:10.1186/s40623-016-0524-z. 5.3.3

Wang, H., H. Lühr, S. Ma, and P. Ritter (2005), Statistical study of the substorm onset: its dependence on solar wind parameters and solar illumination, *Annales Geophysicae*, *23*(6), 2069–2079. 5.5

Wang, H., H. Lühr, and A. J. Ridley (2010), Plasma convection jets near the poleward boundary of the nightside auroral oval and their relation to Pedersen conductivity gradients, in *Annales Geophysicae*, vol. 28, pp. 969–976. 2.14

Waters, C., B. Anderson, and K. Liou (2001), Estimation of global field aligned currents using the Iridium® system magnetometer data, *Geophysical Research Letters*, *28*(11), 2165–2168. 3.2

Weber, E., J. Klobuchar, J. Buchau, H. Carlson Jr, R. Livingston, O. de La Beaujardiere, M. McCready, J. Moore, and G. Bishop (1986), Polar cap F layer patches: Structure and dynamics, *Journal of Geophysical Research: Space Physics*, *91*(A11), 12,121–12,129. 2.13

Weimer, D. (1995), Models of high-latitude electric potentials derived with a least error fit of spherical harmonic coefficients, *Journal of Geophysical Research: Space Physics*, *100*(A10), 19,595–19,607. 2.7

Weimer, D. (1996), A flexible, IMF dependent model of high-latitude electric potentials having "space weather" applications, *Geophysical Research Letters*, *23*(18), 2549–2552. 2.7

Weimer, D. (2005), Improved ionospheric electrodynamic models and application to calculating joule heating rates, *Journal of Geophysical Research: Space Physics*, *110*(A5). 2.7

Wild, J. A., and A. Grocott (2008), The influence of magnetospheric substorms on SuperDARN radar backscatter, *Journal of Geophysical Research: Space Physics*, *113*(A4). 5.5

Xing, X., L. Lyons, Y. Nishimura, V. Angelopoulos, D. Larson, C. Carlson, J. Bonnell, and U. Auster (2010), Substorm onset by new plasma intrusion: THEMIS spacecraft observations, *Journal of Geophysical Research: Space Physics*, *115*(A10). 2.10.1

Yeoman, T., P. Hanlon, and K. McWilliams (2002), Letter to the editor: A statistical study of the location and motion of the HF radar cusp, *Annales Geophysicae*, *20*, 275–280. 5.5

Yeoman, T. K., D. Wright, A. Stocker, and T. Jones (2001), An evaluation of range accuracy in the Super Dual Auroral Radar Network over-the-horizon HF radar systems, *Radio Science*, *36*(4), 801–813. 3.1.4

Zesta, E., E. Donovan, L. Lyons, G. Enno, J. Murphree, and L. Cogger (2002), Two-dimensional structure of auroral poleward boundary intensifications, *Journal of Geophysical Research: Space Physics*, *107*(A11), SIA–6. 2.10.1, 2.10.2

Zesta, E., Y. Shi, E. Donovan, E. Spanswick, L. R. Lyons, V. Angelopoulos, J. McFadden, C. Carlson, H.-U. Auster, S. Mende, et al. (2011), Ionospheric convection signatures of tail fast flows during substorms and Poleward Boundary Intensifications (PBI), *Geophysical research letters*, *38*(8). 2.10.1

Zhang, S.-R., J. M. Holt, and M. McCready (2007), High latitude convection based on long-term incoherent scatter radar observations in North America, *Journal of atmospheric and solar-terrestrial physics*, *69*(10-11), 1273–1291. 2.7

Zmuda, A., J. Martin, and F. T. Heuring (1966), Transverse magnetic disturbances at 1100 kilometers in the auroral region, *Journal of geophysical research*, *71*(21), 5033–5045. 2.6

Zou, Y., Y. Nishimura, L. Lyons, E. Donovan, J. Ruohoniemi, N. Nishitani, and K. McWilliams (2014), Statistical relationships between enhanced polar cap flows and PBIs, *Journal of Geophysical Research: Space Physics*, *119*(1), 151–162. 1, 2.10, 2.10.1, 2.12, 2.10.2, 5.5

Zou, Y., Y. Nishimura, L. R. Lyons, E. F. Donovan, K. Shiokawa, J. M. Ruohoniemi, K. A. McWilliams, and N. Nishitani (2015a), Polar cap precursor of nightside auroral oval intensifications using polar cap arcs, *Journal of Geophysical Research: Space Physics*, *120*(12), 10–698. 2.12

Zou, Y., Y. Nishimura, L. R. Lyons, K. Shiokawa, E. F. Donovan, J. M. Ruohoniemi, K. A. McWilliams, and N. Nishitani (2015b), Localized polar cap flow enhancement tracing using airglow patches: Statistical properties, IMF dependence, and contribution to polar cap convection, *Journal of Geophysical Research: Space Physics*, *120*(5), 4064–4078. 2.13, 5.3.2, 5.3.3

Paper I

A Study of Automatically Detected Flow Channels in the Polar Cap Ionosphere

K. Herlingshaw, L. J. Baddeley, K. Oksavik, D. A. Lorentzen, and E. C. Bland

Journal of Geophysical Research, Vol. 124, doi:10.1029/2019JA026916 (2019)

JGR Space Physics

RESEARCH ARTICLE
10.1029/2019JA026916

A Study of Automatically Detected Flow Channels in the Polar Cap Ionosphere

K. Herlingshaw[1,2], L. J. Baddeley[1,2], K. Oksavik[1,2], D. A. Lorentzen[1,2], and E. C. Bland[1,2]

[1]Department of Arctic Geophysics, University Centre in Svalbard, Longyearbyen, Norway, [2]Birkeland Centre for Space Science, University of Bergen, Bergen, Norway

Key Points:
- Polar cap flow channels can account for a substantial amount (40–60%) of the cross polar cap potential
- Flow channels can form due to dayside reconnection or appear on the edge of polar cap arcs
- Magnetic field lines that opened 25 min ago can still cause fast flow channels deep inside the polar cap

Correspondence to:
K. Herlingshaw,
Katie.Herlingshaw@unis.no

Citation:
Herlingshaw, K., Baddeley, L. J., Oksavik, K., Lorentzen, D. A., & Bland, E. C. (2019). A study of automatically detected flow channels in the polar cap ionosphere. *Journal of Geophysical Research: Space Physics*, *124*, 9430–9447. https://doi.org/10.1029/2019JA026916

Received 3 MAY 2019
Accepted 19 OCT 2019
Accepted article online 30 OCT 2019
Published online 13 NOV 2019

Abstract This paper presents a new algorithm for detecting high-speed flow channels in the polar cap. The algorithm was applied to Super Dual Auroral Radar Network data, specifically to data from the new Longyearbyen radar. This radar is located at 78.2°N, 16.0°E geographical coordinates looking north-east, and is therefore at an ideal location to measure flow channels in the high-latitude polar cap. The algorithm detected >500 events over 1 year of observations, and within this paper two case studies are considered in more detail. A flow channel on "old-open field lines" located on the dawn flank was directly driven under quiet conditions over 13 min. This flow channel contributed to a significant fraction (60%) of the cross polar cap potential and was located on the edge of a polar cap arc. Another case study follows the development of a flow channel on newly opened field lines within the cusp. This flow channel is a spontaneously driven event forming under strong solar wind driving and is intermittently excited over the course of almost an hour. As they provide a high fraction of the cross polar cap potential, these small-scale structures are vital for understanding the transport of magnetic flux over the polar cap.

1. Introduction

For southward interplanetary magnetic field (IMF), the high-latitude plasma convection in the ionosphere can be described on the large scale as twin-cell convection, which flows antisunward across the polar cap and returns to the dayside at auroral latitudes. The flow is usually assumed to be constant over thousands of kilometers with typical speeds of several hundreds of meters per second (MacDougall & Jayachandran, 2001). However, on a smaller scale (100–500 km), convection within the polar cap is not a uniform, laminar flow but is instead frequently driven by dynamic mesoscale phenomena. These structured flow enhancements occur at many locations and are classified under different names within the literature depending on their location, speed, size, and duration. Pinnock et al. (1993) reported a class of longitudinally extended flow channel events (FCEs) within Southern Hemisphere radar data, where the plasma within the flow channels traveled with speeds of 2–3 km/s within the dayside cusp. These features were suggested to be an ionospheric manifestation of flux transfer events (FTEs), which are reconnection events at the dayside magnetopause with a mean recurrence rate of 7–8 min (Haerendel et al., 1978; Russell & Elphic, 1978, 1979). The ionospheric response to transient dayside reconnection has been observed and named differently depending on the context in which it was observed. This can introduce confusion as the observations are linked and in some cases can describe the same phenomenon.

One of the other radar signatures of dayside reconnection linked to FTEs and FCEs was detected in Super Dual Auroral Radar Network (SuperDARN) data and named pulsed ionospheric flows (PIFs; Provan et al., 1998, 1999). These periodic bursts of antisunward convection, detected initially by the SuperDARN radar located in Finland, have a typical recurrence rate of 7–8 min but this can vary between 5 and 12 min. Neudegg et al. (2000) identified a statistical link between FTEs and high speed flows in the polar ionosphere (such as PIFs/FCEs) with over 99% confidence by using Equator-S satellite data and SuperDARN data to observe the effects of FTEs propagating from the magnetosphere to the ionosphere. McWilliams et al. (2000) found the occurrence rates and repetition rates of PIFs to be very similar to that of FTEs and poleward moving auroral forms, the optical manifestations of FTEs (Denig et al., 1993; Milan et al., 1999, 2000; Sandholt et al., 1990, 1993; Thorolfsson et al., 2000).

Journal of Geophysical Research: Space Physics 10.1029/2019JA026916

In addition to poleward moving auroral forms, polar cap arcs (PCAs) are also optical features associated with flow channels. PCAs are caused by precipitating electrons that are often accelerated through a field-aligned potential drop and occur primarily under the influence of a northward IMF and quiet geomagnetic conditions. They are known to be associated with flow shears and therefore flow channels, where the potential drop across the flow channel is typically ~10 kV and can account for ~10–40% of the cross polar cap potential (Zou et al., 2015a, 2015b).

Flow channels (FCs) have also been observed in locations other than the cusp, and their temporal evolution has been described by dividing them into four categories: FC 1, FC 2, FC 3, and FC 4 (Sandholt & Farrugia, 2009). FC 1 and FC 2 are driven by dayside reconnection and occur at different stages of evolution of the opened field lines. Both FC 1 and FC 2 arise from the closure of field-aligned currents via ionospheric Pedersen currents, but they differ as FC 1 occurs on newly opened field lines (time since reconnection <10 min), whereas FC 2 occurs on "old-open field lines," which underwent reconnection 10–30 min earlier (Andalsvik et al., 2011; Sandholt & Farrugia, 2009). PIFs occur on newly opened field lines (corresponding to FC 1) in the cusp, while FC 2 is located immediately poleward of the auroral oval on the dawn and dusk flanks (06–09/15–18 magnetic local time (MLT)). FC 2 are 200–300 km wide channels of enhanced antisunward flow which typically last for 5–10 min. They are attributed to momentum transfer from the high-latitude and flank boundary layers on the downstream side of the cusp via the C1-C2 cusp currents. The C1-C2 cusp currents (Farrugia et al., 2003; Sandholt et al., 2010) form the system responsible for momentum transfer from the high-latitude and flank boundary layers on the downstream side of the cusp on old-open field lines. These channels can either be "directly driven" by southward turnings in the IMF after an appropriate time delay, or "spontaneous" events occurring during stable periods of southward IMF where the channel is intermittently excited (Sandholt et al., 2010). An IMF B_y-induced asymmetry in the location of FC 2 is noted by Sandholt and Farrugia (2012), as FC 2 is located mainly on the postnoon/dusk (prenoon/dawn) side of the polar cap for IMF $B_y < 0$ (>0) conditions. Andalsvik et al. (2011) expands on this framework by defining a polar cap flow channel as a latitudinally restricted (a few 100 km) regime of enhanced antisunward convection >1 km/s and studies the dayside and nightside sources of polar cap convection events. FC 3 (premidnight/postmidnight sectors) and FC 4 (linked to streamers) are driven by nightside processes in the magetotail lobes and/or plasma sheet. The statistics of the nightside flow channels have been studied by Gabrielse et al. (2018) and they find that the flow channels are aligned with the large-scale background convection. They also find a postmidnight preference in the polar cap flows, which is similar to the behavior of PCAs.

Previous work involving flow channels has largely been based on data from satellite passes (e.g., Sandholt & Farrugia, 2009), where the flow channel can only be sampled once per orbit and therefore do not describe the temporal evolution of the flow channel. Although SuperDARN data have been used in the past to observe flow channels, studies have focused on either a single beam within a radar scan (Provan et al., 1999) or occasionally referenced SuperDARN global convection maps for a large-scale overview of the flow channel (Andalsvik et al., 2011). Observing a single beam within a radar scan allows for the best temporal resolution, but offers limited information about the structure of the channel. Each cell within the global convection map is a 111 km × 111 km square, which places a lower limit on the size of channels which can be detected. To give further insight into the structure and spacial/temporal evolution of flow channels, we will analyze individual, whole field-of-view (FOV) radar scans from the Longyearbyen SuperDARN radar over a period of 1 year.

The selection of a 0.9 km/s velocity magnitude threshold and the definition of a flow channel is discussed in more details in section 3 of the paper. These, along with additional applied criteria, ensure that only fast, well-defined channels embedded within a region of slower, background convection flow are identified (as shown, e.g., in Figure 1). In this paper, the focus will be on two case studies of flow channels, one on the dawn flank and another within the cusp. The properties, formation, evolution and contribution to the cross polar cap potential will be examined. A future paper will study the statistics of the detected flow channels.

2. Instrumentation

The Super Dual Auroral Network (SuperDARN) is a global network of over 30 high-frequency coherent scatter radars designed primarily for studying *F* region ionospheric plasma (Chisham et al., 2007; Greenwald et al., 1995). During the common mode of operation, each SuperDARN radar in the network

Journal of Geophysical Research: Space Physics 10.1029/2019JA026916

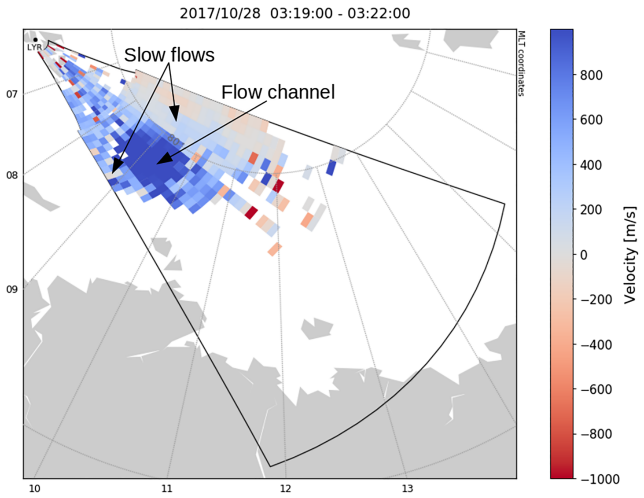

Figure 1. The field-of-view of the Longyearbyen radar in Magnetic Local Time (MLT)/Magnetic Latitude (MLat) coordinates showing the line-of-sight velocity, where blue and red represent flows toward and away from the radar, respectively. A clear channel of enhanced flow toward the radar is visibly embedded within the slower moving background flow.

steps through a series of azimuthally consecutive beams, separated by ~3° increments. Each beam is divided into 75 range gates of 45 km resolution. The radars are frequency agile (8–20 MHz) and routinely measure the line-of-sight Doppler velocity, spectral width, and backscattered power from magnetic field-aligned ionospheric irregularities. These decameter-scale irregularities drift at the bulk E × B drift velocity in the *F* region ionosphere.

In this study, we specifically used scans from the Longyearbyen SuperDARN (LYR) radar, which is located at 78.153°N, 16.074°E, 472 m altitude and began operations in October 2016. The data used were recorded in common mode in 2017 on channel A (9.8–9.9 MHz) at 1 min resolution, which is the time taken to complete a scan of all 16 beams. The LYR radar was selected as the first target of the flow channel detection algorithm as it has an ideal position at a high-latitude with a north-east facing field-of-view (shown in Figure 1), covering a large area of the polar cap and receiving a large amount of backscatter. The radar can theoretically detect backscatter up to 3,500 km in range but more regularly records data up to 1,500 km with a latitudinal range of approximately 76–82° (magnetic coordinates).

Data from SuperDARN radars can be combined to provide maps of the high-latitude ionospheric convection using the "map potential" technique (Ruohoniemi & Baker, 1998), in which the electrostatic potential pattern is determined as an expansion in spherical harmonic functions. Line-of-sight velocity measurements from all of the radars are gridded and used to determine the values of the spherical harmonic coefficients, while an IMF-driven model is used to constrain the spherical harmonic fit in areas where data coverage is sparse or absent. The model used to generate the convection maps within this study is the TS18 statistical model of ionospheric convection (Thomas & Shepherd, 2018). The electrostatic potential pattern usually reaches a maximum near dawn and a minimum near dusk. The cross polar cap potential (CPCP), a proxy for the strength of the ionospheric convection at a given time, can then be calculated as the difference between the maximum and minimum potential. All magnetic coordinates displayed within this paper are altitude adjusted corrected geomagnetic coordinates (Baker & Wing, 1989; Shepherd, 2014).

This study also uses data from the Defense Meteorological Satellite Program (DMSP). Each DMSP satellite has a 101 min polar, Sun-synchronous orbit at an altitude of 840 km. Since 2003, the DMSP satellites have housed the Special Sensor Ultraviolet Spectrographic Imager (SSUSI), with a global far ultraviolet (UV)

Journal of Geophysical Research: Space Physics 10.1029/2019JA026916

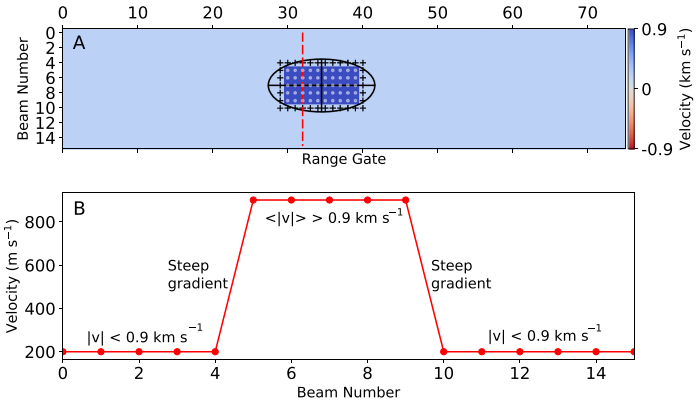

Figure 2. Plots demonstrating the analysis of a simulated flow channel. Panel (a) shows a channel of >0.9 km/s flow within slower moving (200 m/s) background flow. Positively identified cells are marked with gray dots, edge cells are marked by black crosses, and the principal component axes are marked with solid black lines and encompassed by an oval. A vertical dotted red line shows a slice through the beams at a constant range. Panel (b) shows the velocity across that slice with annotations of notable features.

imager (165–180 nm; Paxton et al., 1992). Each scan of the oval takes ~20 min, and the emissions are produced primarily due to precipitating electrons impacting the upper atmosphere. In this paper, observations in the Lyman-Birge-Hopfield Long (LBHL) wavelength range (165–180 nm) are presented to provide a global context for each event.

Optical images recorded by the Sony a7s All Sky Camera (ASC) at the Kjell Henriksen Observatory (78.148°N, 16.043°E, 520 m altitude) were also used in this study to provide a detailed view of the time evolution of the auroral emissions in the vicinity of the flow channel. The camera is located 1 km from the Longyearbyen radar and uses a fish-eye lens to capture 180° color images of the sky with a 4 s exposure time.

3. Flow Channel Detection Algorithm

The aim of the newly developed algorithm was to automatically search through the large SuperDARN data set and locate fast flowing channels embedded within a slower moving background convection. The algorithm was applied on the Longyearbyen radar to all 2017 channel A common mode data. This equated to 314 days of 1 min resolution scans and in total ~450,000 scans were used. The algorithm requires a larger amount of scatter coverage to be present within each fan plot than is typically available within a single scan. This is due to the fact that the radar relies on backscatter from electron density irregularities where the Bragg condition is satisfied and it is generally not the case that data will be obtained from every range gate along every beam. Therefore, the data set was smoothed to improve data coverage by averaging each individual cell (1 × 45 km range gate along one beam) within the FOV over three consecutive scans. Only the available data in each cell over the three scans were averaged together, so the averages in each cell were calculated from between one and three individual velocity values. From this point onward, we define a "scan" to be a grid of beams and range gates, where each "cell" contains an average velocity at that specific beam and range gate over any available velocity data within three consecutive minutes. A choice of a 3 min average for each scan maintains a high enough resolution to detect transient channels associated with reconnection.

Figure 2a shows a scan of an idealized flow channel plotted as color contours on a beam-gate grid, where the red dotted line represents a slice through the beams at a constant range. This idealized case will be used to illustrate the steps in the algorithm. If there were no fast flows within the grid, then there could be no flow channel, thus a check for velocity magnitudes above 0.9 km/s was applied to the grid. If the search yielded nothing, this grid was neglected, the start time was shifted by 1 min and a new scan was generated. If there were fast flows within the grid, it was important to determine if they contain structure or if they were actually noise and not physical. The cell containing the fast flow was then compared to the eight neighboring

Journal of Geophysical Research: Space Physics 10.1029/2019JA026916

cells, spanning across the adjacent beams and ranges. If scatter was present in all of the neighbors, every cell contained velocities of the same sign, and their average velocity exceeded 0.9 km/s, then a velocity structure is said to exist and this represents the threshold of detection of the algorithm.

Another test was required to eliminate instances where fast flows may exist but with a gradual gradient across the structure. Cases such as these are likely to be an artifact of the look direction of the radar, perhaps viewing constant flow at an angle which appears to reveal fast flows gradually transitioning to slower flows. A quantitative check of the gradient is then required and is demonstrated in Figure 2b, which shows the velocity profile over a slice across the beams at a constant range. The gradient of the velocity is calculated by taking the difference in velocity ($v2 - v1$) in a sliding window across the entire slice. The algorithm searches for two sharp gradients of opposing signs, which should be present on the edge cells of the channel at the transition points between the inside of the fast moving channel and the slower background flows. These two locations are defined as the "edge" of the channel and it is now possible to refer to the inside and outside of the channel with respect to these edges. The edge cells must be of the same sign as the inside of the channel, and there must not be any missing data within the channel. The threshold placed on the gradient is 400 m s^{-1} $cell^{-1}$, as this eliminated most of the slowly varying gradients. Additionally, the inside of the channel is examined to ensure that on average the flow magnitude is above 0.9 km/s, which allows for variation but prevents the detection of more complicated channels that are harder to analyze. There should also be no velocity values exceeding 0.9 km/s outside of the channel as this region should be the slower background flow. To ensure that the background flow exists around the channel, the points immediately outside of the edge cells along the slice are examined. If >80% of these points are present and there are >5 edge cells in total, then the FC is accepted to be embedded within a discernible background flow. Slicing only at constant range through the identified cell may also bias results to certain orientations of flow channel. To avoid this, slices are taken every 30° in a circle around the identified cell and the structure was accepted as a flow channel if any one of these slices satisfied the listed criteria of the gradient and background tests.

Another feature shown in Figure 2a is the black oval encompassing the flow channel, where the semimajor and semiminor axes (marked with black straight lines) demarcate the principal component axis of all the identified cells of the algorithm (gray dots). The principal components of the identified cells were calculated to estimate the orientation of the channel with respect to the beam direction (semimajor axis) and the width of the channel (semiminor axis). The ellipse that bounds the flow channel contains 96% of all identified cells.

While a variety of velocity magnitudes have been observed inside flow channels (e.g., Andalsvik et al., 2011, $v > 1$ km/s; Nishimura et al., 2014, $v = 0.9$ km/s; Oksavik et al., 2005, $v = 0.5$ km/s) there exists no definition as to how to define the edge of a channel. As such, we tested the detection algorithm with three different velocity gradient thresholds (400, 500, and 600 m s^{-1} $cell^{-1}$) in combination with a variety of velocity magnitude thresholds inside the channel (from 500 up to 1,000 m/s). To ensure we have fast flows we set the velocity threshold toward the higher end of the range of velocities observed in a flow channel at $v > 0.9$ km/s . Using this as a velocity threshold and given the spatial resolution of the radar data (45 km range gates along the beam), it was decided that a velocity gradient threshold of 400 m s^{-1} $cell^{-1}$ would ensure that we are indeed observing channel structures with distinct edges embedded within a slower background flow. Using this criteria, the flow surrounding the channel would then be a maximum of 45% of the flow inside the channel and this change would occur over a small spatial scale (1 cell). In addition, an examination of the actual velocity inside the identified channels using this criteria was also undertaken, which showed an average channel velocity of ~1,100 m/s with a lower limit of the full width half maximum of the distribution at 950 m/s.

Figure 3 shows four examples of detected channels, where the gray dots indicate the cells which passed all the tests. Many different sizes and orientations of flow channels were identified, and in many cases the flow channel persisted for multiple consecutive scans. To further investigate the location and duration of the flow channels, it was necessary to consider all of the positively identified cells and define a single channel center within each scan. In addition, it is required to separate all of the detections into discrete events by defining a maximum allowable time gap between scans, which if exceeded would separate one "event" from the next. An average of the beams and range gates of the positively identified cells within each scan produced the coordinates of a single location for the flow channel center.

The algorithm identified 546 events with FC centers over a range of MLT as shown in Figure 4. An event is classified as a continuous detection of a FC with no time gaps larger than 3 min. The majority of flow

Journal of Geophysical Research: Space Physics 10.1029/2019JA026916

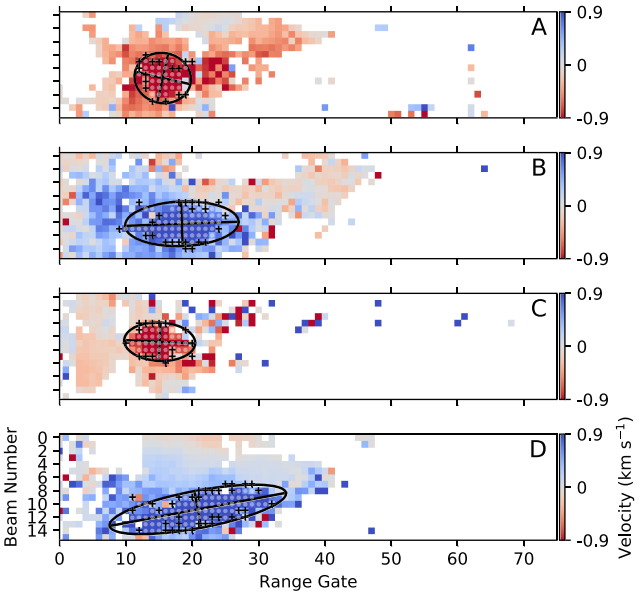

Figure 3. Four different examples of scans where flow channels were identified by the algorithm for the dates of (a) 28 February 2017 08:25 UT, (b) 26 October 2017 06:11 UT, (c) 15 April 2017 07:26 UT, and (d) 28 October 2017 04:33 UT.

channels were detected in the dayside polar cap between 9 and 14 MLT. There are also events present along the dawn and dusk edges of the polar cap and a small number of events on the nightside.

This paper will focus on the in-depth analysis of two case studies that were identified by the detection algorithm. These two case studies are indicated by the red dots within Figure 4: Case 1 on the dawn flank and Case 2 on the dayside. Case 1 was chosen to investigate flow channels occurring deep within the polar cap, as the processes behind these channels have not yet been fully explored. Case 2 was chosen as the majority of events were detected in the dayside polar cap, so taking one from this sample allows discussion of the characteristics of flow channels on newly opened field lines. This event also persisted for almost an hour, which allows a time series to be examined and for the formation, evolution, and decay of the channel to be studied. A later paper will explore the statistics of the identified FCs, including event durations, monthly occurrence, and the IMF dependencies of FC location.

4. Case Studies

4.1. Case 1: Dawn Polar Cap Flow Channel at 79° MLAT/7 MLT

The first case study focuses on an example of a flow channel occurring on the dawn flank (79° MLAT, 7 MLT), deep within the polar cap on 2 October 2017 at 01:10 UT. Figure 5 shows solar wind data from the OMNI 1 min resolution data set, which has been time-shifted to the nose of the Earth's bow shock. Overall, the characteristics of the solar wind show average values with no strong solar wind driving (B_z −0.5–2.5 nT, B_y −1–2.5 nT, density ~3.5 n/cm^3, velocity ~420 km/s, and pressure ~1.5 nPa). Figure 5 shows that during the interval of interest, there was mainly northward IMF and B_y alternated between positive and negative values. The FC duration, as detected by the algorithm, is indicated by a yellow highlighted section of the

Journal of Geophysical Research: Space Physics 10.1029/2019JA026916

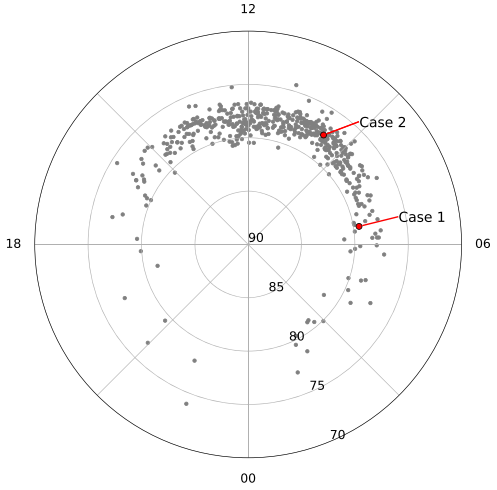

Figure 4. The gray dots show the occurrence in Magnetic Local Time (MLT)/Magnetic Latitude (MLat) coordinates of the flow channel center at the beginning of each event within the study. The two case studies have been indicated by red dots.

plot from 01:10–01:12 UT. Flow channels occurring on the dawn and dusk flanks in the polar cap fall into the FC 2 category and happen on old-open field lines, which are field lines that have been opened on the dayside 10–30 min earlier. In the case of FC 2 on the dawn flank, a positive B_y is also expected (Sandholt & Farrugia, 2012). Searching in the solar wind data for potential FC triggers that match these specifications yields the blue highlighted section between 00:45 and 00:51 UT in Figure 5. During this interval, B_z takes a small magnitude southward turning to a maximum of ~ -0.5 nT and remains negative for 6 min and B_y switches from negative to positive, dominating B_z with a value of +2 nT. The time delay between B_y and B_z and also their signs are consistent with the Sandholt and Farrugia (2009) framework for FC 2 on the dawn flank on old-open magnetic field lines.

Figure 6a is a plot of data from the SSUSI onboard the F17 DMSP satellite, showing emissions in the LBHL wavelength. On the dawn flank, the UV emissions show a thick band at 70–80° MLAT associated with the auroral oval and also a thin branch further poleward (~82° MLAT) that is aligned east-west. This feature is consistent with a PCA, specifically a bending arc. Bending arcs form under B_y-dominated conditions and in most studied cases B_z is close to zero (Carter et al., 2015; Kullen et al., 2015). They move primarily antisunward, in contrast to other PCAs that move dawnward or duskward. The arc may have been imaged on its antisunward journey across the polar cap and was observed in the dawn sector due to the positive B_y component. Figure 6b shows a SuperDARN LYR fan plot for 1:12–1:15 UT, where the FC is clearly visible as an enhanced region of antisunward flow. DMSP traversed from east to west and passed 70 MLAT on the dawnside at 01:19 UT, which means DMSP SSUSI recorded the region where the SuperDARN FOV shows the flow channel at approximately 01:12 UT, the same time as the displayed 3 min average. The FC lies in between the auroral oval and the bending arc and the flow on each side of the FC seems to slow or reverse at some ranges. The velocity shear associated with the arc is located at the poleward side of the channel. At the equatorward side, the radar begins to measure the flow reversal region associated with sunward return flow on closed field lines. The map potential plot of Figure 6c, shows a dominant dusk cell due to the positive B_y and the clear signature of the flow channel in the close ranges. Figure 6c also supports the conclusion that the FC location is antisunward of the convection throat and a comparison with Figure 6a reinforces that the auroral oval emissions are in the same location as the reversal of the convection on the equatorward edge of the FC. Unfortunately, DMSP F17 did not pass directly over the flow channel, so cross-track ion drift velocity measurements are unavailable for the interval.

To investigate the temporal evolution of the flow channel and its associated optical signatures, Figure 7 (left) shows all sky camera data from Longyearbyen plotted beside SuperDARN LYR fan plots over the interval of interest (Figure 7, right). On each ASC image, north, west, south, and east are at the top, right, bottom, and

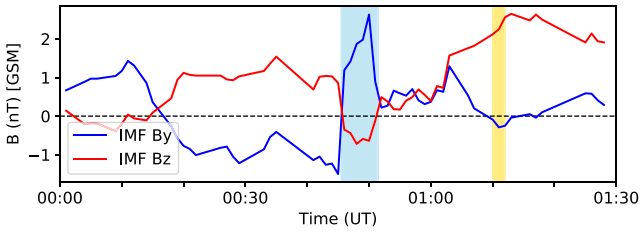

Figure 5. OMNI solar wind data time lagged to the bow shock for Case 1 on 2 October 2017 01:10 UT. The magnetic field data are in Geocentric Solar Magnetospheric (GSM) coordinates. The area highlighted in blue shows the potential solar wind trigger of the flow channel, while the yellow highlighted area marks the flow channel duration.

Journal of Geophysical Research: Space Physics 10.1029/2019JA026916

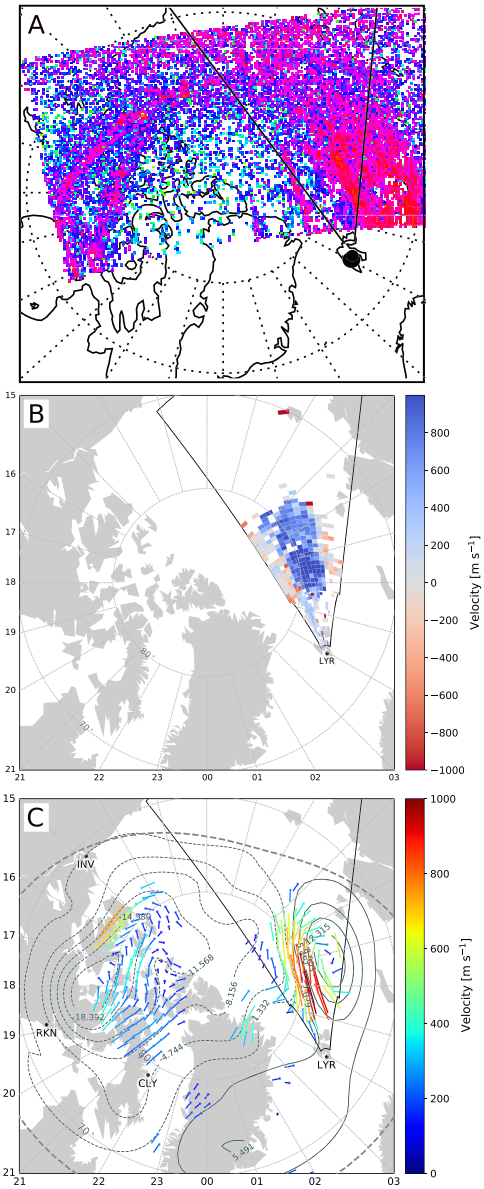

Figure 6. Plots for Case 1 on 2 October 2017 showing (a) the DMSP F17 pass recorded by the SSUSI instrument in the LBHL wavelength, crossing left to right over the period 1:09–1:19 UT, (b) the SuperDARN line-of-sight velocity scan from 1:12–1:15 UT, and (c) the SuperDARN convection map from 1:12–1:14 UT.

Journal of Geophysical Research: Space Physics 10.1029/2019JA026916

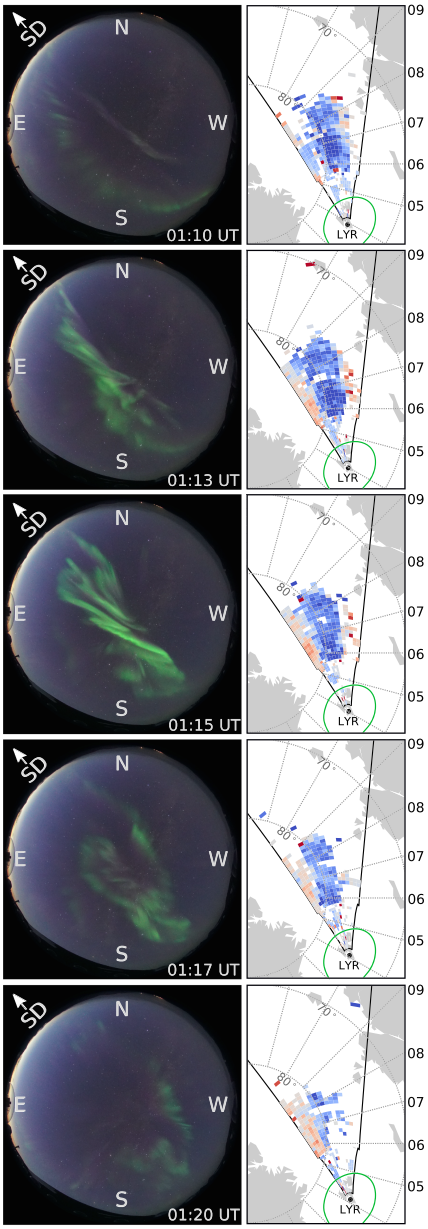

Figure 7. (Left column) The all sky camera images during the formation and decay of the flow channel with the cardinal points and look direction of the SuperDARN Longyearbyen radar. (Right column) The SuperDARN Longyearbyen fan plots at the same times as the all sky images, where the green oval shows an approximate field-of-view of the all sky camera at an assumed altitude of 125 km for the 557.7 nm emission.

Journal of Geophysical Research: Space Physics 10.1029/2019JA026916

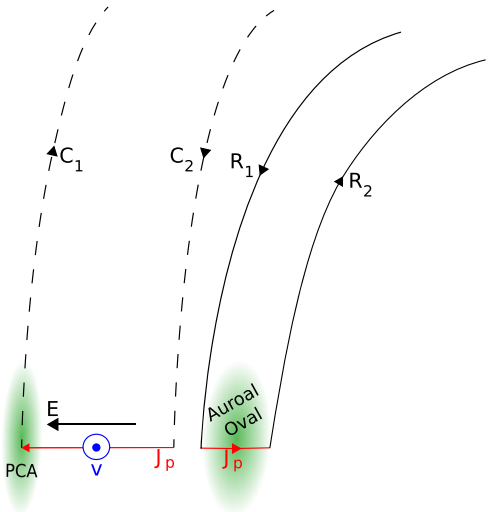

Figure 8. Schematic of the topology of the magnetic field, current systems, and ionospheric features for Case 1 on 2 October 2017. R1 and R2 are the Regions 1 and 2 Birkeland currents, C1 and C2 are the cusp current systems, and red arrows marked J_p indicated ionospheric Pedersen currents. The flow channel velocity is depicted by a blue-filled circle, and the associated electric field by a black arrow. The polar cap arc and auroral oval are shown in green highlighted areas.

left, respectively. In the first image at 01:10 UT, a stable, weak arc stretches from north-east to south-west, which has remained in place for roughly 30 min, first appearing at 00:40 UT. A second thin, faint arc formed at 1:10 UT and is visible close to this stable arc, aligned in the same direction but more directly over zenith. The arcs abruptly brighten and merge at 01:13 UT, aligning north-east to south-west. The intensification of the arcs is short-lived and begins to fade at 01:17 UT, becoming less structured and fading almost completely by 01:20 UT.

The green oval in each panel of Figure 7 (right) shows the approximate field-of-view of the all sky camera at an assumed altitude of 125 km for the 557.7 nm emission. Figure 7 (right) shows that the FC is clearly visible at 1:10 UT. This was when the detection algorithm first identified the channel. However, the three-scan average with the greatest number of detected cells, and therefore the peak intensity of the flow channel evolution, was at 01:11 UT. There are insufficient background flows for FC detection with the algorithm by the 01:13 UT scan, although the high flows associated with the FC center still persist. A manual check of the 3 min average scans reveals that the flow channel has a duration of 13 min. The FC first begins to form at 1:07 UT, peaks at approximately 1:12 UT, and then decays in speed and size until there is very little evidence of the channel by 01:20 UT. The evolution of the FC and arc are similar in duration and intensity, which could suggest that they are a coupled ionospheric response to a system driver. The FC center is (on average over the event) located at 79° MLAT, ~7 MLT. The average velocity within the FC during the period of 01:11–01:14 UT was 985 m/s and can be used alongside the magnetic field strength to estimate an electric field value of 49 mV/m. The width as calculated from the fitted ellipse was found over the event to be on average 418 km. The potential drop over the FC can then be calculated as 21 kV. As the SuperDARN map potential value of the CPCP is 35 kV at the time of the FC, this results in the FC contributing 60% of the total CPCP.

Figure 8 shows a schematic illustration of the field-aligned currents associated with the FC and PCA. On the right-hand side of the diagram are the large-scale current systems associated with the morning sector auroral oval. These currents (R1 and R2) are known as the Birkeland currents (Birkeland, 1908), which encircle the high-latitude regions of each pole in two rings (Iijima & Potemra, 1976). These current systems close via horizontal Pedersen currents, electrodynamically linking the magnetopause, the inner magnetosphere, and the ionosphere. The poleward ring (R1) flows into the ionosphere on the dawnside and out on the duskside, linking to the magnetopause current, while the polarity is reversed for R2, which maps to the partial ring current. Further poleward lie the C1-C2 cusp currents. FC 2 is the result of the closure of these currents in the ionosphere (Sandholt & Farrugia, 2009; Sandholt et al., 2006). The PCA is colocated with the upward directed C1 current. This schematic view is supported by the previously discussed flows in the fan plots shown in Figure 7 as the reversal poleward of the channel is consistent with an upward current (C1) and the auroral precipitation (PCA), while R1 is colocated with the shear between antisunward flow across the polar cap and sunward return flow on closed field lines in the dawn auroral oval.

4.2. Case 2: Extended Cusp Flow Channel 77° MLAT/10.5 MLT

The majority of the detected FCs occur on the dayside between 9 and 14 MLT (see Figure 4). Therefore, in order to examine a case representative of this sample, a period of multiple cusp FCs located on average at 10.5 MLT (between 05 and 06 UT) is analyzed in the following case study. Figure 9 shows the IMF magnetic field, density, velocity, and pressure from the OMNI data between 4:00 and 6:30 UT on 7 November 2017. The algorithm detected FCs in six intervals indicated by the yellow highlighted sections on all four panels in Figure 9. Figures 9b and 9d show that the solar wind density and pressure were very high during the entire interval, although Figure 9c shows a slower than average solar wind velocity. Figure 9a shows a discontinuity

Journal of Geophysical Research: Space Physics 10.1029/2019JA026916

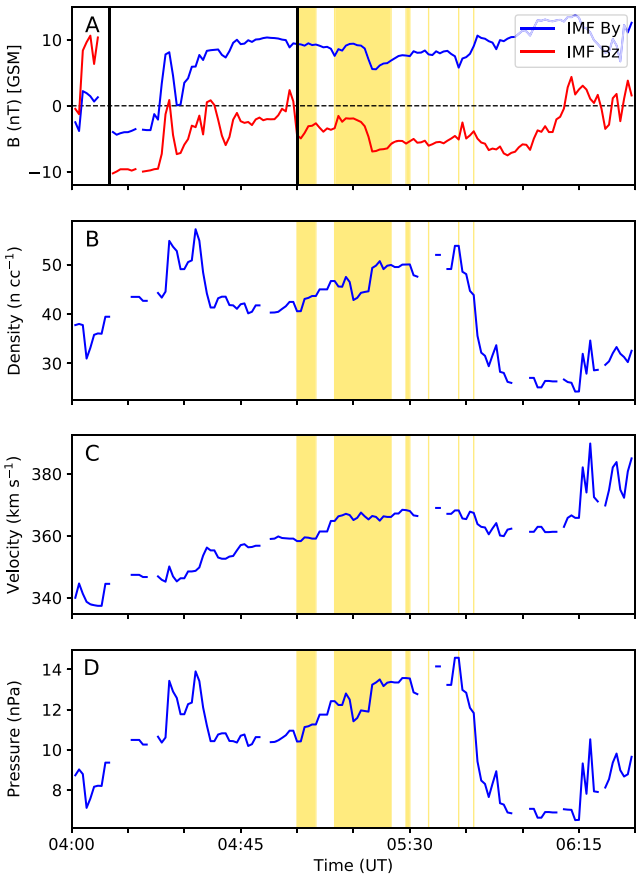

Figure 9. OMNI solar wind data time lagged to the bow shock for Case 2 on 7 November 2017 showing (a) IMF strength where the blue and red lines are the B_y and B_z components, respectively (b) density (c) velocity and (d) pressure. Yellow highlighted areas show the duration of each flow channel and the solid black lines in panel (a) mark times of interest that are elaborated on in the text.

in the solar wind magnetic field at 4:10 UT (first black vertical line), where there is a 20 nT drop in B_z to −10 nT, although there is a data gap directly before and therefore the drop could have occurred between 4:07 and 4:10 UT. At the same instance, there is a smaller drop in B_y to −4 nT. *By* 4:45 UT, B_y has gradually increased and stabilized at +10 nT. Although this period of $-B_z$ is favorable for dayside reconnection, it is probably not steady as B_z is fluctuating. At 5 UT (second black line), B_z turns and remains constantly southward, at which point FCs begin to be detected by the algorithm. Over the next hour, there is strong solar wind driving with a constant $+B_y$ of 10 nT and a steady $-B_z$ between −5 and −7 nT. At 5:45 UT, the density and pressure drop to half of the previous values, and B_z turns positive at approximately 6:15 UT.

Figure 10a shows a SuperDARN convection map where the FC was very fast and wide. The dusk cell dominates over the dawn cell, which is consistent with a positive B_y. Two regions of enhanced flows can be seen in this plot, a clear FC in the close ranges of the radar (77° MLAT, 10.5 MLT) and another area of >0.9 km/s flows postnoon (75° MLAT, 15 MLT). Figure 10d shows selected fan plots over the course of the event, which will be used in conjunction with the solar wind data to discuss the case study. Visual inspection of the fan

Journal of Geophysical Research: Space Physics 10.1029/2019JA026916

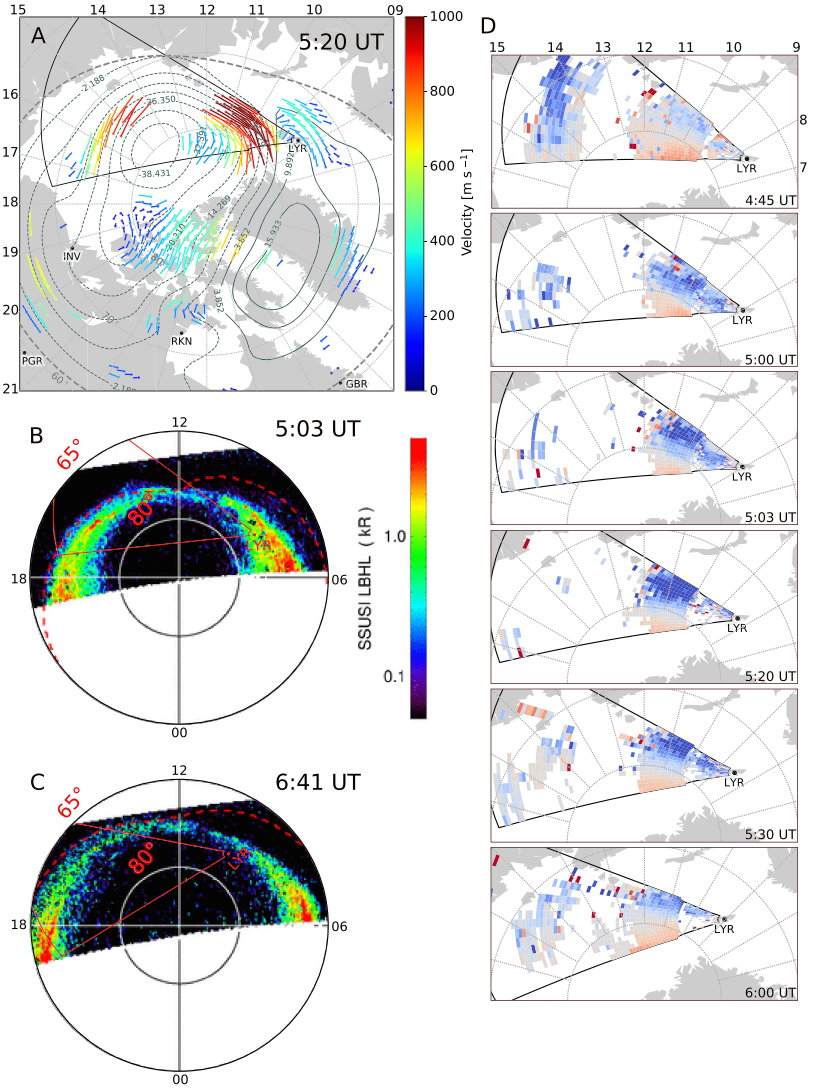

Figure 10. Panels for Case 2 on 7 November 2017 showing (a) the SuperDARN convection map with the LYR fan overlaid, the DMSP SSUSI data in the LBHL wavelength for (b) 5:03 UT and (c) 6:41 UT, and (d) fan plots of line-of-sight velocity over the duration of the event from the LYR radar.

plots in the lead up to the first successful FC detection reveals that the FC begins forming in the near range gates at 04:20 UT (not shown), a few minutes after the southward turning of B_z at ~4:10 UT. The area of enhanced flows shows structuring, but is far below the detection threshold of the algorithm. At 4:45 UT, enhanced flows are visible in the far ranges of the SuperDARN LYR fan plot. At 5:00 UT, the far range flows are no longer visible, the FC begins to gain speed and structure in the close range gates, the velocity surpasses the threshold, and the algorithm detects the FC. The FC then persists in the close ranges until 5:47 UT.

Journal of Geophysical Research: Space Physics 10.1029/2019JA026916

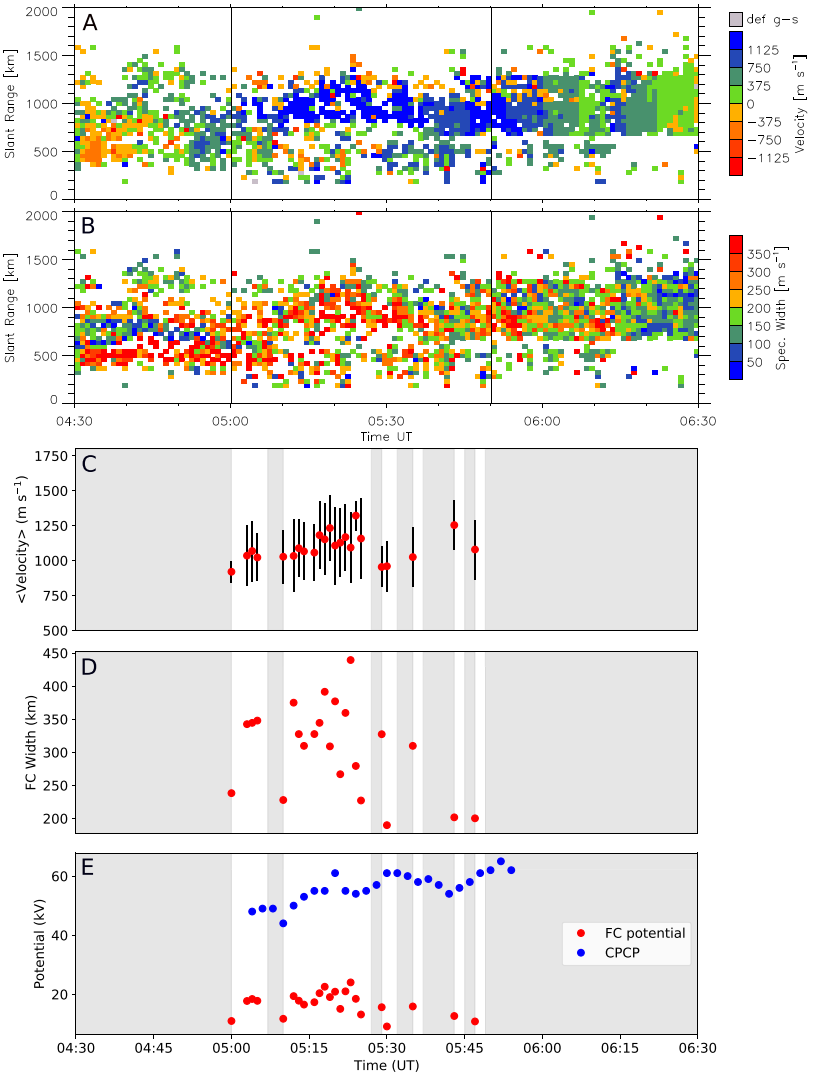

Figure 11. A time series of Case 2 on 7 November 2017. Panels (a) and (b) show range-time graphs for velocity and spectral width, respectively, for beam 13, in the center of the flow channel. (c) The average velocity of the flow channel (red points) with an error bar of 1 standard deviation. (d) The width of the flow channel, and (e) the flow channel potential (red points) and total cross polar cap potential (blue points).

Journal of Geophysical Research: Space Physics 10.1029/2019JA026916

The location of the FC within the cusp region suggests that we are observing FC 1 on newly opened field lines. The flow channel can be seen to be intermittently excited by the $-B_z$, so therefore falls under the "spontaneously driven" category. B_z remains negative and drives reconnection until 6:15 UT. So rather than the FC ceasing, the disappearance of the FC from the SuperDARN LYR FOV could be due to the reconnection site moving equatorward due to the enhanced dayside reconnection. This inference is supported by the expansion of the auroral oval observed by DMSP on two separate passes as seen in Figure 10. The pass at 5:03 UT (Figure 10b) shows that at the beginning of the interval, the dayside oval sits at ~78° MLAT, while at the next pass at 06:41 UT (Figure 10c) the oval has visibly expanded equatorward to approximately 75° MLAT, out of the range of the SuperDARN LYR radar FOV.

Figure 11 shows a time series over the course of the event, beginning 1.5 hr before the algorithm detected the FC and ending 45 min after the last detection. Panels (a) and (b) show range-time plots for beam 13, color coded by velocity and spectral width, respectively. Beam 13 was at the center of the FC, so it is ideal for studying its formation and evolution. The vertical black lines mark the first and last detection times of the algorithm during this interval. Figure 11a shows that the algorithm detected the majority of the event effectively as the highest velocity flows begin and end close to the black vertical lines. Figure 11b shows a high spectral width of up to 400 m/s inside the channel, suggesting turbulent flows. There is an apparent pulsing present in both the velocity and spectral width measurements between 5:00 and 5:35 UT, where the channel periodically moves from 800–1,200 km slant range. Figure 11c shows an average velocity (red points) at times where the algorithm detected a FC, with an error bar of 1 standard deviation to indicate the spread of velocities inside the channel. Values lower than the velocity threshold are present in the velocity spread. This is because the velocity threshold is applied to the average velocity around a cell and between the edges of the channel. This allows for significant variation in the FC at times, but the average velocity always remains above the threshold of 0.9 km/s. Figure 11c shows that the average velocity generally increases until 5:24 UT from values of 900 to 1,300 m/s. After this point there are too few points to determine a trend. Figure 11d shows a large variation in the FC width over the interval from 190–440 km, which classifies the flow channel as a mesoscale feature. Figure 11e shows the FC potential (red points) and the cross polar cap potential (blue points). The FC potential is 30% of the total cross polar cap potential on average and 46% at the peak of the event (5:23 UT). The values in Figures 11c–11e are derived from the algorithm outputs (apart from the CPCP, which is a SuperDARN data product) and the grayed-out regions on these panels indicate periods when no FCs were detected by the algorithm.

5. Discussion

The newly developed algorithm described in this paper identifies structured fast flows (over 0.9 km/s) within the polar cap. These flows are embedded within a slower background convection flow, with a velocity gradient of at least 400 m s^{-1} $cell^{-1}$ on either side of the flow channel. Our algorithm is the first automated method for detecting FCs in SuperDARN data over all MLTs within the polar cap. The algorithm identified 546 events in the Longyearbyen radar data during 2017. The stringent criteria applied with the algorithm ensures that only well-defined, fast flow channels were identified, which are moving in the same direction as the background convection. The algorithm was most effective in detecting the FCs at their peak, at the time of highest flow velocity due to the high-velocity selection criteria. Both short and long duration events were identified at a range of MLTs. Detected FCs should be located in the polar cap in a statistical sense, as the most poleward section of the open-closed field line boundary (dayside cusp region) is statistically located at 75° latitude (Yeoman et al., 2002) and the SuperDARN LYR radar measures a further poleward latitudinal range of approximately 76–82°.

Two case studies were chosen for further investigation: Case 1 on the dawn flank and Case 2 in the cusp region. The Case Study 1 event was chosen for further discussion as relatively little is known about flow channels occurring deep within the polar cap on field lines which have been opened 10–30 min previously. Case Study 2 was chosen as the vast majority of the detected events within the Longyearbyen radar FOV occurred on the dayside. The event was interesting as it allowed discussion of a dayside event (which make up the majority of our sample) but was also chosen as it was roughly an hour in duration. This allows a meaningful time series to be examined and for the formation, evolution, and decay of the channel to be discussed. In both case studies, DMSP observations place the auroral oval equatorward of the FC observations, confirming that the FCs occur within the polar cap.

Journal of Geophysical Research: Space Physics 10.1029/2019JA026916

5.1. Key Properties of the Flow Channels

Case Study 1 on 2 October 2017 shows a short-lived flow channel, lasting 13 min by eye and detected by the algorithm for 2 min, occurring on the dawn flank. The average velocity of the flow channel was 985 m/s with an average width of 418 km. This yields an electric field value and potential drop across the FC of 49 mV/m and 21 kV, respectively.

Case Study 2 on 7 November 2017 is an example of a longer-lived flow channel in the cusp, lasting for approximately 1 hr. The FC had an average speed of 1.1 km/s, an electric field value of 55 mV/m, and an average width of 307 km. The spectral width measurements inside the channel show high values of 400 m/s, suggesting turbulent flows. The average potential across the channel is 17 kV with a peak of 25 kV.

5.2. The Contribution of Flow Channels to the Cross Polar Cap Potential

At their peak values, the flow channels accounted for 60% and 46% of the CPCP in Cases 1 and 2, respectively. These are higher percentages than previously observed for FC 2, for example, Andalsvik et al. (2011) (35%) and Sandholt et al. (2010) (25%). Our algorithm gives a more accurate estimate as both previously published values were observed using DMSP passes, which only give measurements over the satellite trajectory at a given instance. Our algorithm evaluates the FC in two dimensions (range and beam), sampling the radar FOV at a 1 min resolution. This allows continuous observation of the channel for as long as it remains within the radar FOV and sufficient backscatter is present. It is therefore possible to observe the FC over time and obtain average values of the potential. Also, this study does not limit the data to extreme IMF conditions, such as the interplanetary coronal mass ejections typically used by Andalsvik et al. (2011) and Sandholt et al. (2010). Case 1 shows that FCs are occurring for more average values of IMF and an unremarkable, small magnitude magnetic field can still generate FCs which account for 60% of the CPCP. FCs have high velocities and potentials but are small in geographic area, and will not reproduce as well as large-scale features in convection map contours. This is due to filtering by the finite spherical harmonic expansion and due to the influence from the map potential model. Identifying FCs in the data from the individual radars is therefore essential to detecting the smaller-scale FCs, and the LYR radar is in an optimal position for the detection of polar cap FCs. As polar cap FCs can account for such a significant fraction of the CPCP, it is important to have radar coverage in the polar cap in order to obtain realistic values of the CPCP. Without the polar cap radars, the CPCP would likely be severely underestimated.

In both cases, IMF B_y is the dominant IMF component. Under these conditions, a magnetic tension within the dawn-dusk direction is applied to the newly opened magnetic field lines. The entire convection pattern reconfigures on a scale of minutes with a dominant dusk/dawn cell for positive/negative IMF B_y in the Northern Hemisphere (Grocott & Milan, 2014). Reconnection with a B_y component then introduces asymmetric loading of magnetic flux into the magnetospheric lobes. As FC comprise a large fraction of the total CPCP, they are efficient at transmitting this asymmetric loading into the ionospheric convection pattern. This asymmetry can then be reduced when tail reconnection occurs, for example, during substorms, and the magnetospheric lobes are asymmetrically unloaded (Ohma et al., 2018; Reistad et al., 2018).

5.3. Flow Channel Formation and Decay Processes

The algorithm works well at picking up the peak of the FC but does not detect the formation and decay when the velocities are below the detection threshold. The case studies were manually inspected after detection to give insight into the formation and decay processes of the FC. The FC in Case 1 is linked to a PCA, which is likely a bending arc due to the preceding solar wind conditions. The optical emissions potentially associated with the arc and FC are observed in the KHO ASC, aligned in the direction of the SD FOV. Due to a lack of overlapping fields of view between the instruments used in this case study and the different observation parameters (wavelengths and scale sizes), it is not possible to conclusively link the bending arc to the auroral features seen in the ASC. However, the features could be an ionospheric response caused by the same magnetospheric driver due to their similar orientation, duration, and modulation of intensity. These observations support previous work which find FCs occurring on the edges of PCAs (Gabrielse et al., 2018; Zou et al., 2015b).

Case 2 shows a FC intermittently excited around the cusp region, strongly driven by a dense, high-pressure IMF, high magnitudes of $+B_y$ and a sustained $-B_y$. The $-B_z$ persists for over an hour and the FCs are on newly opened field lines, which makes Case 2 a spontaneously driven FC 1 in the Sandholt framework (Sandholt et al., 2010). There are signs of the structure of the FC forming approximately half an hour before the algorithm detects the FC. The velocity however shows a rapid onset in the beam directed along the center

Journal of Geophysical Research: Space Physics 10.1029/2019JA026916

of the FC, where speeds jump above the 0.9 km/s threshold and the FC emerges rapidly from the slower flow. Figure 11a shows possible pulsing of the velocity (5:00–5:35 UT) as the channel appears to move slightly between 800 and 1,200 km in slant range. This is expected from dayside reconnection phenomena, such as PIFs (Provan et al., 1998), but will not be further analyzed as it is outside the scope of this paper. After this period, the FC seems to stabilize in position from 5:35–6:00 UT and remain at 700–1,100 km slant range. Over the lifetime of the FC, there are high spectral widths of 400 m/s, suggesting turbulent flows within the channel, which could be structuring at smaller scales than one SuperDARN range gate (45 km).

5.4. Momentum Transfer on Old Open Flux

The FC in Case 1, residing on the dawn flank, was 418 km in width, lasted for 13 min (detected by the algorithm at its peak for 2 min) and was detected 25 min after a small deviation from northward to southward IMF initiated a reconnection burst with a dominant IMF B_y positive component. This width, duration, and delay time indicate a directly driven FC 2 category on old open flux within the Sandholt and Farrugia (2009) framework. Despite small IMF magnitudes, fast flows are driven deep inside the polar cap, accounting for 60% of the CPCP. The FC is observed between a thin, poleward band of emissions and equatorward auroral oval emissions in the DMSP SSUSI data. Due to the B_y dominant conditions and as B_z is close to zero, the band of emissions most likely falls into the bending arc subclass of PCAs (Carter et al., 2015; Kullen et al., 2015). Bending arcs are located on open field lines (Carter et al., 2015), which further supports the theory that the flow channel is occurring on old open field lines on the dawn flank, deep within the polar cap. This work builds upon the work of Sandholt and Farrugia (2009), using a similar velocity threshold (0.9 km/s) as compared to the 1 km/s velocity threshold of Andalsvik et al. (2011). For the first time, FC 2 is found in conjunction with a PCA (specifically, a bending arc) on the dawn flank through combined observations from DMSP, SuperDARN LYR fan plots, and SuperDARN convection maps.

6. Conclusions

A new algorithm was developed to locate flow channels within the polar cap. The algorithm detected 546 events over a years' worth of data (2017) from the Longyearbyen SuperDARN radar. Two case studies were selected for further analysis: Case 1 on the dawn flank and Case 2 in the cusp. The main findings from these case studies can be summarized as follows:

- The algorithm identified 546 events within the 1 year interval. FCs were observed in the polar cap over most magnetic local times, but the vast majority were detected in the dayside polar cap.
- The FCs comprise high values of the CPCP, peaking at 60% and 46% for Cases 1 and 2, respectively. Thus, polar cap FCs play an important role in flux transfer through the solar wind-magnetosphere-ionosphere system.
- Case 1 confirms that FCs do occur on the edge of PCAs and that fast ionospheric flows can form deep inside the polar cap under small magnitude IMF fields that are B_y dominant.
- Case 2 shows that fast flows can be driven in the cusp for extended periods with a negative B_z component of the IMF and a high magnitude positive IMF B_y. The flow inside these channels is turbulent, exhibiting higher spectral widths for faster flows, which suggests structuring at spatial scales less than one SuperDARN range gate (45 km).

The two case studies provide confidence in the ability of the algorithm to identify FCs in the polar cap. A future publication will detail the findings of a statistical study using all 546 identified events.

Acknowledgments
We would like to thank Steve Milan, Jenny Carter, Jade Reidy, and the members of the Birkeland Centre for Space Science for useful science discussions. Financial support was provided by the Research Council of Norway under Contract 223252. Solar wind and IMF data are available at the Goddard Space Flight Center Space Physics Data Facility (https://cdaweb.sci.gsfc.nasa.gov/index.html/). SuperDARN data were obtained through the SuperDARN website at Virginia Polytechnic Institute and State University (http://vt.superdarn.org/). DMSP SSUSI data are freely available at Johns Hopkins Applied Physics Laboratory (https://ssusi.jhuapl.edu/). We thank Larry Paxton (PI of the DMSP SSUSI instrument) and Dag Lorentzen (PI of SuperDARN Longyearbyen) for use of the data. Quick look all sky camera data from the Kjell Henriksen Observatory are available online (http://kho.unis.no/) and the individual all sky camera images used in this paper are available online (https://figshare.com/articles/All_Sky_Camera_Images_Svalbard_2_2017/9971246) and were obtained from the instrument PI Dag Lorentzen (dag.lorentzen@unis.no).

References

Andalsvik, Y. L., Sandholt, P. E., & Farrugia, C. J. (2011). Dayside and nightside contributions to cross-polar cap potential variations: The 20 March 2001 ICME case. *Annales Geophysicae*, *29*(11), 2189–2201. https://doi.org/10.5194/angeo-29-2189-2011

Baker, K. B., & Wing, S. (1989). A new magnetic coordinate system for conjugate studies at high latitudes. *Journal of Geophysical Research*, *94*(A7), 9139. https://doi.org/10.1029/JA094iA07p09139

Birkeland, K. (1908). The Norwegian aurora polaris expedition 1902–1903.

Carter, J. A., Milan, S. E., Fear, R. C., Kullen, A., & Hairston, M. R. (2015). Dayside reconnection under interplanetary magnetic field B_y-dominated conditions: The formation and movement of bending arcs. *Journal of Geophysical Research: Space Physics*, *120*, 2967–2978. https://doi.org/10.1002/2014JA020809

Chisham, G., Lester, M., Milan, S. E., Freeman, M. P., Bristow, W. A., Grocott, A., et al. (2007). A decade of the Super Dual Auroral Radar Network (SuperDARN): Scientific achievements, new techniques and future directions. *Surveys in Geophysics*, *28*(1), 33–109. https://doi.org/10.1007/s10712-007-9017-8

Journal of Geophysical Research: Space Physics 10.1029/2019JA026916

Denig, W. F., Burke, W. J., Maynard, N. C., Rich, F. J., Jacobsen, B., Sandholt, P. E., et al. (1993). Ionospheric signatures of dayside magnetopause transients: A case study using satellite and ground measurements. *Journal of Geophysical Research*, *98*, 5969–5980. https://doi.org/10.1029/92JA01541

Farrugia, C. J., Sandholt, P. E., Maynard, N. C., Torbert, R. B., & Ober, D. M. (2003). Temporal variations in a four-sheet field-aligned current system and associated aurorae as observed during a polar-ground magnetic conjunction in the midmorning sector. *Journal of Geophysical Research*, *108*(A6), 1230. https://doi.org/10.1029/2002JA009619

Gabrielse, C., Nishimura, Y., Lyons, L., Gallardo-Lacourt, B., Deng, Y., & Donovan, E. (2018). Statistical properties of mesoscale plasma flows in the nightside high-latitude ionosphere. *Journal of Geophysical Research: Space Physics*, *123*, 6798–6820. https://doi.org/10.1029/2018JA025440

Greenwald, R. A., Baker, K. B., Dudeney, J. R., Pinnock, M., Jones, T. B., Thomas, E. C., et al. (1995). DARN/SuperDARN. *Space Science Reviews*, *71*(1-4), 761–796. https://doi.org/10.1007/BF00751350

Grocott, A., & Milan, S. E. (2014). The influence of IMF clock angle timescales on the morphology of ionospheric convection. *Journal of Geophysical Research: Space Physics*, *119*, 5861–5876. https://doi.org/10.1002/2014JA020136

Haerendel, G., Paschmann, G., Sckopke, N., Rosenbauer, H., & Hedgecock, P. C. (1978). The frontside boundary layer of the magnetosphere and the problem of reconnection. *Journal of Geophysical Research*, *83*, 3195–3216. https://doi.org/10.1029/JA083iA07p03195

Iijima, T., & Potemra, T. A. (1976). The amplitude distribution of field-aligned currents at northern high latitudes observed by Triad. *Journal of Geophysical Research*, *81*, 2165–2174. https://doi.org/10.1029/JA081i013p02165

Kullen, A., Fear, R. C., Milan, S. E., Carter, J. A., & Karlsson, T. (2015). The statistical difference between bending arcs and regular polar arcs. *Journal of Geophysical Research: Space Physics*, *120*, 10,443–10,465. https://doi.org/10.1002/2015JA021298

MacDougall, J. W., & Jayachandran, P. T. (2001). Polar cap convection relationships with solar wind. *Radio Science*, *36*, 1869–1880. https://doi.org/10.1029/2001RS001007

McWilliams, K. A., Yeoman, T. K., & Provan, G. (2000). A statistical survey of dayside pulsed ionospheric flows as seen by the CUTLASS Finland HF radar. *Annales Geophysicae*, *18*(4), 445–453. https://doi.org/10.1007/s00585-000-0445-8

Milan, S. E., Lester, M., Cowley, S. W. H., & Brittnacher, M. (2000). Convection and auroral response to a southward turning of the IMF: Polar UVI, CUTLASS, and IMAGE signatures of transient magnetic flux transfer at the magnetopause. *Journal of Geophysical Research*, *105*, 15,741–15,755. https://doi.org/10.1029/2000JA900022

Milan, S. E., Lester, M., Cowley, S. W. H., Moen, J., Sandholt, P. E., & Owen, C. J. (1999). Meridian-scanning photometer, coherent HF radar, and magnetometer observations of the cusp: A case study. *Annales Geophysicae*, *17*(2), 159–172. https://doi.org/10.1007/s00585-999-0159-5

Neudegg, D. A., Cowley, S. W., Milan, S. E., Yeoman, T. K., Lester, M., Provan, G., et al. (2000). A survey of magnetopause FTEs and associated flow bursts in the polar ionosphere. *Annales Geophysicae*, *18*(4), 416–435. https://doi.org/10.1007/s00585-000-0416-0

Nishimura, Y., Lyons, L. R., Zou, Y., Oksavik, K., Moen, J. I., Clausen, L. B., et al. (2014). Day-night coupling by a localized flow channel visualized by polar cap patch propagation. *Geophysical Research Letters*, *41*, 3701–3709. https://doi.org/10.1002/2014GL060301

Ohma, A., Østgaard, N., Reistad, J. P., Tenfjord, P., Laundal, K. M., Snekvik, K., et al. (2018). Evolution of asymmetrically displaced footpoints during substorms. *Journal of Geophysical Research: Space Physics*, *123*, 10,060–10,063. https://doi.org/10.1029/2018JA025869

Oksavik, K., Moen, J., Carlson, H. C., Greenwald, R. A., Milan, S. E., Lester, M., et al. (2005). Multi-instrument mapping of the small-scale flow dynamics related to a cusp auroral transient. *Annales Geophysicae*, *23*(7), 2657–2670. https://doi.org/10.5194/angeo-23-2657-2005

Paxton, L. J., Meng, C.-I., Fountain, G. H., Ogorzalek, B. S., Darlington, E. H., Gary, S. A., et al. (1992). Special sensor ultraviolet spectrographic imager: An instrument description. *Proc. SPIE 1745, Instrumentation for Planetary and Terrestrial Atmospheric Remote Sensing* (Vol. 1745, pp. 2–15). https://doi.org/10.1117/12.60595

Pinnock, M., Rodger, A. S., Dudeney, J. R., Baker, K. B., Newell, P. T., Greenwald, R. A., & Greenspan, M. E. (1993). Observations of an enhanced convection channel in the cusp ionosphere. *Journal of Geophysical Research*, *98*, 3767–3776. https://doi.org/10.1029/92JA01382

Provan, G., Yeoman, T. K., & Cowley, S. W. H. (1999). The influence of the IMF B_y component on the location of pulsed flows in the dayside ionosphere observed by an HF radar. *Geophysical Research Letters*, *26*, 521–524. https://doi.org/10.1029/1999GL900009

Provan, G., Yeoman, T. K., & Milan, S. E. (1998). CUTLASS Finland radar observations of the ionospheric signatures of flux transfer events and the resulting plasma flows. *Annales Geophysicae*, *16*(11), 1411–1422. https://doi.org/10.1007/s00585-998-1411-0

Reistad, J. P., Østgaard, N., Laundal, K. M., Ohma, A., Snekvik, K., Tenfjord, P., et al. (2018). Observations of asymmetries in ionospheric return flow during different levels of geomagnetic activity. *Journal of Geophysical Research: Space Physics*, *123*, 4638–4651. https://doi.org/10.1029/2017JA025051

Ruohoniemi, J. M., & Baker, K. B. (1998). Large-scale imaging of high-latitude convection with Super Dual Auroral Radar Network HF radar observations. *Journal of Geophysical Research*, *103*, 20,797–20,811. https://doi.org/10.1029/98JA01288

Russell, C., & Elphic, R. (1978). Initial ISEE magnetometer results: Magnetopause observations. *Space Science Reviews*, *22*(6), 681–715. https://doi.org/10.1007/BF00212619

Russell, C. T., & Elphic, R. C. (1979). ISEE observations of flux transfer events at the dayside magnetopause. *Geophysical Research Letters*, *6*, 33–36. https://doi.org/10.1029/GL006i001p00033

Sandholt, P. E., Andalsvik, Y., & Farrugia, C. J. (2010). Polar cap flow channel events: Spontaneous and driven responses. *Annales Geophysicae*, *28*(11), 2015–2025. https://doi.org/10.5194/angeo-28-2015-2010

Sandholt, P. E., Dyrland, M., & Farrugia, C. J. (2006). Dayside aurorae and polar arcs under south-east IMF orientation. *Annales Geophysicae*, *24*(12), 3421–3432. https://doi.org/10.5194/angeo-24-3421-2006

Sandholt, P. E., & Farrugia, C. J. (2009). Plasma flow channels at the dawn/dusk polar cap boundaries: Momentum transfer on old open field lines and the roles of IMF B_y and conductivity gradients. *Annales Geophysicae*, *27*(4), 1527–1554. https://doi.org/10.5194/angeo-27-1527-2009

Sandholt, P. E., & Farrugia, C. J. (2012). Plasma flows, Birkeland currents and auroral forms in relation to the Svalgaard-Mansurov effect. *Annales Geophysicae*, *30*(5), 817–830. https://doi.org/10.5194/angeo-30-817-2012

Sandholt, P. E., Lockwood, M., Oguti, T., Cowley, S. W. H., Freeman, K. S. C., Lybekk, B., et al. (1990). Midday auroral breakup events and related energy and momentum transfer from the magnetosheath. *Journal of Geophysical Research*, *95*, 1039. https://doi.org/10.1029/JA095iA02p01039

Sandholt, P., Moen, J., Opsvik, D., Denig, W., & Burke, W. (1993). Auroral event sequence at the dayside polar cap boundary: Signature of time-varying solar wind-magnetosphere-ionosphere coupling. *Advances in Space Research*, *13*(4), 7–15. https://doi.org/10.1016/0273-1177(93)90305-U

Shepherd, S. G. (2014). Altitude-adjusted corrected geomagnetic coordinates: Definition and functional approximations. *Journal of Geophysical Research: Space Physics*, *119*, 7501–7521. https://doi.org/10.1002/2014JA020264

Journal of Geophysical Research: Space Physics 10.1029/2019JA026916

Thomas, E. G., & Shepherd, S. G. (2018). Statistical patterns of ionospheric convection derived from mid-latitude, high-latitude, and polar SuperDARN HF radar observations. *Journal of Geophysical Research: Space Physics*, *123*, 3196–3216. https://doi.org/10.1002/2018JA025280

Thorolfsson, A., Cerisier, J.-C., Lockwood, M., Sandholt, P. E., Senior, C., & Lester, M. (2000). Simultaneous optical and radar signatures of poleward-moving auroral forms. *Annales Geophysicae*, *18*(9), 1054–1066. https://doi.org/10.1007/s00585-000-1054-2

Yeoman, T. K., Hanlon, P. G., & McWilliams, K. A. (2002). Letter to the Editor: A statistical study of the location and motion of the HF radar cusp. *Annales Geophysicae*, *20*(2), 275–280. https://doi.org/10.5194/angeo-20-275-2002

Zou, Y., Nishimura, Y., Lyons, L. R., Donovan, E. F., Shiokawa, K., Ruohoniemi, J. M., et al. (2015a). Polar cap precursor of nightside auroral oval intensifications using polar cap arcs. *Journal of Geophysical Research: Space Physics*, *120*, 10,698–10,711. https://doi.org/10.1002/2015JA021816

Zou, Y., Nishimura, Y., Lyons, L. R., Shiokawa, K., Donovan, E. F., Ruohoniemi, J. M., et al. (2015b). Localized polar cap flow enhancement tracing using airglow patches: Statistical properties, IMF dependence, and contribution to polar cap convection. *Journal of Geophysical Research: Space Physics*, 4064–4078. https://doi.org/10.1002/2014JA020946

Paper II

A Statistical Study of Polar Cap Flow Channels and their IMF By dependence

K. Herlingshaw, L. J. Baddeley, K. Oksavik, D. A. Lorentzen

Journal of Geophysical Research, Vol. 125, doi:10.1029/2020JA028359 (2020)

A Statistical Study of Polar Cap Flow Channels and their IMF By dependence

K. Herlingshaw[1,2], L. J. Baddeley[1,2], K. Oksavik[1,2], D. A. Lorentzen[1,2]

[1]Department of Arctic Geophysics, University Centre in Svalbard, Longyearbyen, Norway
[2]Birkeland Centre for Space Science, University of Bergen, Bergen, Norway

Key Points:

- We present the statistics of flow channels in the dayside polar cap area including: duration, width, peak velocity, and monthly occurrence.
- Their formation is intimately related to IMF By, and the flow channels shift dawnward/duskward for +By/-By.
- Higher velocity flows in the polar cap concentrate into localized, narrower channels.

Corresponding author: Katie Herlingshaw, katie.herlingshaw@unis.no

Abstract
An algorithm to detect high-speed ionospheric flow channels (FCs) in the polar cap was applied to data from the Longyearbyen radar of the Super Dual Auroral Radar Network. The Longyearbyen radar is at high-latitude (78.2°N, 16.0°E geographic coordinates) and points North-East, therefore is in an ideal position for measuring zonal flows in the polar cap. The algorithm detected 998 events in the dayside polar cap region over 2 years of observations. The detected flow channels typically were between 200-300 km latitudinal width, 1.1-1.3 km/s peak velocity, and 3 minutes in duration. The flow channel location shows an IMF By dependency, moving dawnwards/duskwards for a +By/-By. The flow channel monthly occurrence shows a bimodal distribution with peaks around the spring and autumn equinoxes, likely due to increased coupling between the solar wind-magnetosphere-ionosphere system at these times. The highest peak velocities shows an absence of broad FC widths, suggesting that as the flow speed increases in the polar cap, the channels become more localized and narrow.

1 Introduction

The shape and flow strength of the large scale high-latitude plasma convection is strongly governed by the interplanetary magnetic field (IMF) (Cowley & Lockwood, 1992). Under southward IMF, magnetic reconnection occurs at the dayside subsolar point due to the merging of antiparallel magnetic fields. This reconnection drives antisunward flows across the polar cap and reconnection in the Earth's magnetotail drives sunward return flows at lower, sub-auroral latitudes (Dungey, 1961). Dayside reconnection is the dominant mechanism by which energy and momentum are transferred from the solar wind to the Earth's magnetosphere and ionosphere (Pinnock et al., 1993). In the ionosphere, the resultant motion due to dayside and nightside reconnection under IMF Bz- conditions is visualised as a twin cell ionospheric convection pattern. Statistical convection models have been developed to predict the convention pattern using a variety of techniques and observations, including satellite measurements (Heelis, 1984; Heppner & Maynard, 1987) and incoherent scatter radars (Cousins & Shepherd, 2010; Pettigrew et al., 2010; Ruohoniemi & Greenwald, 2005, 1996; Thomas & Shepherd, 2018). For IMF By dominant conditions, the reconnection location at the magnetopause boundary is shifted to earlier or later MLT locations. The twin cell pattern becomes twisted, forming a dominant round cell extending over the majority of the polar cap adjacent to a thin, crescent-shaped cell. The orientation of the IMF By-component determines the location of each of the cells. For IMF By+ the larger, dominant cell lies on the dusk side of the polar cap and the crescent cell on the dawn side of the polar cap. The dayside convection throat and cusp are shifted postnoon and the tension imposed on the field lines leads ionospheric flows with an westward component. For IMF By-, the orientation of the cells is reversed, the dayside convection throat and cusp are shifted prenoon, and the ionospheric flows have an eastward component.

Plasma is transported across the polar cap along the streamlines of the convection pattern at typical speeds of several hundred meters per second (MacDougall & Jayachandran, 2001; Oksavik et al., 2010). Within the dayside cusp region, flows of enhanced velocities ($\sim$ >1 km/s) have been observed and named differently depending on the parameter in which they were identified. These phenomena include flow channels/bursts, pulsed ionospheric flows (PIFs), poleward moving auroral forms (PMAFs) and poleward moving auroral radar forms (PMRAFs) (see Davies et al. (2002)). These signatures are all related and are the ionospheric manifestation of reconnection at the dayside magnetopause and flux transfer events (Haerendel et al., 1978; Russell & Elphic, 1978; Russell & Elphic, 1979; Oksavik et al., 2004). When dayside reconnection occurs, flow channels are thought to be an important feature for the injection of corotating plasma from the subauroral plasma reservoir into transpolar flow (H. Carlson et al., 2006), and in the structuring of plasma within polar cap patches in their early formation stages (H. C. Carlson, 2012). Dayside flow channels have also been found to be collocated with airglow patches, forming under By-dominated dayside reconnection and potentially transporting the airglow patches across the polar cap and into the nightside auroral zone (Hosokawa et al., 2019; Nishimura et al., 2014). Flow channels have been observed deep within the polar cap on the dawn/dusk flanks and on the nightside due to magnetotail reconnection and substorms (Sandholt & Farrugia, 2009; Nishimura et al., 2010; Oksavik et al., 2010).

In this study, we are concerned with the flow channels in the dayside cusp region, coupling strongly with the solar wind. Flow channels of this kind were first observed by the PACE HF radar by Pinnock et al. (1993) and named flow channel events. Flow channel events were consistent with the magnetic tension force on newly opened field lines and created longitudinally extended fast flows. Provan et al. (1999) further researched these events and found them to be quasi-periodic, terming them pulsed ionospheric flows (PIFs). They observed PIFs within data from the Super Dual Auroral Network (SuperDARN) and found that they occurred between 0250 and 1650 MLT with a peak between 0900-1210 MLT, 76-82 MLAT and a typical recurrence rate of 7-8 mins. They also observed an IMF By dependence on the location and frequency of the PIFs, with the location of the PIFs shifting postnoon/prenoon for positive/negative IMF By. Rinne et al. (2010, 2011) observed a series of flow channels moving with the ionospheric convection into the polar cap. The zonal flow direction in these events aligned with the tension applied by the IMF By component, which sharply changed direction multiple times during the observations. Each flow channel propagated polewards, remaining separated from the neighbouring channels with flow directions consistent with the tension applied by IMF By polarity changes. These observations support the view that a flow channel is formed near the polar cap boundary during dayside reconnection and that these flow channels will remain separate and push each other into the polar cap while the magnetic tension force and its associated field aligned current system is maintained (Lockwood et al., 2001; Moen et al., 2013).

Flow channels can be divided into four categories based on the location of the magnetic field line within the Dungey (1961) convection cycle (Sandholt & Farrugia, 2009; Sandholt et al., 2010; Andalsvik et al., 2011). The categories of the flow channels excited by the magnetic field lines at different stages are as follows: newly open field lines (FC 1), old open field lines (FC 2), and field lines connected to the tail lobes (FC 3), and field lines connected to the plasma sheet (FC 4). The focus for this paper is on dayside flow channels, so will concern FC 1 and FC 2. FC 1 and FC 2 both occur on open field lines and flow antisunward, but are distinguished by the amount of time that has passed since the driving dayside reconnection happened. FC 1 occur on newly open field lines (less than 10 minutes since reconnection), are associated with PIFs and the early stages of PMAFs/PMARFs, and are characterized by noonward convections in the prenoon and postnoon sectors. FC 2 occur on old open field lines (10-20 minutes since magnetopause reconnection) embedded in polar rain precipitation, are located near the dusk- or dawn-side of the polar cap boundary, and are associated with the highest-latitude stages of PMAFs/PMARFs (Sandholt et al., 2009).

Whilst the study by Provan et al. (1999) identified flow channel like features (i.e PIFs) in the Finland SuperDARN radar, they did not stipulate that the feature had to be embedded within a discernible background flow. In this study, we identify flow channels which are embedded in a discernible background flow and explore their relationship to IMF By. We apply the flow channel detection algorithm from Herlingshaw et al. (2019) to 2 years of SuperDARN data from the Longyearbyen radar. The statistical characteristics of the detected flow channels are examined including the duration, width, peak velocity and monthly occurrence. The solar wind driving conditions are investigated, as is the dependence of the flow channels on IMF By and the critical clock and regime for flow channel formation.

2 Instrumentation

The Super Dual Auroral Network (SuperDARN) is a chain of high-frequency radars whose field-of-view collectively cover large regions of the polar ionospheres in both hemispheres (Greenwald et al., 1995; Chisham et al., 2007). Each SuperDARN radar is frequency agile (8-20 MHz) and measures the line-of-sight Doppler velocity, spectral width, and backscatter power from decameter-scale ionospheric irregularities at E-region and F-region altitudes. These irregularities can be used as markers to accurately measure the ionospheric convection velocity.

In this study, we use 2 years of data (October 2016 - November 2018) from the Longyearbyen (LYR) SuperDARN radar, located at 78.153 °N, 16.074 °E, 472 m altitude. This radar was selected as its FOV covers a large area of the polar cap, including the dayside cusp region, regularly recording data up to 1500 km in range (with a largest possible range of 3,500 km) and a latitudinal span of approximately 76-82° (magnetic coordinates). This latitudinal range is statistically located

in the polar cap, as it is poleward of the average location of the open-closed field line boundary at 75° (Yeoman et al., 2002). In common mode of operation, the radar beam is steered through 16 positions with an azimuthal separation of 3.24° with a 1 minute resolution. Each radar beam contains 75 range gates with a distance to the first range gate of 180km and a range resolution of 45 km.

Solar wind velocity and IMF By and Bz components (GSM) were obtained from the NASA/GSFC's OMNI data set through OMNIWeb. The data have been time shifted to Earth's bow shock.

3 Method

In this statistical study, we use the algorithm described by Herlingshaw et al. (2019) to automatically detect flow channels in SuperDARN LYR data over a two year period from October 2016 - November 2018. Examples of flow channels detected with the algorithm can be seen in Herlingshaw et al. (2019) (Fig.1 and Fig.3) and in the supporting documentation of the current paper. Here, we summarize some of the key features of the algorithm. The algorithm identifies velocity structures with average magnitudes over 900 m s^{-1}. These velocity structures must be embedded within a slower moving background flow with sharp gradients on the edges of the flow channel. The algorithm searches for sharp gradients of opposing signs on the edges of the flow channel with magnitudes of at least 400 m s^{-1} $cell^{-1}$. The background flows do not include any velocities exceeding 900 m s^{-1} as it should be moving slowly with respect to the flow channel. Principle component analysis and ellipse fitting were used to determine the width and orientation of the flow channel. The algorithm uses a 3 minute average of 1 min resolution common mode data in order to increase the coverage of the received backscatter. The detections are then split into events, which are classified as a continuous detection of a flow channel with no time gaps greater than 3 min. For a more detailed explanation of the algorithm, see Herlingshaw et al. (2019).

A total of 1048 events were identified during this period. We will investigate the characteristics of the flow channels including: location, duration, width, peak velocity and IMF By dependence. All of these properties are outputs of the algorithm, except for the IMF By dependency. We define the IMF clock angle (θ) as

$$\theta = \tan^{-1}\left(\frac{B_y}{B_z}\right), \tag{1}$$

where θ ranges from 0 - 360°. The clock angles were used to separate the IMF into By-dominant and By+ dominant ($45° < \theta < 135°$). Reconnection bursts at the magnetopause take place for a wide range of clock angles (30° to 330°) (Neudegg et al., 2000). We expect to observe reconnection driven dayside signatures within our By+ and By- dominated regimes as they are within this range.

4 Results & Analysis

The first statistical characteristic of the flow channels examined was the flow channel MLAT/MLT location. Fig. 1 shows occurrence distribution of the flow channel centers at the beginning of each event on a polar grid. The distribution is plotted in MLAT/MLT coordinates in 2° by 2° bins. The majority of flow channels were detected on the dayside, with the densest population in the pre-noon sector between 9-12 MLT. There are also events present on the flanks and nightside in smaller abundances. These results indicate that the location of the Longyearbyen radar is favourable for detecting plasma accelerated to high speeds within the dayside cusp region, likely due to dayside reconnection. The small occurrence of nightside flow channels could be due to the FOV of the radar being too far north in order to identify nightside reconnection driven channels.

In this paper we are concerned with FC occurring on the dayside, therefore the detected events were filtered by MLT ($6 \leq \text{MLT} \leq 18$). From this point on, the analysis will focus on the 998 dayside events. Solar wind orientation is a key driver of the dayside reconnection which drives the high latitude convection and thus is intimately linked to dayside flow channels. To explore these driving conditions, the IMF was averaged 10 minutes before each event and the clock angle

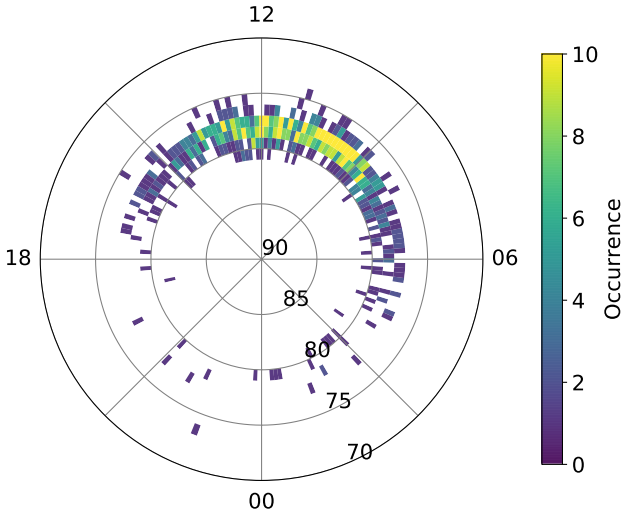

Figure 1. Occurrence distributions in MLAT/MLT coordinates binned into 2° by 2° bins of the flow channel center at the beginning of each event within the study.

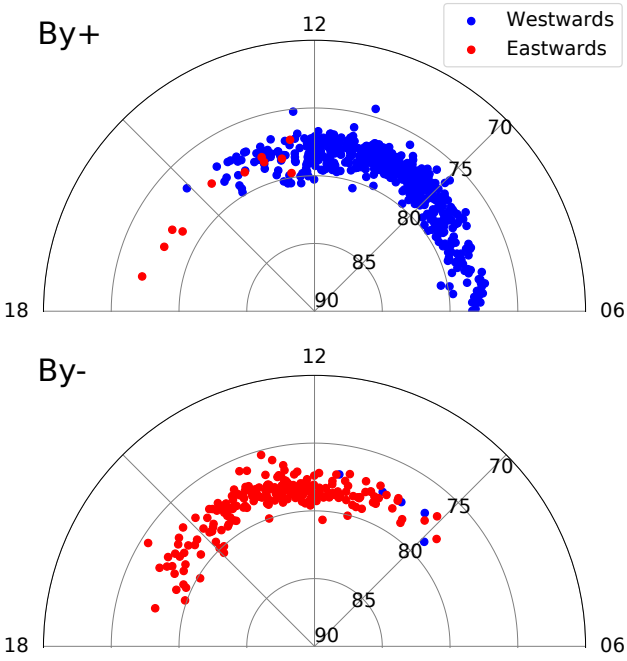

Figure 2. Occurrence distributions in MLAT/MLT coordinates for top) IMF By+ dominated and bottom) IMF By- dominated solar wind conditions. Filled circles represent the direction of the plasma flow within the channel center at the beginning of each event, where blue and red indicate flows westward (towards) and eastward (away) from the Longyearbyen radar respectively.

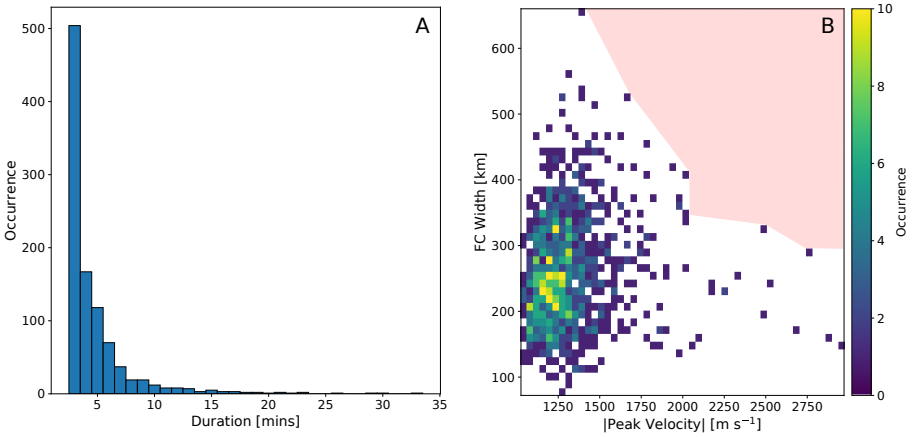

Figure 3. Distributions of a) flow channel duration and b) flow channel width against the magnitude of the peak flow channel velocity.

calculated using Eqn. 1. There was no restraint on the stability of the IMF, so our sample includes both periods of stable and variable IMF.

Fig.2 shows the MLT/MLAT distribution of the flow channel centers at the beginning of each event for IMF By+ (top) and By- (bottom) dominated regimes. Blue filled circles mark plasma flows within the channels moving towards the radar and red mark plasma flows within the channels moving away from the radar. As the Longyearbyen radar FOV is orientated towards the North East, the red points indicate an eastward component of flow while the blue indicate a more westward component. The flow channels show a distinct dependence on IMF By where the flow channel location is shifted dawnward for By+ and duskward for By-. This is the opposite direction to where the mapped footprint of the reconnection region is displaced in each case.

In addition to the location of the flow channels, the duration, FC width and peak velocity of the detected flow channels were also investigated, as shown in the distributions in Fig. 3a and Fig. 3b. As each scan is a three minute average, Fig.3a shows that 49% of the 998 events were detected for the minimum possible duration. There are however a small subset (6%) of stable events that last over 10 minutes. Fig.3b shows that the flow channels range between 72 to 660 km width and peak velocities of 1 - 3 km^{-1}. The densest population of flow channels range between 200-300 km width peak velocities of 1.1-1.3 km s^{-1}. There is also a fast population that travel over 1.5 km/s (12%).

Fig. 4 shows the monthly flow channel occurrence normalised to the monthly operational radar time for the two year interval. The distribution shows a clear bimodal signature, where the distribution peaks in March and October, close to the spring and autumn equinoxes.

Fig. 5 shows the distribution of IMF clock angles at the beginning of each flow channel event. Each radial spoke shows the percentage of flow channel events within a 30 degree range of clock angles. The colored bins within each spoke show the magnitude of the peak velocity within the flow channels at the beginning of each event. The flow channels show a clear IMF By dependency, as the occurrences rise towards By dominant angles and fall towards Bz dominant angles. There are 554 By+ events, 227 By-, 86 Bz+ and 89 Bz- events. There were no corresponding IMF data for 42 of the FCs, so it was not possible to include these events in the analysis of the IMF By dependence. The higher number of By+ events could be a result of reconnection in the By+ configuration drawing in plasma from the postnoon sector, which has been illuminated longer by the solar radiation. The plasma in the postnoon sector has consequently been ionised more and is

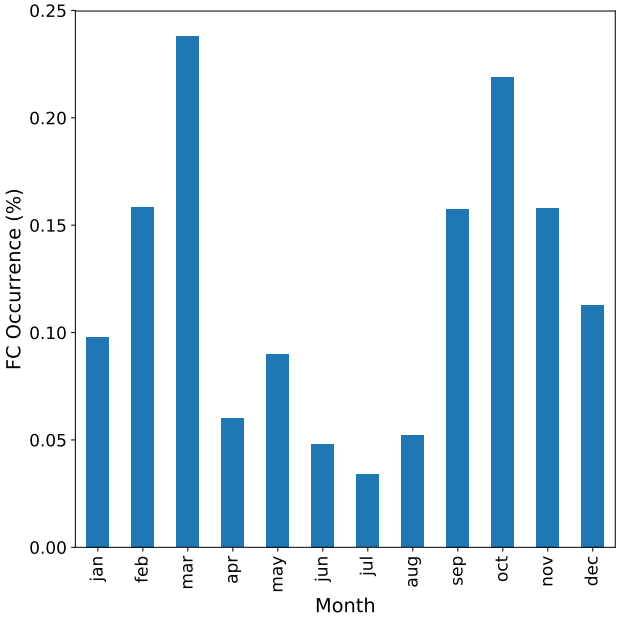

Figure 4. Monthly dayside flow channel occurrence normalised to monthly operational radar time on the dayside ($06 \leq \text{MLT} \leq 18$).

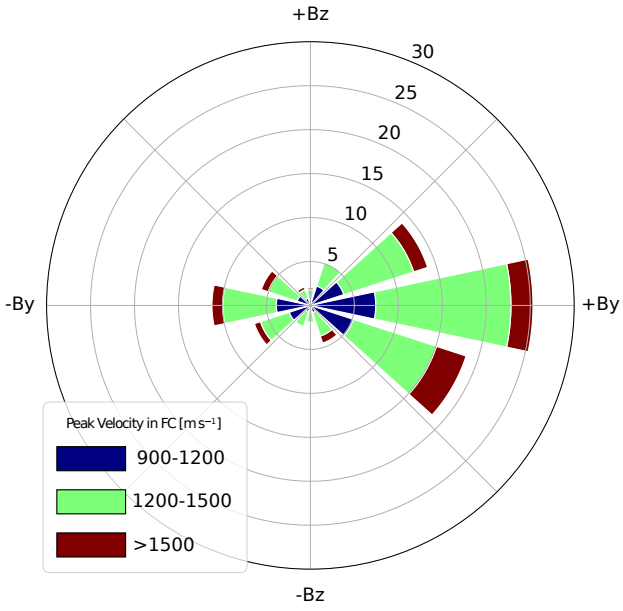

Figure 5. Windrose diagram showing 30°-wide solar wind clock angle radial spokes, colored to peak flow channel velocity magnitudes of 900-1200 m s^{-1} (blue), 1200-1500 m s^{-1} (green) and >1500 m s^{-1} (red). The radial axis shows the percentage of flow channel occurrence, increasing in 5% increments.

denser, so it creates more ionospheric irregularities for the SuperDARN radar to measure and we can therefore easily measure the flow channels in these driving conditions (Koustov et al., 2019).

Other relations were investigated but not displayed in this paper as there were no clear relationships. For example, there was no obvious link between the magnitude of flow velocity on the MLT location or the magnitude of IMF By and the flow velocity.

5 Discussion

The first statistical study on polar cap flow channels within Longyearbyen SuperDARN data was conducted to provide quantitative insight regarding the mesoscale flow structures embedded within the large scale ionospheric convection. Our algorithm has the capability to detect flow channels at all MLT/MLATs measured by the LYR radar. The algorithm identifies flow channels with average speeds over 900 m/s, embedded in background flows moving at least 400 m/s slower with sharp gradients on either side of the channel. Most flow channels were detected on the dayside, peaking between 9 - 12 MLT, with scattered events on the flanks and nightside. To investigate the dayside driven channels, the events were filtered to include only those between 6-18 MLT.

5.1 Duration of Zonal Flow Channels

Dayside flow channels have previously been estimated to range from 5-25 minutes in duration (Lockwood et al., 1990). Almost half (49%) of flow channels were detected for the minimum possible duration of 3 minutes. To create sufficient scatter to detect a FC, the radar requires ionospheric irregularities and the correct ionospheric propagation conditions. The algorithm has a high threshold value of 900 m/s and many other restraints that require high flow values within the FC, low background flow values, and sharp gradients between the two. Therefore, the most common duration of 3 minutes is likely an underestimation of the actual duration of the channels, due to instrumentation effects and the stringent conditions of the algorithm. We likely detect the FC at its peak, but may not record it during the entire formation and decay process, when the channel is turbulent and not well-defined (as seen in the case studies in Herlingshaw et al. (2019)).

Fig. 1 shows that the algorithm detects FC both in the dayside cusp and throat region (FC 1 on newly-opened field lines), all the way around to the dawn and dusk flanks (FC 2 on old-opened field lines). We see temporal variability in both of these types of FC, as they rise above the threshold level and then fall back below it, like a transient pulse. Provan et al. (1999) observed pulsed transients poleward of the convection reversal boundary with a recurrence rate of 7-8 min. The FCs deeper into the polar cap, on old open field lines, have mainly been studied with single DMSP satellite passes (Sandholt & Farrugia, 2009), so it was not possible to detect variation in the FCs. Our method reveals that there is a high degree of temporal variation in the FC on old open flux in the polar cap, which is consistent with a case study of Oksavik et al. (2010).

5.2 Width and Peak Velocity of Zonal Flow Channels

The Longyearbyen radar look direction is most favourable to detect longitudinally orientated flow channels. We therefore primarily measure the latitudinal width of the channel, which spans over a few beams, and cannot detect the longitudinal width of the channel if it extends out of the radar FOV. Fig. 3 shows that the flow channels were mostly between 200 - 300 km in latitudinal width with peak velocities of 1.1-1.3 km/s. The width values are of a similar order to previous studies, such as Pinnock et al. (1993) (100 km), Provan et al. (1998) (250 km), Wang et al. (2016) (300 km) and Zou et al. (2015) (200-300 km).

The interesting result regarding these FC characteristics involves the red-shaded area in Fig. 3. This area is void of data, pointing to an absence of fast, wide FC. This is not true for the most densely populated area of the distribution (1.1-1.3 km/s), where there is a large spread in widths. This suggests that high velocity flows in the polar cap seem to concentrate and be localised into narrower channels. However, the population of flow channels with very high speeds (>1500 m/s) and large widths (>500 km) is small, so the exact relationship requires further study to be confirmed.

5.3 IMF By dependence of Zonal Flow Channels

Fig.2 and Fig. 5 clearly show that the flow channel location and direction have an IMF By dependence. The flow channel location is pushed dawnwards for IMF By+ and mostly westward flows are observed on the dayside, while for IMF By- the flow channel location is pushed duskward and mostly eastwards flows are observed. This IMF By dependence is consistent with statistics of other phenomena linked to flow channels such as PIFs (Provan et al., 1999), PMAFs (Karlson et al., 1996), airglow patches (Wang et al., 2016) and polar cap patches (Spicher et al., 2017). Provan et al. (1999) suggest that for IMF By+, the cusp and dayside merging gap are shifted postnoon and cusp precipitation occurring immediately downstream will be shifted prenoon. Under the influence of the tension applied to the field lines, the FC will flow predominantly westwards into the dawn sector. The opposite will occur for IMF By- and this is consistent with the trends in Fig.2. The main statistical study relating to SuperDARN observations of PIFs by Provan et al. (1999) used the SuperDARN radar located in Finland with a FOV pointing towards North. The Longyearbyen field of view (pointing mostly Eastwards) is orientated much more favourably to detect the zonal flows associated with the tensions of a nonzero IMF By component. The position of the LYR radar at 78° latitude is also more ideal than the Finland radar (located at 62° latitude) for detecting FC on newly opened field lines, as the LYR radar rotates underneath the cusp and dayside reconnection region. Our algorithm also uses the entire field of view to automatically detect 998 events over a 3 year period, while Provan et al. (1999) used a 2-beam swinging technique to manually identify 31 days with PIF activity. Using the entire FOV allows us to confidently detect FC embedded within a slower moving background flow.

The dependency on IMF Bz shows that in the absence of a significant IMF By component, the distribution is more centered around noon in the IMF Bz- dominated case (not shown) as the reconnection region has not been shifted dawnward or duskward. However, the SuperDARN Longyearbyen radar has a look direction primarily East-West. This orientation is not favourable to measure any high velocity anti-sunward (Northward) components of flow present during IMF Bz- dominant conditions, which would flow perpendicular to the radar beams. Only 9% of the flow channels were detected under predominant IMF Bz+ conditions and the distribution in MLAT/MLT (not included) shows no clear relationship, possibly due to complicated flow ionospheric patterns resulting from lobe reconnection.

The majority of detected flow channels (78%) were under By dominant conditions. As stated, the look direction of the SuperDARN Longyearbyen radar could be biasing these results, as it is orientated in a favourable direction to detect zonal flow channels. However, Wang et al. (2016) also find that they detect flow channels associated with airglow patches most frequently during IMF By dominant conditions. In that study, satellite data were used to determine the flow characteristics, removing the look-direction bias that applies to single SuperDARN radars and still noting the same IMF By dependence. The results in this study support the work of Wang et al. (2016), but the application of the algorithm to more radars in the SuperDARN network with different positions and look directions is required to confirm the IMF By dependence.

5.4 Seasonal Variation of Zonal Flow Channels

Fig. 4 shows a bimodal distribution, with peaks close to the spring and autumn equinoxes. This distribution is likely influenced by the peaks in geomagnetic activity around the equinoxes due to the Russell-McPherron effect (Russell & McPherron, 1973). This effect describes the semi-annual variation of geomagnetic activity due to the southward component of the IMF becoming statistically more geoeffective around the equinoxes. A similar distribution is also observed for the PIFs in Provan et al. (1999). Our results contain flow channels on both newly opened and old opened field lines and this monthly distribution indicates a link between reconnection signatures in the majority of cases, regardless of whether the dayside features that can be seen are PIFs or another phenomena.

6 Conclusions

Our algorithm to detect flow channels within the polar cap (Herlingshaw et al., 2019) was applied to two years of data from the SuperDARN LYR radar. The algorithm identified 1048 flow

channels. The majority of the FC were located on the dayside, peaking between 9-12 MLT, but there were also events present around the dawn and dusk flanks and on the nightside. In this study, we focused on channels formed by dayside reconnection, close to the cusp/throat region and deeper into the polar cap. The events were then filtered to $06 \leq \text{MLT} \leq 18$, which left 998 events remaining. The main findings of the study can be summarized as follows:

- The majority of the flow channels were short, variable pulses of 3 minutes in duration.
- The FC were typically between 200-300 km in latitudinal width with peak velocities of 1.1 - 1.3 km/s.
- At lower peak velocities (<1.5 km/s), the spread in width is broad (72 - 660 km. Above this threshold, there are fewer fast, wide channels which suggests that higher velocity flows in the polar cap concentrate into localised, narrower channels.
- The flow channel location shows an IMF By dependence. The FC location is pushed dawnwards for +By with mostly westward flows and duskwards for -By with mostly eastward flows.
- The monthly FC occurrence shows a bimodal distribution with peaks around the equinoxes, likely due to increased solar wind-magnetospheric coupling at these times as described by the Russell-McPherron effect.

The coverage of the SuperDARN Longyearbyen radar was ideally situated for studying dayside zonal flows between 76-82° latitude (magnetic coordinates). In our future work, we will extend the algorithm to all SuperDARN radars within the polar cap in both hemispheres. This will allow us to understand the temporal evolution of flow channels across the entire polar cap region, the driving factors involved from the solar wind, and any inter-hemispheric asymmetries.

Acknowledgments

Financial support was provided by the Research Council of Norway under contract 223252. Solar wind and IMF data are available at the Goddard Space Flight Center Space Physics Data Facility (`https://cdaweb.sci.gsfc.nasa.gov/index.html/`). The authors acknowledge the use of SuperDARN data, which are available online (`http://vt.superdarn.org/`). SuperDARN is a collection of radars funded by the national scientific funding agencies of Australia, Canada, China, France, Italy, Japan, Norway, South Africa, United Kingdom and United States of America. The flow channel database generated for this paper is available online (`https://figshare.com/articles/Flow_Channels_Detected_in_SuperDARN_Longyearbyen_data_2016-2018 /12482642`).

References

Andalsvik, Y., Sandholt, P., & Farrugia, C. (2011, 11). Dayside and nightside contributions to cross-polar cap potential variations: The 20 March 2001 ICME case. *Annales Geophysicae*, *29*, 2189-2201. doi: 10.5194/angeo-29-2189-2011

Carlson, H., Moen, J., Oksavik, K., Nielsen, C., Mccrea, I., Pedersen, T., & Gallop, P. (2006, 03). Direct observations of injection events of subauroral plasma into the polar cap. *Geophysical Research Letters*, *33*. doi: 10.1029/2005GL025230

Carlson, H. C. (2012). Sharpening our thinking about polar cap ionospheric patch morphology, research, and mitigation techniques. *Radio Science*, *47*(4). doi: 10.1029/2011RS004946

Chisham, G., Lester, M., Milan, S. E., Freeman, M. P., Bristow, W. A., Grocott, A., ... Walker, A. D. (2007). A decade of the Super Dual Auroral Radar Network (SuperDARN): Scientific achievements, new techniques and future directions. *Surveys in Geophysics*, *28*(1), 33–109. doi: 10.1007/s10712-007-9017-8

Cousins, E. D. P., & Shepherd, S. G. (2010). A dynamical model of high-latitude convection derived from SuperDARN plasma drift measurements. *Journal of Geophysical Research: Space Physics*, *115*(A12). doi: 10.1029/2010JA016017

Cowley, S., & Lockwood, M. (1992). Excitation and decay of solar-wind driven flows in the magnetosphere-ionosphere system. *Annales Geophysicae*, *10*, 103–115.

Davies, J. A., Yeoman, T. K., Rae, I. J., Milan, S. E., Lester, M., Lockwood, M., & McWilliams, A. (2002). Ground-based observations of the auroral zone and polar cap ionospheric re-

sponses to dayside transient reconnection. *Annales Geophysicae*, *20*(6), 781–794. doi: 10.5194/angeo-20-781-2002

Dungey, J. W. (1961, Jan). Interplanetary magnetic field and the auroral zones. *Phys. Rev. Lett.*, *6*, 47–48. doi: 10.1103/PhysRevLett.6.47

Greenwald, R. A., Baker, K. B., Dudeney, J. R., Pinnock, M., Jones, T. B., Thomas, E. C., ... Yamagishi, H. (1995, 2). DARN/SuperDARN. *Space Science Reviews*, *71*(1-4), 761–796. doi: 10.1007/BF00751350

Haerendel, G., Paschmann, G., Sckopke, N., Rosenbauer, H., & Hedgecock, P. C. (1978). The frontside boundary layer of the magnetosphere and the problem of reconnection. *Journal of Geophysical Research: Space Physics*, *83*(A7), 3195-3216. doi: 10.1029/JA083iA07p03195

Heelis, R. A. (1984). The effects of interplanetary magnetic field orientation on dayside high-latitude ionospheric convection. *Journal of Geophysical Research: Space Physics*, *89*(A5), 2873-2880. doi: 10.1029/JA089iA05p02873

Heppner, J. P., & Maynard, N. C. (1987). Empirical high-latitude electric field models. *Journal of Geophysical Research: Space Physics*, *92*(A5), 4467-4489. doi: 10.1029/JA092iA05p04467

Herlingshaw, K., Baddeley, L., Oksavik, K., Lorentzen, D., & Bland, E. (2019, 10). A study of automatically detected flow channels in the polar cap ionosphere. *Journal of Geophysical Research: Space Physics*, *124*. doi: 10.1029/2019JA026916

Hosokawa, K., Zou, Y., & Nishimura, Y. (2019, 11). Airglow patches in the polar cap region: A review. *Space Science Reviews*, *215*. doi: 10.1007/s11214-019-0616-8

Karlson, K. A., Øieroset, M., Moen, J., & Sandholt, P. E. (1996). A statistical study of flux transfer event signatures in the dayside aurora: The IMF By-related prenoon-postnoon symmetry. *Journal of Geophysical Research: Space Physics*, *101*(A1), 59-68. doi: 10.1029/95JA02590

Koustov, A. V., Ullrich, S., Ponomarenko, P. V., Nishitani, N., Marcucci, F. M., & Bristow, W. A. (2019). Occurrence of F region echoes for the polar cap SuperDARN radars. *Earth, Planets and Space*, *71*(1), 112.

Lockwood, M., Cowley, S. W. H., Sandholt, P. E., & Lepping, R. P. (1990). The ionospheric signatures of flux transfer events and solar wind dynamic pressure changes. *Journal of Geophysical Research: Space Physics*, *95*(A10), 17113-17135. doi: 10.1029/JA095iA10p17113

Lockwood, M., Milan, S. E., Onsager, T., Perry, C. H., Scudder, J. A., Russell, C. T., & Brittnacher, M. (2001). Cusp ion steps, field-aligned currents and poleward moving auroral forms. *Journal of Geophysical Research: Space Physics*, *106*(A12), 29555-29569. doi: 10.1029/2000JA900175

MacDougall, J. W., & Jayachandran, P. T. (2001). Polar cap convection relationships with solar wind. *Radio Science*, *36*(6), 1869-1880. doi: 10.1029/2001RS001007

Moen, J., Oksavik, K., Alfonsi, L., Rinne, Y., Romano, V., & Spogli, L. (2013, 01). Space weather challenges of the polar cap ionosphere. *Journal of Space Weather and Space Climate*, *3*, 02-. doi: 10.1051/swsc/2013025

Neudegg, D., Cowley, S., Milan, S., Yeoman, T., Lester, M., Provan, G., ... Georgescu, E. (2000, 04). A survey of magnetopause FTEs and associated flow bursts in the polar ionosphere. *Annales Geophysicae*, *18*, 416-435. doi: 10.1007/s005850050900

Nishimura, Y., Lyons, L. R., Zou, S., Xing, X., Angelopoulos, V., Mende, S. B., ... Heinselman, C. (2010). Preonset time sequence of auroral substorms: Coordinated observations by all-sky imagers, satellites, and radars. *Journal of Geophysical Research: Space Physics*, *115*(A5). doi: 10.1029/2010JA015832

Nishimura, Y., Lyons, L. R., Zou, Y., Oksavik, K., Moen, J. I., Clausen, L. B., ... Lester, M. (2014). Day-night coupling by a localized flow channel visualized by polar cap patch propagation. *Geophysical Research Letters*, *41*(11), 3701-3709. doi: 10.1002/2014GL060301

Oksavik, K., Barth, V. L., Moen, J., & Lester, M. (2010). On the entry and transit of high-density plasma across the polar cap. *Journal of Geophysical Research: Space Physics*, *115*(A12). doi: 10.1029/2010JA015817

Oksavik, K., Moen, J., & Carlson, H. C. (2004). High-resolution observations of the small-scale flow pattern associated with a poleward moving auroral form in the cusp. *Geophysical Research Letters*, *31*(11). doi: 10.1029/2004GL019838

Pettigrew, E. D., Shepherd, S. G., & Ruohoniemi, J. M. (2010). Climatological patterns of

high-latitude convection in the Northern and Southern hemispheres: Dipole tilt dependencies and interhemispheric comparisons. *Journal of Geophysical Research: Space Physics*, *115*(A7). doi: 10.1029/2009JA014956

Pinnock, M., Rodger, A. S., Dudeney, J. R., Baker, K. B., Newell, P. T., Greenwald, R. A., & Greenspan, M. E. (1993). Observations of an enhanced convection channel in the cusp ionosphere. *Journal of Geophysical Research: Space Physics*, *98*(A3), 3767-3776. doi: 10.1029/92JA01382

Provan, G., Yeoman, T., & Milan, S. (1998, 11). CUTLASS Finland radar observations of the ionospheric signatures of flux transfer events and the resulting plasma flows. *Annales Geophysicae*, *16*. doi: 10.1007/s00585-998-1411-0

Provan, G., Yeoman, T. K., & Cowley, S. W. H. (1999). The influence of the IMF By component on the location of pulsed flows in the dayside ionosphere observed by an HF radar. *Geophysical Research Letters*, *26*(4), 521-524. doi: 10.1029/1999GL900009

Rinne, Y., Moen, J., Baker, J. B. H., & Carlson, H. C. (2011). Convection surrounding mesoscale ionospheric flow channels. *Journal of Geophysical Research: Space Physics*, *116*(A5). doi: 10.1029/2010JA015997

Rinne, Y., Moen, J., Carlson, H. C., & Hairston, M. R. (2010). Stratification of east-west plasma flow channels observed in the ionospheric cusp in response to IMF BY polarity changes. *Geophysical Research Letters*, *37*(13). doi: 10.1029/2010GL043307

Ruohoniemi, J. M., & Greenwald, R. A. (1996). Statistical patterns of high-latitude convection obtained from Goose Bay HF radar observations. *Journal of Geophysical Research: Space Physics*, *101*(A10), 21743-21763. doi: 10.1029/96JA01584

Ruohoniemi, J. M., & Greenwald, R. A. (2005). Dependencies of high-latitude plasma convection: Consideration of interplanetary magnetic field, seasonal, and universal time factors in statistical patterns. *Journal of Geophysical Research: Space Physics*, *110*(A9). doi: 10.1029/2004JA010815

Russell, C. T., & Elphic, R. C. (1978). Initial ISEE Magnetometer Results: Magnetopause Observations (Article published in the special issues: Advances in Magnetospheric Physics with GEOS- 1 and ISEE - 1 and 2.). *Space Sci. Rev.*, *22*(6), 681-715. doi: 10.1007/BF00212619

Russell, C. T., & Elphic, R. C. (1979). ISEE observations of flux transfer events at the dayside magnetopause. *Geophysical Research Letters*, *6*(1), 33-36. doi: 10.1029/GL006i001p00033

Russell, C. T., & McPherron, R. L. (1973). Semiannual variation of geomagnetic activity. *Journal of Geophysical Research (1896-1977)*, *78*(1), 92-108. doi: 10.1029/JA078i001p00092

Sandholt, P., Andalsvik, Y., & Farrugia, C. (2010, 11). Polar cap flow channel events: Spontaneous and driven responses. *Annales Geophysicae*, *28*. doi: 10.5194/angeo-28-2015-2010

Sandholt, P., & Farrugia, C. (2009, 04). Plasma flow channels at the dawn/dusk polar cap boundaries: Momentum transfer on old open field lines and the roles of IMF By and conductivity gradients. *Annales Geophysicae*, *27*. doi: 10.5194/angeo-27-1527-2009

Sandholt, P., Farrugia, C., & Aandalsvik, Y. (2009, 12). Polar cap convection/precipitation states during earth passage of two ICMEs at minimum of solar cycle 23. *AGU Fall Meeting Abstracts*.

Spicher, A., Clausen, L. B. N., Miloch, W. J., Lofstad, V., Jin, Y., & Moen, J. I. (2017). Interhemispheric study of polar cap patch occurrence based on Swarm in situ data. *Journal of Geophysical Research: Space Physics*, *122*(3), 3837-3851. doi: 10.1002/2016JA023750

Thomas, E. G., & Shepherd, S. G. (2018). Statistical patterns of ionospheric convection derived from mid-latitude, high-latitude, and polar SuperDARN HF radar observations. *Journal of Geophysical Research: Space Physics*, *123*(4), 3196-3216. doi: 10.1002/2018JA025280

Wang, B., Nishimura, Y., Lyons, L., Zou, Y., Carlson, H., Frey, H., & Mende, S. (2016, 09). Analysis of close conjunctions between dayside polar cap airglow patches and flow channels by all-sky imager and DMSP. *Earth, Planets and Space*, *68*, 150. doi: 10.1186/s40623-016-0524-z

Yeoman, T., Hanlon, P., & McWilliams, K. (2002, 02). Letter to the editor: A statistical study of the location and motion of the HF radar cusp. *Annales Geophysicae*, *20*, 275-280.

Zou, Y., Nishimura, Y., Lyons, L. R., Shiokawa, K., Donovan, E. F., Ruohoniemi, J. M., ... Nishitani, N. (2015). Localized polar cap flow enhancement tracing using airglow patches: Statistical properties, imf dependence, and contribution to polar cap convection. *Journal of Geophysical Research: Space Physics*, *120*(5), 4064–4078.

Graphic design: Communication Division, UiB / Print: Skipnes Kommunikasjon AS

uib.no

ISBN: 9788230854402 (print)
9788230840900 (PDF)